



UNIVERSITAT DE
BARCELONA

Classifying synthesized optical codes using polarimetric information and machine learning algorithms for optical security applications

Kavan Ahmadi

ADVERTIMENT. La consulta d'aquesta tesi queda condicionada a l'acceptació de les següents condicions d'ús: La difusió d'aquesta tesi per mitjà del servei TDX (www.tdx.cat) i a través del Dipòsit Digital de la UB (diposit.ub.edu) ha estat autoritzada pels titulars dels drets de propietat intel·lectual únicament per a usos privats emmarcats en activitats d'investigació i docència. No s'autoritza la seva reproducció amb finalitats de lucre ni la seva difusió i posada a disposició des d'un lloc aliè al servei TDX ni al Dipòsit Digital de la UB. No s'autoritza la presentació del seu contingut en una finestra o marc aliè a TDX o al Dipòsit Digital de la UB (framing). Aquesta reserva de drets afecta tant al resum de presentació de la tesi com als seus continguts. En la utilització o cita de parts de la tesi és obligat indicar el nom de la persona autora.

ADVERTENCIA. La consulta de esta tesis queda condicionada a la aceptación de las siguientes condiciones de uso: La difusión de esta tesis por medio del servicio TDR (www.tdx.cat) y a través del Repositorio Digital de la UB (diposit.ub.edu) ha sido autorizada por los titulares de los derechos de propiedad intelectual únicamente para usos privados enmarcados en actividades de investigación y docencia. No se autoriza su reproducción con finalidades de lucro ni su difusión y puesta a disposición desde un sitio ajeno al servicio TDR o al Repositorio Digital de la UB. No se autoriza la presentación de su contenido en una ventana o marco ajeno a TDR o al Repositorio Digital de la UB (framing). Esta reserva de derechos afecta tanto al resumen de presentación de la tesis como a sus contenidos. En la utilización o cita de partes de la tesis es obligado indicar el nombre de la persona autora.

WARNING. On having consulted this thesis you're accepting the following use conditions: Spreading this thesis by the TDX (www.tdx.cat) service and by the UB Digital Repository (diposit.ub.edu) has been authorized by the titular of the intellectual property rights only for private uses placed in investigation and teaching activities. Reproduction with lucrative aims is not authorized nor its spreading and availability from a site foreign to the TDX service or to the UB Digital Repository. Introducing its content in a window or frame foreign to the TDX service or to the UB Digital Repository is not authorized (framing). Those rights affect to the presentation summary of the thesis as well as to its contents. In the using or citation of parts of the thesis it's obliged to indicate the name of the author.

Tesi doctoral

**Classifying synthesized optical codes using
polarimetric information and machine
learning algorithms for optical security
applications**

Kavan Ahmadi



UNIVERSITAT DE
BARCELONA

**Classifying synthesized optical codes using
polarimetric information and machine
learning algorithms for optical security
applications**

Programa de doctorat en Física

Autor: Kavan Ahmadi

Director: Prof. Artur Carnicer González

Tutora: Prof. Assumpta Parreño García

Departament de Física Aplicada

Universitat de Barcelona



UNIVERSITAT DE
BARCELONA

*“ patience with small details makes
perfect a large work, like the universe ”*

Rumi, a Persian poet

*Dedicated to my parents, Mahnaz and
Fathollah, and my Nanaz, who has always
been like a mother to me*

Acknowledgment

First and foremost, I am extremely grateful to my supervisor, Prof. Artur Carnicer, for his invaluable advice, continuous support, and patience during my PhD study. His immense knowledge and plentiful experience have encouraged me all the time in my academic research. I would also like to thank Prof. Pedro Latorre-Carmona, Prof. Ignacio Juvells Prades, and Prof. David Maluenda for their technical support on my study.

I acknowledge the financial support from the University of Barcelona under the predoctoral program (APIF). This work has also been partially funded by Ministerio de Ciencia y Tecnología, project PID2019-104268GB-C22.

Finally, I would like to express my gratitude to my family. Without their tremendous support and encouragement throughout my studies, it would be impossible for me to complete this journey.

Abstract

Given the increasing use of the internet and the transfer of information in this era, it is crucial to focus on encryption and data security. According to the technological advances in optics and photonics and their multiple applications, many researchers have been urging to apply optics to encrypt and authenticate information in the last decades. In other words, optical waveforms involve many complex degrees of freedom, such as polarization, amplitude, phase, large bandwidth, quantum properties of photons, and multiplexing that can be combined in many ways to produce high-security information systems.

In this thesis, we have been investigating different photonics techniques appropriate for optical security applications. This interdisciplinary investigation includes photonics techniques such as digital holography, beam shaping, Fourier optics, polarization optics, diffractive imaging system, and interferometry. Besides, our applied approaches demanded extensive research in computational methods such as pattern classification by means of machine learning algorithms, computer simulation, fringe analysis, statistical analysis, and binary encoding. However, despite the defined thesis title, our achievement has not been limited to optical security.

Classifying synthesized (unique) optical codes can be mainly split into two categories. The first one is an approach for obtaining unique optical codes. The second one is a method or technique for classifying and distinguishing synthesized optical codes.

Regarding the first category, in this thesis, on the one hand, we propose a method to obtain unique optical codes (polarimetric signature codes) from illuminating 3D printed samples by linearly polarized beams. Also, the ability of 3D printed samples to be considered as Physical Unclonable Functions based on polarimetric information is discovered in this thesis. Hence, we consider 3D printed samples as physical keys able to produce unique polarized optical codes. On the other hand, we obtain unique polarized optical codes by synthesizing a laser beam at the entrance pupil of a highly focusing system. Accordingly, we developed a binary approach for encoding character codes into holographic cells appropriate for transferring information in free space.

Regarding the second category, on one side, we classify the polarimetric signature codes obtained by a physical key (3D printed sample) by means of the Support Vector Machine classifier using feature vectors extracted from

statistical analysis on speckle patterns. On the other side, we introduce polarimetric mapping images as multidimensional arrays to be inputs of a convolutional neural network model for the autodetection of character codes obscured in the longitudinal component of a highly focused electromagnetic field. This approach might be considered an alternative method, which eliminates the necessity of phase retrieval algorithms in particular cases.

Besides, one of our motivations in this thesis is related to highly focused electromagnetic fields. Tightly focused beams attract much attention because of the non-neglectable component of the electric field in the direction of propagation. The potential applications of highly focused beams in many fields, such as microscopy, nonlinear optics, tomography, and optical encryption, have been reported. However, the detection of the longitudinal component of a highly focused electromagnetic field is not simple and still is a challenging task. In this thesis, we propose a method based on an experimental and numerical framework to estimate and visualize the longitudinal component of the field using a conventional imaging system. However, achieving this goal required a vast investigation in wavefront engineering and designing a proper optical system able to generate and detect highly focused beams.

To generate an optical beam with an arbitrary intensity and phase distribution, we used a fast method to characterize a twisted-nematic liquid crystal display based on the Mach-Zehnder interferometer and fringe analysis in the Fourier domain. Then we applied the double-pixel hologram Arrizón's approach, which is able to generate on-axis computer-generated hologram into a low-resolution twisted-nematic liquid crystal. Since this codification algorithm is time-consuming, we developed a fast algorithm for mapping double-pixel holograms using the K-Nearest Neighbors machine learning algorithm, which has the potential to generate double-pixel holograms in real-time.

Finally, in this thesis, we present a method to estimate the aberrated wavefront at the focal plane of a vectorial diffraction system. In contrast to the phase, the polarization state of optical fields is simply measurable. In this regard, we introduce an alternative approach for determining the aberration of the wavefront using polarimetric information and convolutional neural networks designed for estimating the Zernike polynomials coefficients.

Resumen

En la actualidad, dado el creciente uso de Internet y la transferencia de información, es fundamental centrarse en el cifrado y la seguridad de los datos. De acuerdo con los avances tecnológicos en óptica y fotónica y sus múltiples aplicaciones, recientemente muchos investigadores han sugerido aplicar técnicas ópticas para encriptar y autenticar información. Esto es posible, ya que las ondas de luz se caracterizan por presentar muchos grados de libertad (polarización, amplitud, fase), gran ancho de banda, propiedades cuánticas de los fotones, y multiplexación, que se pueden combinar de muchas maneras para producir sistemas de información de alta seguridad.

En esta tesis, hemos investigado diferentes técnicas fotónicas apropiadas para aplicaciones de seguridad óptica. Esta investigación interdisciplinaria incluye técnicas como holografía digital, codificación de información en haces, óptica difractiva y de Fourier, polarización, e interferometría, entre otras. Además, nuestro enfoque aplicado exigieron una amplia investigación en métodos computacionales como la clasificación de patrones mediante algoritmos de aprendizaje automático, simulación por ordenador, análisis de franjas, análisis estadístico y codificación binaria. Sin embargo, a pesar del título de la tesis, nuestros logros no se ha limitado a la seguridad óptica.

La clasificación óptica de códigos sintéticos únicos, se puede dividir en dos ámbitos. El primero consiste en la obtención de códigos ópticos únicos. El segundo es un método para clasificar y distinguir códigos ópticos sintetizados. Respecto al primero, por un lado, proponemos un método para obtener códigos ópticos únicos (códigos de firma polarimétrica) a partir de la iluminación de muestras impresas mediante una impresora 3D utilizando luz polarizada linealmente. Además, analizamos la capacidad de las muestras generadas para ser consideradas funciones física no clonables basada en información polarimétrica. Por otro lado, hemos desarrollado un método para codificar información en la pupila de entrada de un sistema altamente enfocado. Dicho de otra manera, se ha desarrollado un enfoque binario para codificar códigos de caracteres en celdas holográficas apropiadas para transferir información en el espacio libre.

En cuanto a la segunda tarea, por un lado, clasificamos los códigos de firma polarimétrica obtenidos mediante una clave física (la muestra impresa en 3D) mediante máquinas de soporte virtual, utilizando vectores de características

extraídos del análisis estadístico de los patrones de speckle. Por otro lado, introdujimos imágenes de mapeo polarimétrico como matrices multidimensionales para que actúen como entradas de un modelo de red neuronal convolucional para la autodetección de códigos de caracteres codificados en la componente longitudinal de un campo electromagnético altamente enfocado. Este enfoque podría considerarse como un método alternativo, que elimina la necesidad del algoritmo de recuperación de fase en casos particulares.

Además, una de nuestras motivaciones en esta tesis, está relacionada con los campos electromagnéticos altamente focalizados. Los haces altamente enfocados atraen mucha atención debido a que la componente del campo eléctrico en la dirección de propagación puede ser no despreciable. Recientemente, han sido reportadas aplicaciones potenciales de estos haces en muchos campos: microscopía, óptica no lineal, tomografía y encriptación óptica. Sin embargo, la detección de la componente longitudinal de un campo electromagnético altamente enfocado no es simple y sigue siendo una tarea desafiante. En esta tesis, proponemos un método basado en un marco experimental y numérico para estimar y visualizar la componente longitudinal del campo utilizando un sistema de imágenes convencional. Lograr este objetivo requirió una vasta investigación en ingeniería de frente de onda y el diseño de un sistema óptico adecuado capaz de generar y detectar haces altamente enfocados.

Para generar haces ópticos con intensidad arbitraria y distribución de fase, utilizamos un método rápido para caracterizar una pantalla de cristal líquido nemática basado en el interferómetro de Mach-Zehnder y el análisis de franjas en el dominio de Fourier. Luego aplicamos la técnica del holograma de doble píxel de Arrizón, que es capaz de generar hologramas en eje. Dado que este algoritmo de codificación requiere mucho tiempo, desarrollamos una técnica rápida para mapear hologramas de doble píxel utilizando el algoritmo de aprendizaje automático de los k vecinos más próximos, que permite generar hologramas de doble píxel en tiempo real.

Finalmente, se ha presentado un método para estimar la aberración del frente de onda en el plano focal de un sistema de difracción vectorial. A diferencia de la fase, el estado de polarización se puede medir con facilidad. En este sentido, presentamos un enfoque alternativo para determinar la aberración del frente de onda utilizando información polarimétrica y redes neuronales convolucionales diseñadas para estimar los coeficientes de polinomios de Zernike.

Contents

Acronyms	xiv
1. Overview	1
1.1. Publications	4
1.1.1. Chapter books	4
1.1.2. Journal papers	4
1.1.3. Conference papers	4
1.2. Other contributions	4
2. Introduction	6
3. Review of basic concepts	13
3.1. Polarization optics	13
3.2. Beams in the focal domain: Application to the optical encryption	22
3.2.1. Fast calculation of the electromagnetic field in the focal domain	22
3.2.2. Optical encryption in the axial domain	24
3.3. Computer-generated hologram: Double-pixel Arrizón's approach	31
3.4. Phase retrieval algorithm	38
3.5. Machine learning	41
3.5.1. K-Nearest Neighbors	43
3.5.2. Support Vector Machine	45
3.5.3. Convolutional Neural Network	48
4. Beam modulation with a twisted nematic liquid crystal display	52
4.1. Twisted nematic liquid crystal display	52
4.2. Characterizing TNLC displays	53
4.2.1. Phase modulation	57
4.2.2. Amplitude modulation	59
4.3. Fast generating DPHs using KNN classifier	61
5. Encoding character codes in an optical beam	66
5.1. Configuration of CEs	66
5.2. Experiment and results	68

6. Generating highly focused EM fields and recovering their transverse and longitudinal components in the focal area	71
6.1. Optical setup	72
6.2. Recovering the transverse components.....	77
6.3. Recovering the longitudinal component	82
7. Estimation of Zernike polynomials for a highly focused EM field using polarimetric mapping images and neural networks	85
7.1. Zernike polynomials	86
7.2. Simulation	87
7.2.1 Training dataset.....	87
7.2.2 Neural network model.....	88
7.3. Discussion and conclusions	91
8. Secret sharing of optically obscured character codes in a highly focused EM field	93
8.1. Encrypting and encoding character codes into an optical beam	93
8.2. Obscuring CEs into the longitudinal component	96
8.3. Polarimetric mapping images and CNN model	97
8.4. Optical implementation and results.....	100
8.5. Analyzing the operation of the system.....	104
8.5.1 Design of CEs	104
8.5.2. PMIs	106
8.6. Robustness of the system against noise and occlusion attack.....	108
8.6.1 Noise	108
8.6.2. Occlusion attack.....	109
9. Polarimetric identification of 3D-printed nanoparticle encoded optical codes	111
9.1. Design of 3D printed samples	112
9.2. Experimental procedure: Polarimetric signature codes	114
9.3. Statistical analysis: Feature extraction	116
9.4. Pattern classification	119

9.4.1. Classifying one group of identical 3D printed samples against the other different samples.....	120
9.4.2. Classifying one sample against the other identical 3D printed samples.....	123
10. Conclusion remarks.....	125
References	128

Acronyms

DES	Data Encryption Standard
AES	Advanced Encryption Standard
TLS	Transport Layer Security
SSH	Secure Shell
DRPE	Double Random Phase Encoding
LCD	Liquid Crystal Display
EM	Electromagnetic
TEM	Transverse Electromagnetic Wave
QR	Quick Response
3D	Three-dimensional
SVM	Support Vector Machine
KNN	K-Nearest Neighbors
TNLC	Twisted-Nematic Liquid Crystal
CCD	Charge-Coupled Device
SLM	Spatial Light Modulator
LP	Linear Polarizer
QWP	Quarter-Wave Plate
HWP	Half-Wave Plate
CGH	Computer-Generated Hologram
DPH	Double-Pixel Hologram
SNR	Signal-to-Noise Ratio
FT	Fourier Transform
FT ⁻¹	Inverse Fourier Transform
CNN	Convolutional Neural Network

ANN	Artificial Neural Network
ASCII	American Standard Code for Information Interchange
UTF-32	32-bit Unicode Transformation Format
CE	Circular Encoder
NA	Numerical Aperture
EP	Entrance Pupil
MO	Microscope Objective
PMI	Polarimetric Mapping Image
DNN	Deep Neural Network
PUF	Physical Unclonable Function

1. Overview

We have begun this PhD thesis with the title “Enhanced photonics techniques for device authentication and encryption” by focusing on two objectives as follows:

1. Encryption methods in the axial domain
2. Security and authentication using 3D optical codes

Regarding objective 1, we used the visual encryption technique to encrypt character codes into two cipher-shares, in which each one obscured into the longitudinal component of a highly focused electromagnetic field. We applied the double-pixel hologram codification algorithm to design light beams. This approach is able to generate an on-axis computer-generated hologram into a low-resolution spatial light modulator. However, this approach demands an extensive search of the minimum Euclidean distance between desired complex values and the accessible ones according to the experimental modulation curve. We proposed an algorithm to map double-pixel holograms using the K-Nearest Neighbor classifier, which is 80 times faster than the conventional calculation. This method was orally presented at the 2021 OSA Imaging and Applied Optics Congress and published as “Fast Mapping of Double-Pixel Holograms using K-Nearest Neighbors.”

Based on this work, I was invited to contribute to writing the chapter titled “Beam implementation with a Translucent Twisted-Nematic Liquid Crystal Display” in the book titled “Holography- Recent Advances and Applications,” edited by Prof. Joseph Rosen.

Besides, we developed a binary approach to encode character codes into holographic cells in order to synthesize optical beams appropriate for obscuring data into highly focused beams. This work was orally presented at the conference IONS Ireland 2021 titled “Encoding ASCII codes in an optical beam.”

Finally, the propagation of the synthesized beams through a highly focusing system has been numerically simulated to provide the training dataset. Accordingly, we applied a convolutional neural network model to recover cipher shares at the focal plane. This project has been published in the Optics and Laser in Engineering journal with the title “Optical visual encryption using focused beams and convolutional neural network.” This proposed scheme can

be improved to reach a higher level of security by combining it with a photon-counting model. We propose this be accomplished in future work.

Also, in cooperation with other members of the Wavefront Engineering group, we developed an experimental and numerical approach using conventional optical and electro-optical devices in order to estimate and visualize the longitudinal component of a highly focused electromagnetic field. This approach also can be applied to encrypt data in the axial domain. This team-working project has been published in the Scientific Reports journal titled “Experimental estimation of the longitudinal component of a highly focused electromagnetic field” with three equally contributed authors. This work involved several tasks for each participant, in which the implementation and design of the experiment was my task.

Our published work proposed a relatively simple way to retrieve the longitudinal component of a tightly focused beam based on a phase retrieval framework that requires capturing polarimetric images at different planes in the focal area. Nevertheless, we did not consider the possible effects of aberrations introduced by the optical system on the results. In this regard, we have commenced developing an algorithm for instant detection of the longitudinal component considering the aberrated wavefronts using polarimetric information and neural networks. In the first step, we developed a numerical algorithm to estimate the Zernike polynomials coefficients using polarimetric mapping images and neural networks. This work has been orally presented at the V International Conference on Applications of Optics and Photonics- AOP2022, and it has been accepted to be published in the Journal of Physics: Conference Series. We hope to extend this work in the future for real-time reconstruction of the longitudinal component of highly focused beams.

Regarding objective 2, to the best of our knowledge, we introduced 3D printer samples as 3D physical keys for the first time. Producing physical keys with unique microstructures and mechanical properties usually demands advanced technologies, which can be economically expensive. In contrast, we used a low-cost 3D printer with conventional polylactic acid filament filled with metallic powder to produce 3D samples appropriate for polarimetric signature implementation. We investigated an interesting real-world scenario that shows how a single class of codes can be distinguished (authenticated) among a group of samples to be rejected. This classification was a difficult unbalanced problem since the number of polarimetric signatures that characterize the true class was small compared to the complete dataset. Each sample was characterized by analyzing the polarization state of the emerging light. We found high accuracy in recognizing the true class codes using the one-class support vector machine

classifier. This work has been published in the IEEE Photonics Journal with the title “Polarimetric identification of 3D-printed nanoparticle encoded optical codes.”

The investigation of objective 1 encountered many interesting ideas that provided us to develop the application of our approach in the other research area (as mentioned above). One of the interesting topics that attracted my attention in this PhD thesis is the combination use of optical techniques and machine learning algorithms to find a solution for optics and photonics problems. This can be tracked based on the accomplished works in this thesis. We have mainly been dealing with pattern classifications, which mostly required techniques to obtain unique optical codes using polarimetric information. In this regard, we altered the title of this thesis, which specifically fulfills the purpose of this thesis.

This thesis is organized as follows:

The second section introduces a summary of the most relevant works to this thesis, accompanied by a short history of cryptography. Section 3 reviews the theory, basic techniques, and/ or algorithms applied in this thesis. The achievements in this thesis begin in section 4. An efficient approach to generating light beams with arbitrary intensity and phase distribution using twisted-nematic liquid crystals is described in section 4. Section 5 introduces a binary approach for encoding character codes into holographic cells. Section 6 presents the experimental setup used in projects introduced in sections 6, 7, and 8. Section 7 describes a method for estimating Zernike polynomials using polarimetric mapping images and neural networks. Sections 8 and 9 consist of the most relevant topics to the chosen title for this thesis. A novel technique is introduced in section 8, which can autodetect obscured information in a highly focused electromagnetic field. Section 9 describes a developed application of three-dimensional samples produced by a conventional 3D printer using a sensitive material to the polarization.

1.1. Publications

1.1.1. Chapter books

- 1) **K. Ahmadi**, “Beam implementation with a translucent twisted-nematic liquid crystal display,” P. J. Rosen (Ed.), “Holography- Recent Advances and Applications,” IntechOpen, Rijeka, 2022, Ch. 25. DOI: 10.5772/intechopen.105671.

1.1.2. Journal papers

- 2) **K. Ahmadi** and A. Carnicer, “Optical visual encryption using focused beams and convolutional neural networks” *Opt. Lasers Eng*, 161, 107321 (2023).
- 3) D. Maluenda*, M. Aviñoá*, **K. Ahmadi***, R. Martínez-Herrero, and A. Carnicer, “Experimental estimation of the longitudinal component of a highly focused electromagnetic field,” *Sci Rep* 11, 17992 (2021) [*Equally contributed authors].
- 4) **K. Ahmadi**, P. Latorre-Carmona, B. Javidi, and A. Carnicer, “Polarimetric Identification of 3D-Printed Nano Particle Encoded Optical Codes,” *IEEE Photonics*, 12(3), 1-10 (2020).

1.1.3. Conference papers

- 5) **K. Ahmadi**, A. Carnicer, “Estimation of Zernike polynomials for a highly focused electromagnetic field using polarimetric mapping images and neural network,” in V International Conference on Applications of Optics and Photonics-AOP2022, Guimaraes, Portugal (accepted).
- 6) **K. Ahmadi**, D. Maluenda, and A. Carnicer, “Fast mapping of Double-Pixel Holograms using K-nearest Neighbors,” *OSA Imaging and Applied Optics Congress* [On-line], DW5E.7, 2021.
- 7) **K. Ahmadi**, I. Juvells, A. Carnicer, “On how thick diffusers can contribute to the design of optical security systems,” *Proc. SPIE* 11207, Fourth International Conference on Applications of Optics and Photonics, Lisbon, Portugal, 112071H, 2019.

1.2. Other contributions

- 8) **K. Ahmadi**, “Encoding ASCII codes into an optical beam,” *IONS Ireland 2021* [On-line] (oral presentation).
- 9) M. Aviñoá, D. Maluenda, **K. Ahmadi**, R. Martínez-Herrero, and A. Carnicer, “GUI-Based Phase Retrieval Algorithm for the Reconstruction of the Longitudinal Component of Electromagnetic Beams,” in V International

Conference on Applications of Optics and Photonics-AOP2022, Guimaraes, Portugal (poster presentation).

- 10) D. Maluenda, M. Aviñoá, **K. Ahmadi**, A. Carnicer, and R. Martínez-Herrero, “On the total estimation of the electromagnetic field in the focal area with no interaction with the media,” in V International Conference on Applications of Optics and Photonics-AOP2022, Guimaraes, Portugal (keynote).

2. Introduction

Cryptography is the science of protecting sensitive information by applying a specific algorithm or/and generating keys that it has a long history. Despite the classic encryption methods such as Caesar's encryption technique based on substitution cipher, the invention of electromechanical machines, such as the Enigma rotor machine used during World War II, enhanced encryption. In parallel to enhancing encryption methods, the so-called cryptanalysis has developed the analyzing information system to break down the encryption algorithm. For instance, Al-Kindi invented the frequency analysis technique for breaking monoalphabetic substitution ciphers in the 9th century.

In modern times, Encryption algorithms have become mature, using keys that can be the same (symmetric-key) or different (asymmetric-key) for ciphering and deciphering processes. We can name the Data Encryption Standard (DES) and Advanced Encryption Standard (AES) as two well-known digital encryption standard methods applying a symmetric key, developed from 1970 to 2002. The main disadvantage of symmetric key algorithms is the necessity of a secure channel for exchanging the key between the communicating parties. In 1976, Whitfield Diffie and Martin Hellman introduced a method of distributing cryptographic keys, which sparked asymmetric key algorithms.

In contrast to the symmetric cryptography technique, the public-key cryptography or asymmetric cryptography technique uses a pair of keys, the so-called public and private key, for ciphering and deciphering messages. Hence, authorized people who know the public key can encrypt a message, whereas the encrypted message can be decrypted just with the owner's private key. The security level of this system depends on cryptographic algorithms used for generating the key pairs. Digital signatures for authentication purposes, key distribution, or a combination of both, for instance, the Rivest-Shamir-Adleman (RSA) algorithm, are some applications of the public-key algorithm.

Generally speaking, humans have been trying to secure information by providing new encryption algorithms accompanied by developing the current ones, from the simplest encryption algorithm (Caesar's encryption technique) to the high-advanced and currently used ones such as Transport Layer Security (TLS) and Secure Shell (SSH). In parallel, the vulnerability of the cryptosystems has been assessed and advanced by cryptanalytic methods [1].

Given the enormous increasing use of the Internet and the transfer of information in this digital era, it is crucial to focus on encryption and data

security. Although the main encryption algorithms belong to digital encryption algorithms, the technological advances in optics and photonics and their multiple applications have opened a new cryptosystem class. Many researchers have been urged to apply optics and photonics to encrypt information in the last decades. The use of optical techniques in security applications might be interesting because, on the one side, optical waveforms involve many complex degrees of freedom, such as polarization, amplitude, phase, large bandwidth, quantum properties of photons, and multiplexing that can be combined in many ways to produce high-security information systems. On the other side, optical techniques take advantage of high-speed, parallel, and multidimensional processing.

In advance, optical processing and pattern recognition were developed for authentication purposes [2-7]. Then, in 1995, Réfrégier and Javidi proposed an optical image encryption method, the so-called Double Random Phase Encoding (DRPE) [8,9]. In the DRPE scheme, an image is encrypted into a complex-amplitude stationary white noise using two statistically independent random phase masks at the input and the Fourier plane of a 4f-imaging system. Although the proposed algorithm was relatively straightforward but sparked a new application of optical techniques for encryption systems, in which DRPE can be tracked in many publications [10-23]. Although the basic DRPE scheme demonstrated vulnerability against chosen-cyphertext attacks [24] and known-plaintext attacks [25], several alternatives have been proposed to enhance the security level of the optical systems [26-29].

In general, the security level of the cryptosystem depends on the used key or keys, including the length, design, and randomness. In digital cryptography, keys are introduced based on mathematical algorithms. In contrast, in optical cryptosystems [30-32], designing a key is mainly based on the physical properties of optical processing, for instance, physical keys (such as diffusers), the state of polarization introduced by polarizers and retarders, modulation characteristics of spatial light modulators (SLMs), or combining digital algorithms with optical techniques [33-35].

The phase distribution of light beams plays a significant role in optical security systems due to the disability of sensing by the human eye or recording by conventional cameras such as CCDs. For instance, phase encoding can be implemented with an optical system that works in the Fourier domain [8-10], the fractional Fourier domain [12-14], the Fresnel domain [15-17], or using graytor transform [18,19] which are belong to linear optical systems. Another interesting encryption technique that takes advantage of the phase property of lights is phase imaging or fully-phase encryption by transforming an amplitude-

only image into a phase-only function [36-39] accompanied by techniques for converting phase imaging into an amplitude image or vice versa, for instance, phase retrieval algorithms [40-42] and phase-contrast method [43,44].

Polarization is one of the reconfigurable properties of optical wave fields in which its different states specify the different geometric orientations of transverse wave oscillations. The polarization property of light attracts much attention in optical security systems due to its flexibility in the encryption key design and the encryption process [45-48]. Polarization-encoding systems often take advantage of recording intensities over phase-encoding systems. For instance, utilizing polarization in a phase-based optical encryption system for recording the decoded information with conventional intensity-sensitive detectors [49]. Since liquid crystal displays (LCDs) are polarization-sensitive devices, LCDs play a significant role in polarization encoding systems in which the dynamic generation of spatially variant polarized beams (vector beams) can be achieved [50-55]. Complex information can be encoded in transverse components of an electromagnetic field to introduce polarization masks as secret keys [56-61], or arbitrary data can be encoded in the longitudinal component of a highly focused and non-uniform polarized beam [62,63]. Besides, a technique for generating arbitrary 3D polarization orientation by superposition of a radially polarized beam and an azimuthally polarized beam applied to gold nanorods has been reported to provide an orientation-unlimited polarization encryption system with high security [64]. Regarding the 3D polarization key, the authors in [65] demonstrated the feasibility of 3D polarization multiplexing by optimizing a single vectorial beam using a multiple-signal window multiple-plane phase retrieval algorithm. Another exciting application of polarization encoding is implementing the logical XOR operation using LC-SLMs to encrypt binary images [66,67].

In 2016, Carnicer et al. proposed a numerical approach to encoding information in the longitudinal component of a highly focused beam [62,63]. Despite electromagnetic (EM) plane waves, the tightly convergent wavefront of light provided by propagating through a vectorial diffraction system, for instance, a high numerical aperture (NA) objective lens [68,69], demonstrates a non-zero contribution of the electric field in the direction of propagation. On one side, the longitudinal component cannot be recorded directly using a conventional imaging system [70, 71]. On the other side, the energy ratio between the longitudinal component and transverse ones of a focused EM field is variable from zero to even further than one, depending on the state of the input polarization and physical properties of the concentrated beam. Therefore, the selection of polarization of the input beam is a critical element in designing a

secure optical system based on highly focused fields. Due to the complexity of the experiments and the fact that the longitudinal component should be obtained by its lateral electric field, decoding the original data depends on the quality of retrieving the transverse parts of the electromagnetic field at the observed plane. The practically obtained results often suffer from the misalignment of optical elements, imperfection of polarizers/retarders, some aberrations such as spherical and distortion, and some errors caused by the coupled amplitude-phase modulation. All mentioned errors challenge the decoding process. Since the proposed encoding approach has the same weakness as the DRPE approach, they enhanced the security of the system by applying the photon-counting model [72].

The photon-counting model is a nonlinear transformation that might overcome the vulnerability of linear optical systems. In photon-counting imaging systems, the number of photons reaching each pixel is limited by predefined incident photons [73]. Experimentally, the photon-limited images can be recorded by optical systems that work under low light conditions. Statistically, the photon-limited images can be modeled by the Poisson distribution [74]. This approach is usually used to obtain a sparse representation of encrypted data for verification purposes [59].

Regarding focused fields, we developed a practical method to estimate the longitudinal component of a highly focused beam using a conventional imaging system that might be applied to encrypt data in the axial domain. Furthermore, we introduced a novel approach for encoding and decoding data in the longitudinal component of a highly concentrated beam without the necessity of direct observation of the longitudinal component using a machine learning algorithm and polarimetric mapping images.

One of the most used applications of optical security is related to verification and authentication. The validity of documents, messages, or products is crucial, particularly for commercial, industrial, and military organizations. Document signature is a powerful technique used to determine whether a message is tampered with or valid. For instance, using a specific nanoparticle material doped in inks for security printing [75] or attaching a phase-encoded label with the specifications of an integrated circuit to the microchip package [76]. Hence, the physical support used for identifying the encoded data plays a crucial role in optical authentication approaches [77]. Among different optical techniques for authentication purposes [31], we focused on those authentication schemes that use optically tagged security codes accompanied by machine learning algorithms to classify and verify the optical codes without the necessity of decoding ciphertexts [78-81].

In [78], a quick response (QR) code was sandwiched between a combination of diffusers and glass slides to provide a 3D optical phase mask as physical support. Unique speckle patterns obtained by passing a laser beam through the 3D optical phase mask were classified with statistical analysis and the random forest classifier.

In [79], a QR code made of metal nanoparticles covered with a diffuser was proposed as polarization-sensitive physical support. Polarimetric-signature speckle noises were obtained by passing a linearly polarized laser beam with different polarization directions. A multi-class Support Vector Machine (SVM) algorithm accompanied by speckle patterns analysis successfully distinguished between verified and counterfeit samples.

In [80], QR samples were fabricated by standard lithographic and deposition technologies on flat glass substrates using two different thin films. In thin-film technology, many parameters can be freely selected, such as materials, compositions, homogeneous films, anisotropic films, layer thickness, etc. [82], providing an excellent degree of freedom. Since thin-film structures display distinctive polarization signatures, unique polarimetric-encoded codes were obtained by illuminating samples with a polarized laser beam. The polarimetric codes were measured in imaging and non-imaging systems based on an ellipsometry setup able to measure the Mueller matrix [83]. Particularly, in the more complicated situation, polarimetric-encoded codes were obtained using a linearly polarized beam passing through a phase-encoded anisotropic film in a non-imaging system. The Stokes vectors related to different directions of linearly polarized beams reflected from samples were recorded as a dataset to feed the K-Nearest Neighbors (KNN) classifier [84]. Even though the encoded information was not accessible because of converting to noise distributions, the KNN machine learning algorithm could still authenticate polarimetric codes. Besides, a similar approach has been implemented to authenticate pharmaceutical tablets produced with film-coated gold nanoparticles (AuNP). Since these coated tablets included unique polarimetric signatures, an ellipsometric optical technique accompanied by a machine learning technique successfully distinguished false and authentic ones [81].

As explained above, the combination of polarimetric signatures, specific materials, and machine learning algorithms can distinguish among different samples even in a highly complex scenario. Very often, the number of samples might be restricted due to the production costs associated with these types of technologies. Hence, in this thesis, we developed an intelligent authentication system using commercially accessible materials produced with low-cost technology.

As defined in [85], machine learning is the technique that improves system performance by learning from experience via computational methods. In computer systems, experience exists in the form of data, and the main task of machine learning is to develop learning algorithms that build models from data. By feeding the learning algorithm with experience data, we obtain a model that can make predictions on new observations. In other words, machine learning is a subfield of artificial intelligence that involves developing self-learning algorithms to gain knowledge from that information to make predictions. Instead of requiring humans to manually derive rules and build models from analyzing large amounts of data, machine learning offers a more efficient alternative for capturing the knowledge in data to gradually improve the performance of predictive models and make data-driven decisions [86].

Classical machine learning algorithms can be mainly divided into three types:

- Supervised learning: to learn a model from labeled training data to predict the label of unseen or future data
- Unsupervised learning: to explore the structure of unlabeled input data to extract meaningful information resulting in grouping or clustering of data points
- Reinforcement learning: to develop a system that improves its performance based on interactions with an environment

Classification techniques are a subcategory of supervised learning to predict the categorical class labels of new observations based on the predefined-labeled training dataset.

Deep learning is a subfield of machine learning that has recently become prominent. Deep learning-based algorithms involve the use of concepts from representation learning where various demonstrations of the data are learned in different layers that also aid automated feature extraction in contrast to classical machine learning algorithms, in which vector features must be extracted by applicants using statistical, mathematical, and data mining techniques. As a result, deep learning algorithms make machines more intelligent [87].

As mentioned previously, machine learning techniques can be applied in optical security systems to classify and distinguish authentic and counterfeit samples [78-81]. Besides, the use of machine-learning techniques to attack or evaluate the security of the current cryptosystems has been reported [88-92]. Particularly, recent advances in deep learning have given rise to applying deep learning algorithms in many optical techniques. For instance, applying deep learning in holography and coherent imaging [93-97], wavefront sensing [98,

99], fringe pattern analysis [100], fringe projection profilometry [101], phase unwrapping [102], phase retrieval [103-108], lensless computational imaging [109]. In this regard, we used machine learning algorithms to build an intelligent optical security system.

The final issue that we discuss here is the secret sharing technique. The secret sharing technique is one of the cryptography techniques proposed by Shamir and Bakley independently in 1979 [110,111]. The concept of secret sharing is to split a secret into n shares ($n \geq 2$) in which the secret can only be decoded when all n -shares are accessible, and any $n-1$ shares unmask no information about the secret. In 1989, Desmedt and Frankel developed the basis of secret sharing by introducing threshold cryptography [112]. In threshold cryptography scheme (t, n) , a secret is shared with n shareholders but can only be decrypted by the threshold number of legitimate users, t ($t \leq n$). In this case, if one or a couple of shareholders is not accessible, still the secret can be decoded by a specific number of legitimate users. Furthermore, the visual secret sharing scheme was proposed by Naor and Shamir in 1994 [113]. The proposed method is one of the well-known techniques among visual cryptography techniques. The visual cryptography technique encrypts the visual information, for instance, images, plaintext, etc., in a way that the decoded information appears as a visual image. In this technique, an image is broken up into n image shares ($n \geq 2$), and none of them unmask any information about the original image.

The basic mathematical algorithm used in secret sharing is the Lagrange interpolation theorem which is computationally complex. Since optical techniques take advantage of high-speed, parallel processing, and multidimensional processing, the concept of secret sharing has been used in optical encoding techniques [114-122]. For example, a secret image was encoded (shared) into three statistically independent phase-only masks using an iterative phase retrieval algorithm based on the propagation of a laser beam in the Fresnel domain, without any complicated mathematical operations. Among three phase-encoded masks, the existence of two of them was an essential tool to reveal the secret image at a specific propagation distance. At the same time, a single one unmasked the secret image [114].

3. Review of basic concepts

3.1. Polarization optics

In paraxial optics, beams are approximately transverse electromagnetic waves (TEM) in which their electric-field vectors lie approximately in transverse planes (the plane perpendicular to the optical axis) and have negligible axial components. Hence, the optical field consists of only two orthogonal components in the plane transverse to the direction of propagation. The electric field of the EM field propagating in free space can be obtained by Maxwell's equation [123]

$$\left(\nabla^2 - \frac{1}{c^2} \frac{\partial^2}{\partial t^2} \right) \mathbf{E} = 0, \quad (3.1-1)$$

where ∇^2 is the Laplacian operator, t is the time, and c is the speed of light. The plane wave of Eq. (3.1-1) describes the electric field components as follows:

$$E_x(\mathbf{r}, t) = E_{0x} \cos(\omega t - \mathbf{k} \cdot \mathbf{r} + \varphi_x), \quad (3.1-2a)$$

$$E_y(\mathbf{r}, t) = E_{0y} \cos(\omega t - \mathbf{k} \cdot \mathbf{r} + \varphi_y), \quad (3.1-2b)$$

Where \mathbf{k} is the vector that shows the direction of propagation, \mathbf{r} is the radius vector to a point in the field from the origin of the coordinate system as shown in Fig. (3.1.1a), ω is the angular frequency, E_{0x} and E_{0y} are the maximum amplitudes, and φ_x and φ_y are arbitrary phases. For a plane wave traveling in the z -direction, the electric field lies in the x - y plane, as shown in Fig. (3.1.1b). Correspondingly, Eqs. (3.1-2) can be rewritten as

$$E_x(z, t) = E_{0x} \cos(\omega t - kz + \varphi_x), \quad (3.1-3a)$$

$$E_y(z, t) = E_{0y} \cos(\omega t - kz + \varphi_y), \quad (3.1-3b)$$

where $k = 2\pi/\lambda$ is the wave number. The components $E_x(z, t)$ and $E_y(z, t)$ are sinusoidal oscillations in the x - z and y - z planes, which describe the polarization of light, respectively. Regardless of the time-space propagator $\omega t - kz$, Eqs. (3.1-3) lead to the equation of an ellipse as follows:

$$\frac{E_x(z, t)^2}{E_{0x}^2} + \frac{E_y(z, t)^2}{E_{0y}^2} - \frac{2E_x(z, t)E_y(z, t)}{E_{0x}E_{0y}} \cos \varphi = \sin^2 \varphi, \quad \varphi = \varphi_x - \varphi_y. \quad (3.1-4)$$

This equation describes the polarization ellipse because it refers to polarized light. In general, the electric field of a TEM field can be written as follows:

$$\mathbf{E}(z,t) = E_x(z,t)\hat{X} + E_y(z,t)\hat{Y}, \quad (3.1-5)$$

in which the endpoint of the vector $\mathbf{E}(z,t)$ describes the polarization of the beam (wave) at each position z as a function of time.

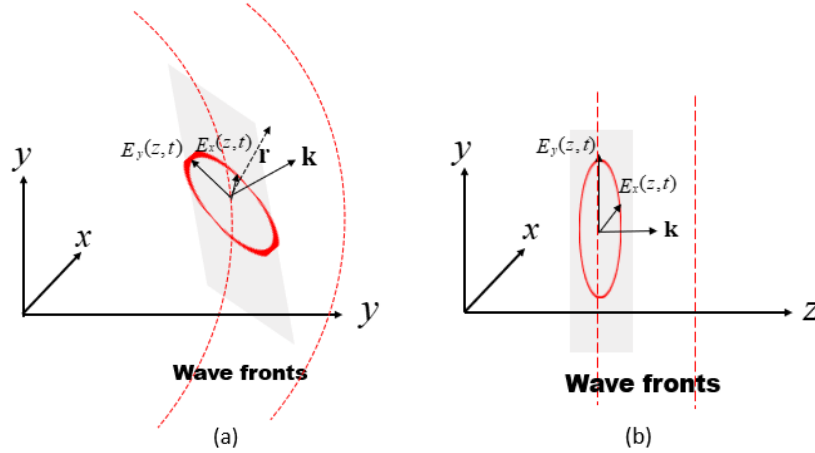


Fig. 3.1.1. (a) Propagation of a transverse electromagnetic wave. The wavefronts of the paraxial field are exaggerated for illustration purposes. The electric field components lie in a plane (gray plane) tangential to the wavefront at the position \mathbf{r} (b) Propagation of a plane wave in the z -direction. Own sketch extracted from [123,124].

The state of polarization of the wave is determined by the orientation and shape of the polarization ellipse, which is expressed by the orientation angle ψ and the ellipticity angle χ , as shown in Fig. (3.1-2). The relationship between these angles and the parameters of the polarization ellipse is given by

$$\tan 2\psi = \frac{2E_{0x}E_{0y}}{E_{0x}^2 - E_{0y}^2} \cos \varphi, \quad 0 \leq \psi \leq \pi \quad (3.1-6a)$$

$$\sin 2\chi = \frac{2E_{0x}E_{0y}}{E_{0x}^2 + E_{0y}^2} \sin \varphi, \quad -\pi/4 \leq \chi \leq \pi/4. \quad (3.1-6b)$$

Moreover, the size of the ellipse is determined by the intensity of the wave equal to $E_{0x}^2 + E_{0y}^2$. In general, the optical field is elliptically polarized, as shown in Fig. (3.1.2), but there are several combinations of amplitude and phase that are especially important. If $E_{0x} = 0$, the light is linearly polarized in the y -direction (LPY). If $E_{0y} = 0$, the light is linearly polarized in the x -direction (LPX). If

$\varphi=0$ or $\varphi=\pi$, the wave still is linearly polarized in which the plane of polarization is rotated as $\arctan(\pm E_{0y}/E_{0x})$ with respect to the x-axis (the + and - signs correspond to $\varphi=0$ and $\varphi=\pi$, respectively). In particular, if $E_{0x}=E_{0y}=E_0$ and $\varphi=0$ or $\varphi=\pi$, the plane of polarization makes an angle $\pm 45^\circ$ with the x-axis denoted by LP ± 45 . If $\varphi=\pm\pi/2$ and $E_{0x}=E_{0y}=E_0$, the wave is right circularly polarized (correspond to $\varphi=\pi/2$) or left circularly polarized (correspond to $\varphi=-\pi/2$) denoted by RCP and LCP, respectively. The right and left correspond to clockwise and counterclockwise rotation of the electric field when viewed from the direction toward which the wave is propagating in the z-direction, respectively.

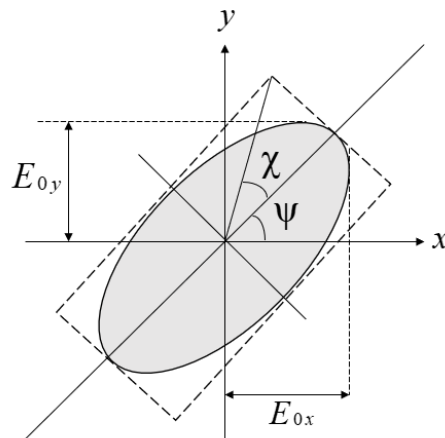


Fig. 3.1.2. Polarization ellipse configuration. Own sketch extracted from [123,124].

The state of polarization of a light wave can be visualized by means of the polarization ellipse. However, practically is not easy to determine the orientation and ellipticity angles regarding the polarization ellipse. Another alternative is what Poincaré proposed in 1892. He defined a sphere, the so-called Poincaré sphere, that is a geometrical construct in which the state of polarization is presented by a point on the surface of a sphere of unit radius, as sketched in Fig. (3.1.3).

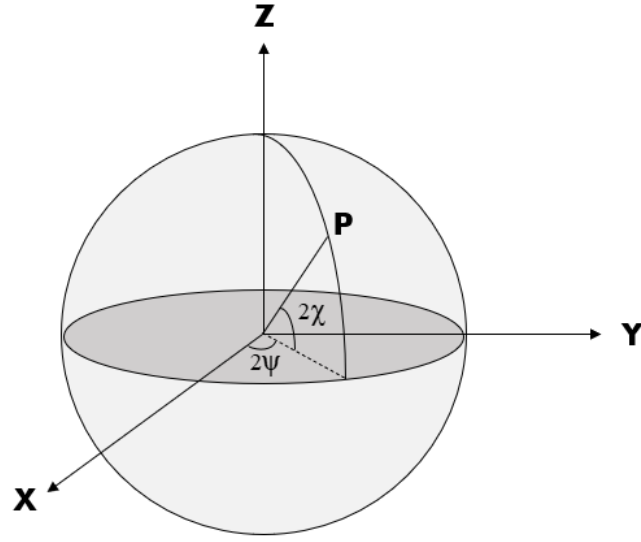


Fig. 3.1.3. The poincaré sphere representation. X, Y, and Z are Cartesian coordinate axes, ψ and χ are the spherical orientation and ellipticity angles, respectively, and P is a point on the surface. Own sketch extracted from [123,124].

The Cartesian coordinates are related to the spherical coordinates as $x = \cos(2\chi)\cos(2\psi)$, $y = \cos(2\chi)\sin(2\psi)$, $z = \sin(2\chi)$ in which $x^2 + y^2 + z^2 = 1$. In this representation, any polarization state can be obtained by the coordinate pair $(2\psi, 2\chi)$. For instance, LPX corresponds to $(0^\circ, 0^\circ)$, LPY corresponds to $(180^\circ, 0^\circ)$, LP+45 corresponds to $(90^\circ, 0^\circ)$, LP-45 corresponds to $(270^\circ, 0^\circ)$, RCP corresponds to $(0^\circ, 90^\circ)$, and LCP corresponds to $(0^\circ, -90^\circ)$, as shown in Fig. (3.1.4). However, the measurable parameter of a wave is intensity, whereas the angle pair $(2\psi, 2\chi)$ does not contain any information about the intensity. To overcome this limitation, Stokes introduced a set of four quantities: S_0 , S_1 , S_2 and S_4 , which are real numbers and measurable, the so-called Stokes polarization parameters. These parameters can be obtained by taking a time average of the polarization ellipse (Eq. (3.1-5)). The time average is defined as $\langle E_i(z,t)E_j(z,t) \rangle = \lim_{T \rightarrow \infty} \frac{1}{T} \int_0^T E_i(z,t)E_j(z,t)dt$, where $i, j = x, y$ and T is the total averaging time. Subsequently, the Stokes parameters are defined as follows:

$$S_0 = E_{0x}^2 + E_{0y}^2, \quad (3.1-7a)$$

$$S_1 = E_{0x}^2 - E_{0y}^2, \quad (3.1-7b)$$

$$S_2 = 2E_{0x}E_{0y} \cos \varphi, \quad (3.1-7c)$$

$$S_3 = 2E_{0x}E_{0y} \sin \varphi, \quad (3.1-7d)$$

where $S_0^2 = S_1^2 + S_2^2 + S_3^2$. In addition, by eliminating the time-space propagator ($\omega t - kz$) in Eqs. (3.1-3), the Stokes parameter can be presented in complex notation as follows:

$$S_0 = E_x E_x^* + E_y E_y^*, \quad (3.1-8a)$$

$$S_1 = E_x E_x^* - E_y E_y^*, \quad (3.1-8b)$$

$$S_2 = E_x E_y^* + E_y E_x^*, \quad (3.1-8c)$$

$$S_3 = j(E_x E_y^* - E_y E_x^*), \quad (3.1-8d)$$

where the components of the electric field are defined as $E_x(t) = E_{0x} \exp(j\varphi_x)$ and $E_y(t) = E_{0y} \exp(j\varphi_y)$. Also, the relationship between the Stokes parameters and the orientation and ellipticity angles regarding the Poincaré sphere is defined as

$$S_1/S_0 = \cos(2\chi) \cos(2\psi), \quad (3.1-9a)$$

$$S_2/S_0 = \cos(2\chi) \sin(2\psi), \quad (3.1-9b)$$

$$S_3/S_0 = \sin(2\chi), \quad (3.1-9c)$$

and subsequently, the orientation and ellipticity angles can be obtained by the Stokes parameters as follows:

$$\psi = \frac{1}{2} \arctan\left(\frac{S_2}{S_1}\right) \quad 0 \leq \psi \leq \pi \quad (3.1-10)$$

$$\chi = \frac{1}{2} \arcsin\left(\frac{S_3}{S_0}\right) \quad -\frac{\pi}{4} \leq \chi \leq \frac{\pi}{4}$$

Therefore, the Cartesian coordinates of the Poincaré sphere can be defined by the Stokes parameters such as $(x, y, z) = (S_1/S_0, S_2/S_0, S_3/S_0)$. The Stokes vector (\mathbf{S}) containing the Stokes parameters as a column matrix completely defines the intensity and the state of polarization of a light wave. For instance,

$$\mathbf{S}_{\text{LPX}} = S_0 \begin{pmatrix} 1 \\ 1 \\ 0 \\ 0 \end{pmatrix}, \mathbf{S}_{\text{LPY}} = S_0 \begin{pmatrix} 1 \\ -1 \\ 0 \\ 0 \end{pmatrix}, \mathbf{S}_{\text{LP+45}} = S_0 \begin{pmatrix} 1 \\ 0 \\ 1 \\ 0 \end{pmatrix}, \mathbf{S}_{\text{LP-45}} = S_0 \begin{pmatrix} 1 \\ 0 \\ -1 \\ 0 \end{pmatrix}, \mathbf{S}_{\text{RCP}} = S_0 \begin{pmatrix} 1 \\ 0 \\ 0 \\ 1 \end{pmatrix}$$

, and $\mathbf{S}_{\text{LCP}} = S_0 \begin{pmatrix} 1 \\ 0 \\ 0 \\ -1 \end{pmatrix}$ are the Stokes vectors correspond to LPX, LPY, LP+45,

LP-45, RCP, and LCP, respectively. The position of the mentioned states of polarization on the Poincaré sphere is shown in Fig. (3.1.4).

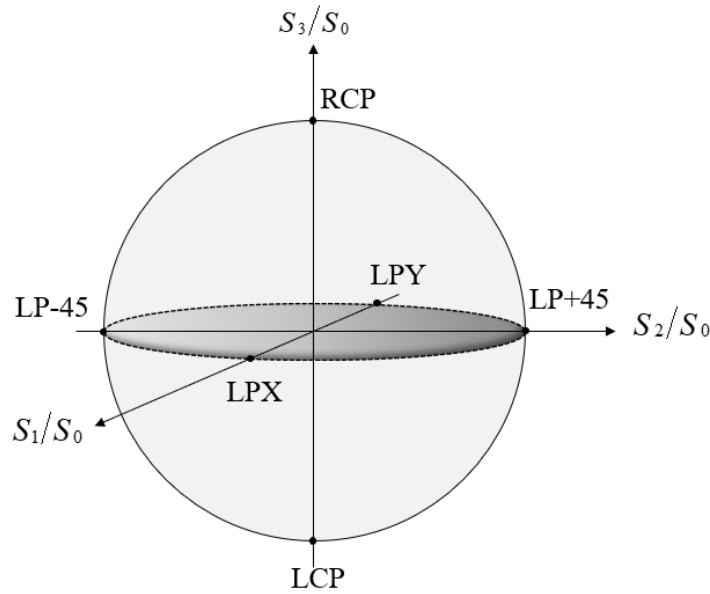


Fig. 3.1.4. Points on the Poincaré sphere represent LPX, LPY, LP+45, LP-45, RCP, and LCP. Own sketch extracted from [123,124].

Note that unpolarized and partially polarized light can also be described using the Stokes parameters. However, unpolarized or partially polarized lights are beyond the scope of this thesis. As previously mentioned, the Stokes parameters are real and measurable with an intensity detector, for instance, a CCD camera. In practice, the four Stokes parameters can be obtained using a wave retarder and a linear polarizer. Figure (3.1.5) demonstrates the experimental setup for obtaining the Stokes parameters.

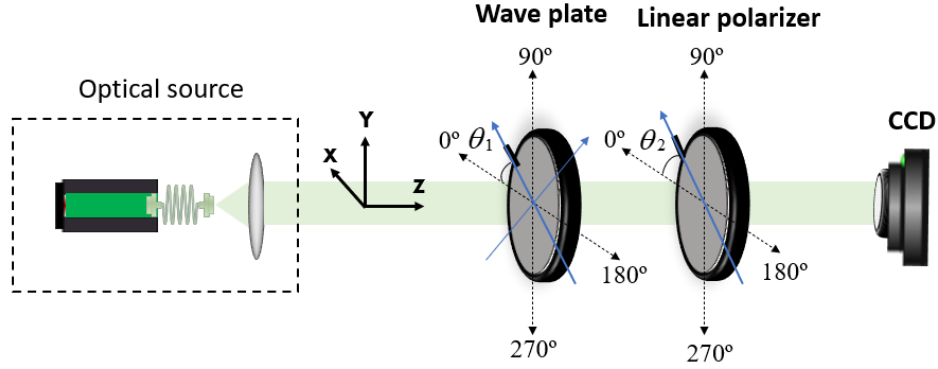


Fig. 3.1.5. The optical setup for measuring the Stokes parameters. The blue arrows demonstrate the transmission axis of the linear polarizer and the axes of the wave plate. Own sketch extracted from [123]

The beam passing through the wave plate experiences a phase shift δ between the orthogonal components. This phase shift depends on the applied wave plate, for instance, for a quarter wave plate (QWP) $\delta = \pi/2$. The linear polarizer transmits the resultant field along its transmission axis at angle θ_2 with respect to the x-axis, and the intensity $I(\theta, \delta)$ on the CCD (or any intensity detector) is given by

$$I(\theta, \delta) = \frac{1}{2} [S_0 + S_1 \cos 2\theta + S_2 \sin 2\theta \cos \delta - S_3 \sin 2\theta \sin \delta], \quad (3.1-11)$$

where $\theta = \theta_2 - \theta_1$. In order to obtain the Stokes parameters S_0 , S_1 , and S_2 we remove the wave plate and place the transmission axis of the linear polarizer at $\theta = 0^\circ$, $\theta = 45^\circ$, $\theta = 90^\circ$, and $\theta = 135^\circ$ to measure $I(0,0)$, $I(45,0)$, $I(90,0)$, and $I(135,0)$. Moreover, to obtain the Stokes parameter S_3 , we place the QWP and fix the axis of the linear polarizer at $\theta_2 = 0^\circ$. In this situation, by rotating the fast axis of the QWP to $\theta_1 = 45^\circ$ and $\theta_1 = 135^\circ$ the intensities $I(45,90)$ and $I(135,90)$ can be obtained. Regarding Eq. (3.1-11) and measured intensities, the Stokes polarization parameters of the incident beam are given by

$$S_0 = I(0,0) + I(90,0), \quad (3.1-12a)$$

$$S_1 = I(0,0) - I(90,0), \quad (3.1-12b)$$

$$S_2 = I(45,0) - I(135,0), \quad (3.1-12c)$$

$$S_3 = I(45,90) - I(135,90). \quad (3.1-12d)$$

In this thesis, Stokes images have been experimentally obtained by the optical setup sketched in Fig. (3.1.5) and Eqs. (3.1-12).

So far, we have considered three equivalent representations for describing the state of polarization of an optical field: the polarization ellipse, Poincaré sphere, and the Stokes vector. Another alternative for this purpose has been introduced by the Jones vector [124]. However, the Jones formulation is restricted to describing only completely polarized light, which fulfills the purpose of this thesis. In the Jones matrix description, the transverse components of an electric field vector are defined as a matrix consisting of two rows and a column given by

$$\mathbf{J} = \begin{bmatrix} E_x \\ E_y \end{bmatrix} = \begin{bmatrix} E_{0x}e^{j\varphi_x} \\ E_{0y}e^{j\varphi_y} \end{bmatrix}. \quad (3.1-13)$$

Subsequently, the intensity can be obtained by the inner product as follows:

$$I = \mathbf{J}^\dagger \cdot \mathbf{J} = \begin{pmatrix} E_x^* & E_y^* \end{pmatrix} \begin{pmatrix} E_x \\ E_y \end{pmatrix} = E_x E_x^* + E_y E_y^*, \quad (3.1-14)$$

where \dagger is the conjugate transpose.

By normalizing the intensity to one, the Jones vectors (matrix) for special polarization states are $\mathbf{J}_{\text{LPX}} = \begin{pmatrix} 1 \\ 0 \end{pmatrix}$, $\mathbf{J}_{\text{LPY}} = \begin{pmatrix} 0 \\ 1 \end{pmatrix}$, $\mathbf{J}_{\text{LP+45}} = \frac{1}{\sqrt{2}} \begin{pmatrix} 1 \\ 1 \end{pmatrix}$, $\mathbf{J}_{\text{LP-45}} = \frac{1}{\sqrt{2}} \begin{pmatrix} 1 \\ -1 \end{pmatrix}$, $\mathbf{J}_{\text{RCP}} = \frac{1}{\sqrt{2}} \begin{pmatrix} 1 \\ j \end{pmatrix}$, and $\mathbf{J}_{\text{LCP}} = \frac{1}{\sqrt{2}} \begin{pmatrix} 1 \\ -j \end{pmatrix}$.

An arbitrary Jones vector \mathbf{J} can be obtained by the superposition of two orthogonal Jones vectors, say \mathbf{J}_1 and \mathbf{J}_2 , in which $\mathbf{J} = a\mathbf{J}_1 + b\mathbf{J}_2$, where a and b can be obtained by $a = \mathbf{J}^* \cdot \mathbf{J}_1$ and $b = \mathbf{J}^* \cdot \mathbf{J}_2$. For instance, an elliptically polarized light can be obtained by the superposition of two orthogonal oscillations of an electric field with arbitrary amplitude and phase as follows:

$$\mathbf{J} = E_{0x}e^{j\varphi_x} \begin{pmatrix} 1 \\ 0 \end{pmatrix} + E_{0y}e^{j\varphi_y} \begin{pmatrix} 0 \\ 1 \end{pmatrix} = \begin{pmatrix} E_{0x}e^{j\varphi_x} \\ E_{0y}e^{j\varphi_y} \end{pmatrix}. \quad (3.1-15)$$

The polarizing elements or polarization devices can be described by 2×2 Jones matrices. Subsequently, if the input and output waves are presented by Jones vectors \mathbf{J}_{inp} and \mathbf{J}_{out} , respectively, the Jones matrix \mathbf{T} which describes the optical system is given by

$$\mathbf{J}_{\text{out}} = \mathbf{T}\mathbf{J}_{\text{inp}}, \quad \mathbf{T} = \begin{pmatrix} t_{11} & t_{12} \\ t_{21} & t_{22} \end{pmatrix}, \quad (3.1-16)$$

where t_{11} , t_{12} , t_{21} , and t_{22} are constants characterizing the device. All linear optical polarization devices obey Eq. (3.1-16). A linear polarizer with a transmission axis in x- and y-direction are represented by the Jones matrices

$$\mathbf{T}_{\text{LPX}} = \begin{pmatrix} 1 & 0 \\ 0 & 0 \end{pmatrix} \text{ and } \mathbf{T}_{\text{LPY}} = \begin{pmatrix} 0 & 0 \\ 0 & 1 \end{pmatrix}, \text{ respectively. The Jones matrix for a wave}$$

retarder with its fast axis along the x-direction is $\mathbf{T}_{\text{WP}} = \begin{pmatrix} 1 & 0 \\ 0 & e^{-j\Delta} \end{pmatrix}$, which

transforms a wave with field components (E_{1x}, E_{1y}) into another with components $(E_{1x}, e^{-j\Delta}E_{1y})$ by imposing a phase delay (Δ) between y and x components. In particular, for a quarter-wave retarder $\Delta = \pi/2$, and for a half-wave retarder $\Delta = \pi$. Another optical polarization devices which are mostly used in optical setups are polarization rotators. Despite the wave retarders, the polarization rotators keep the state of polarization of the input beam but rotate their polarization plane by a particular angle. The Jones matrix for a rotator is

$$\mathbf{T}_{\text{RT}}(\theta) = \begin{pmatrix} \cos \theta & \sin \theta \\ -\sin \theta & \cos \theta \end{pmatrix}. \text{ In addition, for a rotated polarizing element, the}$$

Jones matrix is given by

$$\mathbf{T}(\theta) = \mathbf{T}_{\text{RT}}(-\theta)\mathbf{T}\mathbf{T}_{\text{RT}}(\theta). \quad (3.1-17)$$

As a result, a linear polarizer with a transmission axis rotated by θ with respect to the x-axis is obtained as follows:

$$\mathbf{T}_{\text{LP}\theta}(\theta) = \begin{pmatrix} \cos^2 \theta & \sin \theta \cos \theta \\ \sin \theta \cos \theta & \sin^2 \theta \end{pmatrix}. \quad (3.1-18)$$

Finally, the effect of cascaded optical devices on polarized light is determined by using matrix multiplication formulas, in which a system represented by the Jones matrix \mathbf{T}_1 followed by another represented by the Jones matrix \mathbf{T}_2 can be present as a single device characterized by the product matrix $\mathbf{T} = \mathbf{T}_2\mathbf{T}_1$. In this thesis, linear polarizers and quarter wave-plates are simulated based on the Jones matrix representation.

3.2. Beams in the focal domain: Application to the optical encryption

3.2.1. Fast calculation of the electromagnetic field in the focal domain

In this subsection, we review a flexible implementation of the Debye integral incorporating the effects of the amplitude, phase, and polarization in an overall manner, which takes advantage of rapid numerical evaluation for calculating the amplitude, phase, and polarization of an EM field distribution generated by a high NA microscope objective (MO), which was proposed by Leutenegger et al. [125]. They evaluated the vectorial Debye diffraction integral [126] with the fast Fourier transform for calculating the EM field in the entire focal region instead of direct integration [127,128].

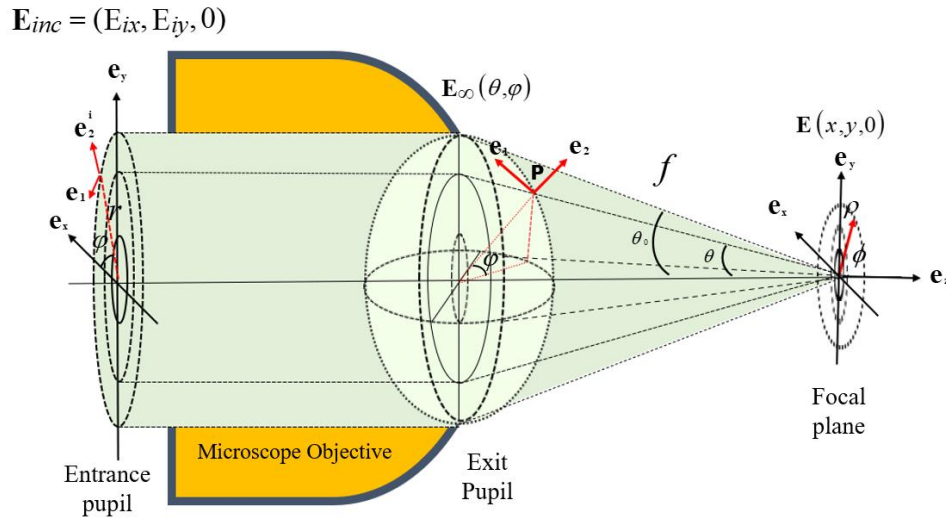


Fig. 3.2.1. The highly focused beam configuration.

To go through the basic formalism based on the Debye diffraction integral and the formulation of this integral as a Fourier transform, consider the basic optical layout and the respective coordinate systems as shown in Fig. (3.2.1). We assume this imaging system obeys Abbe's sine condition. In addition, we assume that a coherent plane wave in parallel to the optical axis crosses the entrance pupil passing through the objective lens and is refracted at the exit pupil and correspondingly focused at the focal plane. The spherical surface at the exit pupil is centered at the focal point (F), and the deflection angle θ at the position P is given by

$$\sin \theta = \frac{r}{R} \frac{NA}{n}, \text{ and } NA = n \sin \theta_0, \quad (3.2-1)$$

where r , R , θ_0 , and n are the off-axis coordinate of the incident wave, the radius of the entrance pupil, the semi-aperture angle, and the refractive index, respectively. Here, we consider the propagation of the electric field in the free space resulting in $n=1$. In Debye approximation, the transmitted EM field at the Gaussian sphere (the spherical surface at the exit pupil) $\mathbf{E}_\infty(r, \varphi)$ is the plane wave spectrum of the focused field $\mathbf{E}(x, y, z)$ near the focal point. Therefore, the electric field in the focal region is defined by integrating the propagated plane waves as follows:

$$\mathbf{E}(x, y, z) = -\frac{if}{2\pi} \iint_{(k_x^2+k_y^2) \leq k^2} \mathbf{E}_\infty(\theta, \varphi) e^{j(k_z z - k_x x - k_y y)} \frac{1}{k_z} dk_x dk_y, \quad (3.2-2)$$

where

$$\mathbf{E}_\infty(\theta, \varphi) = \sqrt{\cos \theta} \left[(\mathbf{E}_{inc} \cdot \mathbf{e}_1) \mathbf{e}_1(\varphi) + (\mathbf{E}_{inc} \cdot \mathbf{e}_2^i) \mathbf{e}_2(\varphi, \theta) \right]. \quad (3.2-3)$$

In Eq. (3.2-2), f is the focal length. Besides, the wave vector $\mathbf{k}(k_x, k_y, k_z)$ in the spherical coordinates (θ, φ) is given by

$$\mathbf{k}(\theta, \varphi) = k \begin{pmatrix} -\cos \varphi \sin \theta \\ -\sin \varphi \sin \theta \\ \cos \theta \end{pmatrix} \text{ where } k = \frac{2\pi}{\lambda}. \quad (3.2-4)$$

The integral in Eq. (3.2-2) is limited to an area where evanescent fields are not included. In Eq. (3.2-3), \mathbf{E}_{inc} is the incident field, in which $\mathbf{E}_{inc} = (E_{ix}, E_{iy}, 0)$, \mathbf{e}_1 and \mathbf{e}_2 are unit vectors in the radial and azimuthal directions, and \mathbf{e}_2 is the projection of \mathbf{e}_2^i on the convergent wavefront surface, as shown in Fig. (3.2.1). The relationship between unit vectors $\mathbf{e}_1, \mathbf{e}_2$ and \mathbf{e}_2^i , and the Cartesian unit vectors $\mathbf{e}_x, \mathbf{e}_y$ and \mathbf{e}_z can be obtained by the following formulas:

$$\mathbf{e}_1(\varphi) = -\sin \varphi \mathbf{e}_x + \cos \varphi \mathbf{e}_y, \quad (3.2-5a)$$

$$\mathbf{e}_2^i(\varphi) = \cos \varphi \mathbf{e}_x + \sin \varphi \mathbf{e}_y, \quad (3.2-5b)$$

$$\mathbf{e}_2(\varphi, \theta) = \sin \theta \sin \varphi \mathbf{e}_x + \sin \theta \cos \varphi \mathbf{e}_y + \sin \theta \mathbf{e}_z. \quad (3.2-5c)$$

Moreover, the wavefront vector is given by

$$\mathbf{s} = (\alpha, \beta, \gamma) = \sin \theta \cos \varphi \mathbf{e}_x + \sin \theta \sin \varphi \mathbf{e}_y - \cos \theta \mathbf{e}_z. \quad (3.2-6)$$

A direct numerical integration considering the coordinate transforms results in the Richard-Wolf integral representation [163,164]. However, Eq. (3.2-2) can be rewritten as a Fourier transform by splitting the phase factor into a lateral and an axial term. Hence, Eq. (3.2-1) can be rewritten as follows:

$$\mathbf{E}(x, y, z) = -\frac{jf\lambda}{4\pi^2} \iint_{(k_x^2 + k_y^2) \leq k^2} (\mathbf{E}_{\infty}(\theta, \varphi) e^{jk_z z / \cos \theta}) e^{-j(k_x x + k_y y)} dk_x dk_y,$$

which finally results in

$$\mathbf{E}(x, y, z) = -\frac{jf\lambda}{4\pi^2} \text{FT}[\mathbf{E}_{\infty}(\theta, \varphi) e^{jk_z z / \cos \theta}], \quad (3.2-7)$$

where FT stands for the Fourier transform operation. Note that the electric field at the focal plane is $\mathbf{E}(x, y, 0)$. The numerical results related to highly focused beams obtained in this Ph.D. thesis are based on calculating Eq. (3.2-7).

3.2.2. Optical encryption in the axial domain

In 2016, Carnicer et al. proposed an optical cryptosystem based on using properties of highly focused beams in addition to the DRPE scheme and a quantum imaging technique [62]. However, their approach is based on a numerical framework that practically requires an algorithm to retrieve the longitudinal component to decode the cipher data. Despite the paraxial waves, a tightly focused EM field demonstrates a non-negligible amount of energy in the direction of propagation in the depth of focus, in which, in some situations, this distribution of the energy is compromised with the distribution of intensity in the lateral directions. Very often, the longitudinal components of highly convergent vector beams are weak and completely embedded by their transverse components. Besides, it is not possible to isolate the irradiance of the longitudinal component using well-known optical techniques, for instance, digital holography or utilizing polarizers. Hence, the unique properties of highly focused beams might be an appropriate tool for hiding and/or securing information.

Regarding Eq. (3.2-7), the EM field at the focal plane ($z=0$) can be rewritten in a compact form as follows:

$$\mathbf{E}(x, y, 0) = \text{FT}_{\lambda f} \left[\frac{\mathbf{E}_\infty}{\cos \theta} \right], \quad (3.2-8)$$

where the subindex λf indicates that spatial frequencies are scaled accordingly, and the constant value in Eq. (3.2-7) is eliminated for the sake of simplicity. By substituting Eq. (3.2-5) in Eq. (3.2-3), the longitudinal component at the exit pupil can be obtained as follows:

$$\mathbf{E}_{z\infty} = \sqrt{\cos \theta} (E_{ix} \cos \varphi + E_{iy} \sin \varphi) \sin \theta, \quad (3.2-9)$$

considering the input field as $\mathbf{E}_{inc} = (E_{ix}, E_{iy}, 0)$. Using Eq. (3.2-9) and Eq. (3.2-8) gives a tool to relate the longitudinal component E_z of the focused field at the focal plane with the transverse components of the input beam at the entrance pupil as follows:

$$E_{ix} \cos \varphi + E_{iy} \sin \varphi = \frac{\sqrt{\cos \theta}}{\sin \theta} \text{FT}_{\lambda f}^{-1} [E_z], \quad (3.2-10)$$

where FT^{-1} indicates the inverse Fourier transform. Taking Eq. (3.2-10) into account, the phase and amplitude distribution of the z-component at the focal plane strongly depend on the phase and amplitude distribution of the transverse components of the plane wave at the entrance pupil. Besides, the transverse components at the entrance pupil are related to each other based on the state of polarization. Hence, information can be encoded in E_z , which the selection of the polarization at the entrance pupil plays a significant role in designing an optical cryptosystem based on a highly focused beam [63]. Since the z-component can not be visualized directly by conventional optical means, E_z can be an appropriate container for encoding data. However, E_z can be obtained numerically through Gauss's theorem.

3.2.2.1. Obtaining the longitudinal component of an EM field from its transverse components

The EM field in free space must satisfy Maxwell's Equations, specifically, the Gauss' theorem

$$\nabla \cdot \mathbf{E}(\mathbf{r}) = 0, \quad (3.2-11)$$

where $\mathbf{E}(\mathbf{r})$ is the electric field, and \mathbf{r} is the position vector. Since here we consider quasi-monochromatic waves, the time dependence is dropped. Regarding plane waves, Gauss' theorem satisfies the transverse condition for the EM field. In other words, the polarization direction of the beam is perpendicular to the direction of propagation. Note that non-homogeneous fields can be considered as a composition of a set of plane waves propagating

in different directions. As a consequence, we cannot strictly talk about the transverse waves due to the direction of propagation is not perfectly defined. Without loss of generality, the EM field $\mathbf{E}(\mathbf{r})$ propagating alongside a reference axis, say the z-axis, can be split into transverse and longitudinal components as follows:

$$\mathbf{E}(\mathbf{r}) = \mathbf{E}_\perp(\mathbf{r}) + E_z(\mathbf{r})\mathbf{e}_z, \quad (3.2-11)$$

where $\mathbf{E}_\perp(\mathbf{r})$ and $E_z(\mathbf{r})$ are the transverse and parallel components to the z-axis, respectively, and \mathbf{e}_z is the unit vector in the direction of the z-axis. By substituting Eq. (3.2-11) into Eq. (3.2-10), the following identity is obtained as

$$\nabla_\perp \cdot \mathbf{E}_\perp(\mathbf{r}) + \frac{\partial E_z(\mathbf{r})}{\partial z} = 0, \quad (3.2-12)$$

with $\nabla_\perp = \mathbf{e}_x \frac{\partial}{\partial x} + \mathbf{e}_y \frac{\partial}{\partial y}$ and $\mathbf{e}_x, \mathbf{e}_y, \mathbf{e}_z$ is an orthogonal triad of unit vectors.

Hence, each component of the EM field can be considered as a superposition of plane waves (for more details, see section 3.2.1) as follows:

$$\left\{ \begin{array}{l} \mathbf{E}_\perp(\mathbf{r}) = \frac{1}{4\pi^2} \int_{-\infty}^{+\infty} \hat{\mathbf{E}}_\perp(\mathbf{k}_\perp; z) e^{j\mathbf{k}_\perp \cdot \mathbf{r}} d^2 k_\perp \\ E_z(z) = \frac{1}{4\pi^2} \int_{-\infty}^{+\infty} \hat{E}_z(\mathbf{k}_\perp; z) e^{j\mathbf{k}_\perp \cdot \mathbf{r}} d^2 k_\perp \end{array} \right., \quad (3.2-13)$$

where $\mathbf{k}_\perp = (k_x, k_y)$ and k_z are the transverse and longitudinal wave-vectors, respectively, satisfying $k^2 = \mathbf{k}_\perp^2 + k_z^2$:

$$\left\{ \begin{array}{l} k_z = \sqrt{k^2 - k_\perp^2} \quad k_\perp^2 \leq k^2 \\ k_z = j\sqrt{k_\perp^2 - k^2} \quad k_\perp^2 > k^2 \end{array} \right. \quad (3.2-14)$$

$\hat{\mathbf{E}}_\perp(\mathbf{k}_\perp; z)$, $\hat{E}_z(\mathbf{k}_\perp; z)$ are the plane wave spectra of the transverse and longitudinal components, respectively. By substituting Eq. (3.2-13) in Eq. (3.2-12), the following equality is obtained

$$j\mathbf{k}_\perp \cdot \hat{\mathbf{E}}_\perp(\mathbf{k}_\perp; z) + \frac{\partial \hat{E}_z(\mathbf{k}_\perp; z)}{\partial z} = 0. \quad (3.2-15)$$

By considering waves propagating through free space, each Cartesian component satisfies its own Helmholtz equation,

$$\nabla^2 \mathbf{E}_i(\mathbf{r}) + k^2 \mathbf{E}_i(\mathbf{r}) = 0, \quad (3.2-16)$$

where $i = x, y, z$. Using the decomposition into plane waves of Eq. (3.2-13) in the Helmholtz equation (Eq. (3.2-16)) gives

$$\frac{\partial^2 \hat{\mathbf{E}}_i(\mathbf{k}_\perp; z)}{\partial z^2} + k_z^2 \hat{\mathbf{E}}_i(\mathbf{k}_\perp; z) = 0, \quad (3.2-17)$$

with the general solution

$$\hat{\mathbf{E}}_i(\mathbf{k}_\perp; z) = \hat{\mathbf{E}}_i(\mathbf{k}_\perp; z=0) \exp(jk_z z). \quad (3.2-18)$$

Introducing Eq. (3.2-18) into Eq. (3.2-15) gives

$$\hat{\mathbf{E}}_z(\mathbf{k}_\perp; z=0) = -\frac{\mathbf{k}_\perp \cdot \mathbf{E}_\perp(\mathbf{k}_\perp; z=0)}{k_z}. \quad (3.2-19)$$

Finally, the longitudinal component in real space is just the inverse Fourier Transform of this spectrum, multiplied by the complex factor $\exp(jk_z z)$

$$E_z(\mathbf{r}) = -\frac{1}{4\pi^2} \int_{k_\perp^2 \leq k^2} \frac{\mathbf{k}_\perp \cdot \hat{\mathbf{E}}_\perp(k_\perp; z=0)}{k_z} e^{jk_z z} e^{j\mathbf{k}_\perp \cdot \mathbf{r}} d^2 k_\perp. \quad (3.2-20)$$

As a result, the longitudinal component of the EM field can be written in terms of just the transverse component, up to a unimodular complex factor.

3.2.2.2 Optical encryption process

The proposed encryption algorithm is explained as follows: Let t be a plain text to be encrypted, RPM_1 and RPM_2 two random phase masks to perform the DRPE scheme. Hence, the encrypted beam reached the entrance pupil is $\text{RPM}_2 \text{FT}_{\lambda_f}[\text{RPM}_1 t]$. Then, the signal is encoded in the longitudinal component, that is, $E_z = \text{FT}_{\lambda_f}[\text{RPM}_2 \text{FT}_{\lambda_f}[\text{RPM}_1 t]]$. Correspondingly, the transverse components of the EM field are encoded as follows [see Eq. (3.2-10)]:

$$E_{ix}^e \cos \varphi + E_{iy}^e \sin \varphi = \frac{\sqrt{\cos \theta}}{\sin \theta} \text{RPM}_2 \text{FT}_{\lambda_f}[\text{RPM}_1 t], \quad (3.2-21)$$

where uppercase e indicates the encoded components. Note that the transverse components at the entrance pupil should be appropriately synthesized to encode information in the z -component of a highly focused EM field. Since the transverse components at the entrance pupil are related to each other regarding the state of polarization, the selection of polarization gives a degree of freedom to manipulate the performance of the encryption system. For instance, if the

input beam is circularly polarized $\mathbf{E}_{inc} = (E_0^e, jE_0^e, 0)$, the synthesized-encoded EM field at the entrance pupil will be

$$E_0^e = \exp(-j\varphi) \frac{\sqrt{\cos\theta}}{\sin\theta} \text{RPM}_2\text{FT}_{\lambda_f}[\text{RPM}_1t], \quad (3.2-22)$$

where $E_{0x}^e = E_0^e$ and $E_{0y}^e = jE_0^e$. If the input beam is radially polarized $\mathbf{E}_{inc} = (E_0^e \cos\varphi, E_0^e \sin\varphi, 0)$, the synthesized-encoded EM field at the entrance pupil will be

$$E_0^e = \frac{\sqrt{\cos\theta}}{\sin\theta} \text{RPM}_2\text{FT}_{\lambda_f}[\text{RPM}_1t], \quad (3.2-23)$$

where $E_{0x}^e = E_0^e \cos\varphi$ and $E_{0y}^e = E_0^e \sin\varphi$.

Since the longitudinal component at the focal plane can not be obtained experimentally with direct observation, the encoded information in the z-component should be obtained numerically from the transverse components at the focal plane, as explained in subsection 3.2.2.1. At the focal plane ($z = 0$), Eq. (3.2-20) can be rewritten based on the Fourier transform as follows:

$$E_z(x, y, 0) = \text{FT}_{\lambda_f} \left[\frac{\alpha \text{FT}_{\lambda_f}^{-1}[E_x(x, y, 0)] + \beta \text{FT}_{\lambda_f}^{-1}[E_y(x, y, 0)]}{\sqrt{1 - \alpha^2 - \beta^2}} \right], \quad (3.2-24)$$

with considering $\gamma = -\sqrt{1 - \alpha^2 - \beta^2}$ (α and β are defined in Eq. (3.2-6)). In this regard, the relationship between the encoded transverse component at the entrance pupil and the transverse components at the focal plane is derived using Eqs. (3.2-3), (3.2-5), and (3.2-8) as follows:

$$E_x^e(x, y, 0) = \text{FT}_{\lambda_f} \left[\frac{1}{\sqrt{\cos\theta}} (E_{0x}^e (\sin^2\varphi + \cos^2\varphi \cos\theta) - E_{0y}^e \sin\varphi \cos\varphi (1 - \cos\theta)) \right] \quad (3.2-25a)$$

$$E_y^e(x, y, 0) = \text{FT}_{\lambda_f} \left[\frac{1}{\sqrt{\cos\theta}} (E_{0x}^e \sin\varphi \cos\varphi (\cos\theta - 1) + E_{0y}^e (\cos^2\varphi + \sin^2\varphi \cos\theta)) \right]. \quad (3.2-25b)$$

Finally, by substituting Eqs. (3.2-25) into Eq. (3.2-24), the encrypted plain text can be decoded as follows:

$$t = \left| \text{FT}_{\lambda_f}^{-1} \left[\text{RPM}_2^* \frac{\alpha \text{FT}_{\lambda_f}^{-1} [E_x^e(x, y, 0)] + \beta \text{FT}_{\lambda_f}^{-1} [E_y^e(x, y, 0)]}{\sqrt{1 - \alpha^2 - \beta^2}} \right] \right|. \quad (3.2-26)$$

Although the intensity pattern of the transverse components, $E_x^e(x, y, 0)$ and $E_y^e(x, y, 0)$, can easily be recorded by a CCD camera, obtaining their phase distributions requires proper techniques such as phase retrieval algorithms or digital holography.

Note that information that reaches the entrance pupil is encoded by means of the DRPE approach, and cipher data is obscured into the inverse Fourier transform of the longitudinal component. Consequently, the encoding system is vulnerable to attacks designed to break down the linear transform optical system. Therefore, they enhanced the security level of the proposed scheme by modeling a photon-limited illumination condition using the photon-counting scheme. As a result, the linearity of the encryption procedure is solved, and the encrypted plain text is no longer accessible, whereas it can be authenticated.

According to the photon-counting model, a low light condition for an optical system can be statistically modeled by Poisson distribution. Thereby, the transverse components obtained by Eqs. (3.2-25) can be encrypted by the Poisson distribution as follows:

$$|E_x^e|^{ph}(x, y) = \begin{cases} 0 & \text{rand}(x, y) \leq \exp(-n_p(x, y)) \\ 1 & \text{otherwise} \end{cases}, \quad (3.2-27)$$

where uppercase *ph* indicates the photon-counting binary version of transverse components, $\text{rand}(x, y)$ is a uniformly distributed random number ranging from 0 to 1, and $n_p(x, y)$ is the normalized irradiance at pixel (x, y) given by

$$n_p(x, y) = \frac{N_p |E_x^e(x, y)|^2}{\sum_{n,m=1}^{N,M} |E_x^e(n, m)|^2}, \quad (3.2-28)$$

where N_p is the predetermined number of photon counts in the entire scene, and $N \times M$ is the total number of pixels. Note that $|E_y^e|$ is encrypted in the same way. Besides, the amplitudes of the transverse components are encrypted using Eqs. (3.2-27) and (3.2-28), but their phase remain unchanged as follows:

$$E_x^{ph} = |E_x^e|^{ph} \frac{E_x^e}{|E_x^e|} \quad (3.2-29)$$

and

$$E_y^{ph} = |E_y^e|^{ph} \frac{E_y^e}{|E_y^e|}. \quad (3.2-30)$$

Finally, the photon-limited plain text t^{ph} can be obtained by applying Eqs. (3.2-27) to (3.2-30) into Eq. (3.2-26). Although t^{ph} can not reveal the original information of the plain text t , the contained information can be verified by the correlation coefficient ρ given by

$$\rho(x, y) = \frac{\sum_{n,m=1}^{N,M} [t^{ph}(m+x, n+y) - \langle t^{ph} \rangle][t(m, n) - \langle t \rangle]}{\sqrt{\sum_{n,m=1}^{N,M} [t^{ph}(m, n) - \langle t^{ph} \rangle]^2 \sum_{n,m=1}^{N,M} [t(m, n) - \langle t \rangle]^2}}, \quad (3.2-31)$$

where $\langle \dots \rangle$ represents the mean value.

3.3. Computer-generated hologram: Double-pixel Arrizón's approach

Arrizón's approach is a type of cell-oriented computer-generated hologram (CGH) encoding. In the cell-oriented method, each encoding point is split into a couple of holographic cells [129,130]. Arrizón proposed a modification of the previous works regarding a double-phase CGH method with an on-axis reconstruction field [131-133]. His approach improved the signal-to-noise ratio (SNR) in the reconstruction plane using two pixels of SLM to encode one holographic cell [134]. Since then, he generalized his encoding method to produce a more symmetric and high-SNR-signal domain using four pixels rather than two pixels of SLM, the so-called the modified Double-Pixel Hologram (DPH) [135]. Nevertheless, his approach was suited for encoding information on phase-only SLMs. Also, he adjusted his method to encode complex modulation with a transmission TNLC as a low-resolution spatial light modulator [136-138].

In this subsection, we first describe the DPH Arrizón's approach to expanding the accessible modulations beyond the restricted SLM response. Then, we review the modified DPH approach by applying 4 pixels to encode one holographic cell adapted to an experimentally obtained modulation curve. In this regard, we aim to produce an on-axis computer-generated hologram with the optimum reconstruction efficiency, maximum signal bandwidth, and high SNR suitable for encoding arbitrary complex modulation into a low-resolution TNLC display.

Here, we consider a phase-mostly modulation curve, as shown in Fig. (3.3.1). The experimental way to obtain this modulation curve is introduced in section 4. We assume that each complex modulation point belongs to the modulation curve as follows:

$$M_g = |M_g| \exp(j\psi_g), \quad (3.3-1)$$

where subscript g denotes 8-bit integer gray values ranging from 0 to 255. In addition, regarding the pixelated structure of the display, we consider the display as a matrix with $N \times M$ pixels. The modulation M_{nm} at the (n, m) th pixel can be described by

$$M_{nm} = |M_{nm}| \exp(j\psi_{nm}). \quad (3.3-2)$$

To encode a desired complex modulation value

$$q_{nm} = |q_{nm}| \exp(j\tau_{nm}), \quad (3.3-3)$$

Arrizón employed the holographic double pixel shown in Fig. (3.3.2), whose pixels have complex modulations M_{nm}^1 and M_{nm}^2 that belong to the modulation curve. As shown in Fig. (3.3.2), the holographic cell is equal to a double pixel with the encoded modulation q_{nm} plus an error double pixel, with modulation values e_{nm}^1 and e_{nm}^2 .

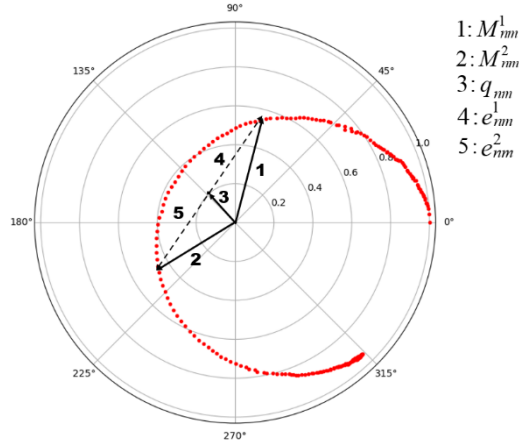


Fig. 3.3.1. The pair of modulation points on the modulation curve in order to encode an arbitrary complex value in the (n, m) th pixel. Figure from [139] under the CC Attribution 3.0 Unported License.

The conditions required to produce an on-axis signal reconstruction with a null contribution of the error term at the zero frequency are as follows:

$$q_{nm} = (M_{nm}^1 + M_{nm}^2)/2, \quad (3.3-4a)$$

$$e_{nm}^2 = -e_{nm}^1. \quad (3.3-4b)$$

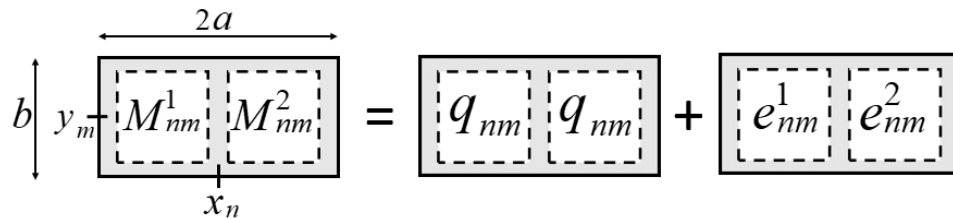


Fig. 3.3.2. The DPH configuration. Own sketch extracted from [136]

Consequently, we can access the modulation points (q) beyond the restricted SLM responses (M_g), as shown in Fig. (3.3.1). Considering the modulation points on the modulation curve (M_g) as a vector with the origin of the polar plot shown in Fig. (3.3.1), encoded modulation points (q) are obtained by the average of the superposition of vectors M^1 and M^2 . Consequently, the modulation errors are $e_{nm}^1 = M_{nm}^1 - q_{nm}$ and $e_{nm}^2 = M_{nm}^2 - q_{nm}$ which lead to Eq. (3.3-4b).

To go through Arrizón's approach in more detail, we assume that the transmittance of the CGH that can be displayed on the LCD is

$$h(x, y) = \sum_{n,m} M_{nm} w(x - np, y - mp), \quad (3.3-5)$$

where p is the pixel pitch, and $w(x, y) = \text{rect}(x/a)\text{rect}(y/b)$. Considering the CGH is intended to encode the spatially quantized complex function

$$q(x, y) = \sum_{nm} q_{nm} w(x - np, y - mp), \quad (3.3-6)$$

where q_{nm} is defined in Eq. (3.3-3), and $|q_{nm}| \leq 1$. Let us assume the spectrum of $q(x, y)$, denoted $Q(u, v)$, is centered at the zero frequency $(u, v) = (0, 0)$. Hence, the CGH transmittance must be related to the encoded complex modulation $q(x, y)$ by the following expression:

$$h(x, y) = A_0 q(x, y) + e(x, y), \quad (3.3-7)$$

where A_0 is the SLM amplitude modulation, which fulfills $\max\{|q_{nm}|\} = \min\{A_0\}$. Then, the Fourier transform of Eq. (3.3-6) gives

$$H(u, v) = A_0 Q(u, v) + E(u, v). \quad (3.3-8)$$

The error spectrum, $E(u, v)$, should be negligible within the largest possible bandwidth centered at the zero frequency to obtain a high SNR, so Arrizón proposed an error function as follows:

$$e(x, y) = l(x, y)g(x, y), \quad (3.3-9a)$$

$$l(x, y) = \sum_{n,m} l_{nm} w(x - np, y - np), \quad (3.3-9b)$$

$$g(x, y) = \sum_{n,m} g_{nm} w(x - np, y - np). \quad (3.3-9c)$$

He demonstrated that the optimal choice $l(x, y)$ is binary grating with discrete

modulation $l_{nm} = (-1)^{n+m}$. Accordingly, the Fourier transform of the error function, which is contributed by the noise field, is given mainly by four off-axis replicas of the function $G(u, v)$ centered at the spatial frequency coordinates $(1/2p, 1/2p)$, $(-1/2p, 1/2p)$, $(1/2p, -1/2p)$, $(-1/2p, -1/2p)$.

Therefore, the reconstructed field with a zero noise contribution places on the optical axis, whereas symmetric off-axis error contributions occur far enough from the optical axis at the Fourier plane, which can be removed using a 4-f spatial filtering system. According to Eqs. (3.3-5) to (3.3-9), $g(x, y)$ is specified by its discrete modulation l_{nm} , which is related to the CGH modulation by the formula

$$M_{nm} = A_0 q_{nm} + (-1)^{n+m} g_{nm}. \quad (3.3-10)$$

Since both function $q(x, y)$ and $g(x, y)$ have on-axis spectrum bands, their variation should be negligible when the increment ($\Delta n = 1$) in x is of the order of the pixel pitch. To satisfy this condition, Arrizón proposed to establish the discrete function g_{nm} such that both complex vectors,

$$M_{nm}^1 = A_0 q_{nm} + g_{nm}, \quad (3.3-11a)$$

$$M_{nm}^2 = A_0 q_{nm} - g_{nm}, \quad (3.3-11b)$$

belong to the SLM modulation curve. Note that Eqs. (3.3-11) are the general form of Eqs. (3.3-4). The constant value A_0 is the maximum possible amplitude, for instance, the radius of a circle to fulfill complex amplitude-phase modulation, in which the average of each pair of modulation points (M_{nm}^1, M_{nm}^2) on the modulation curve should be an interior point inside this circle. As a result, the pair of modulation points (M_{nm}^1, M_{nm}^2) always exist. The maximum CGH efficiency is related to the maximum possible value A_0 . Since the set of the modulation points is finite and discrete, we should find the nearest accessible complex value denoted q_{nm}^a to the desired complex value $A_0 q_{nm}$. Thus, we select the pair modulation points (M_{nm}^1, M_{nm}^2) in such a way that its middle point has the minimum Euclidean distance ε_{nm} from the desired complex value regarding each holography cell as

$$\varepsilon_{nm} = \min |A_0 q_{nm} - q_{nm}^a|. \quad (3.3-12)$$

The remaining issue is to select the position of M_{nm}^1 and M_{nm}^2 with respect to each other on the modulation plot. In this regard, there are two possibilities:

- Selection 1: M_{nm}^1 performs a clockwise rotation (smaller than 180°) of the radial line that contains q_{nm}^a , which M_{nm}^1 has a phase smaller than M_{nm}^2 , as demonstrated in Fig. (3.3.3a).
- Selection 2: M_{nm}^1 performs a counterclockwise rotation of this radial line, which M_{nm}^2 has a phase smaller than M_{nm}^1 , as demonstrated in Fig. (3.3.3b).

On one side, he showed that the appropriate position-selection of the pair modulation points to encode a discrete modulation $q_{nm} = |q_{nm}| \exp(j\tau_{nm})$, where both the modulus $|q_{nm}|$ and the phase τ_{nm} are soft or quasi-continuous functions, is a way explained in selection 1, which leads to

$$M_{nm} = \begin{cases} M_{nm}^1 & (n+m)\text{even} \\ M_{nm}^2 & (n+m)\text{odd} \end{cases} \quad (3.3-13)$$

This configuration is shown in Fig. (3.3.4). On the other side, he proved that the appropriate position-selection for the pair modulation points to encode complex functions of the type

$$q_{nm} = r_{nm} \exp(j\tau_{nm}^0), \quad (3.3-14)$$

is as follows:

$$M_{nm} = \begin{cases} \begin{cases} M_{nm}^1 & (n+m)\text{even} \\ M_{nm}^2 & (n+m)\text{odd} \end{cases} & r_{nm} \geq 0 \\ \begin{cases} M_{nm}^2 & (n+m)\text{even} \\ M_{nm}^1 & (n+m)\text{odd} \end{cases} & r_{nm} < 0 \end{cases} \quad (3.3-15)$$

In Eq. (3.3-14), both r_{nm} (which is a real factor) and phase τ_{nm}^0 are quasi-continuous functions. This configuration is shown in Fig. (3.3.5). The top half of Fig. (3.3.5) (area U) corresponds to $r \geq 0$, and the bottom half (area D) to $r < 0$. This encoding algorithm is also appropriate for encoding continuous functions of the type $F(r, \theta) = R(r) \exp(jt\theta)$, where t is the topological charge, (r, θ) are polar coordinates, and $R(r)$ is a real function of the radial coordinate. In addition, if we intend to encode the complex function $F_{nm} = |r_{nm}| \exp(j\theta_{nm})$, the sampling point of this function should be defined as $r_{nm} = (x_{nm}^2 + y_{nm}^2)^{1/2}$, $x_n = 2np$ $y_n = 2mp$, $-N/2 \leq n < N/2$, and $-M/2 \leq m < M/2$. Note that the pixel size of the function is twice the pixel size of the applied LCD, in which

four pixels of the LCD encode one holographic cell, as shown in Figs (3.3.4) and (3.3.5).

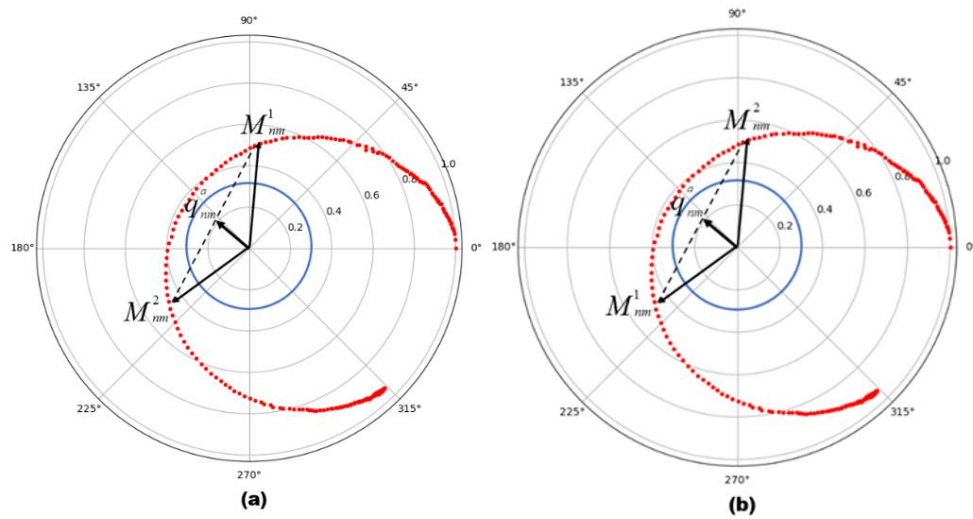


Fig. 3.3.3. (a) Selection 1. (b) Selection 2. Figure from [139] under the CC Attribution 3.0 Unported License.

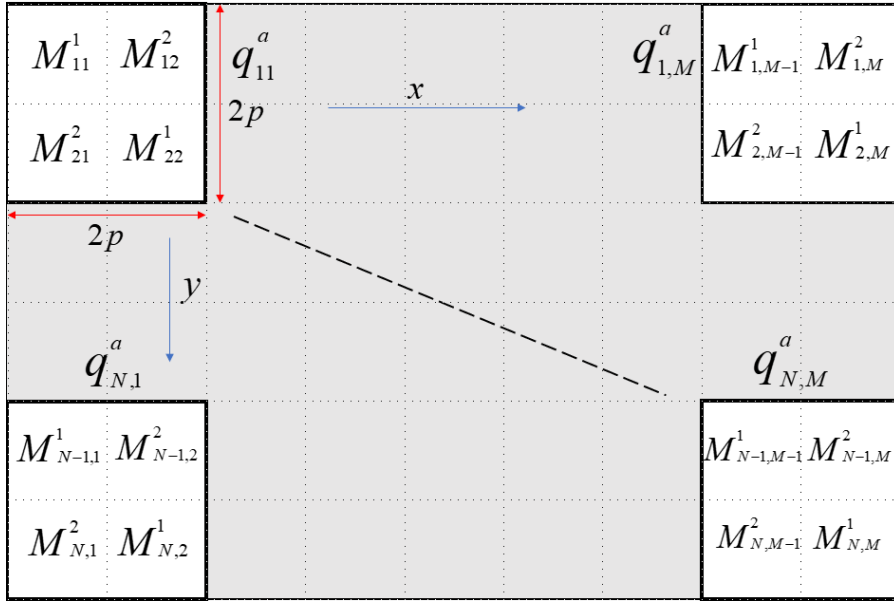
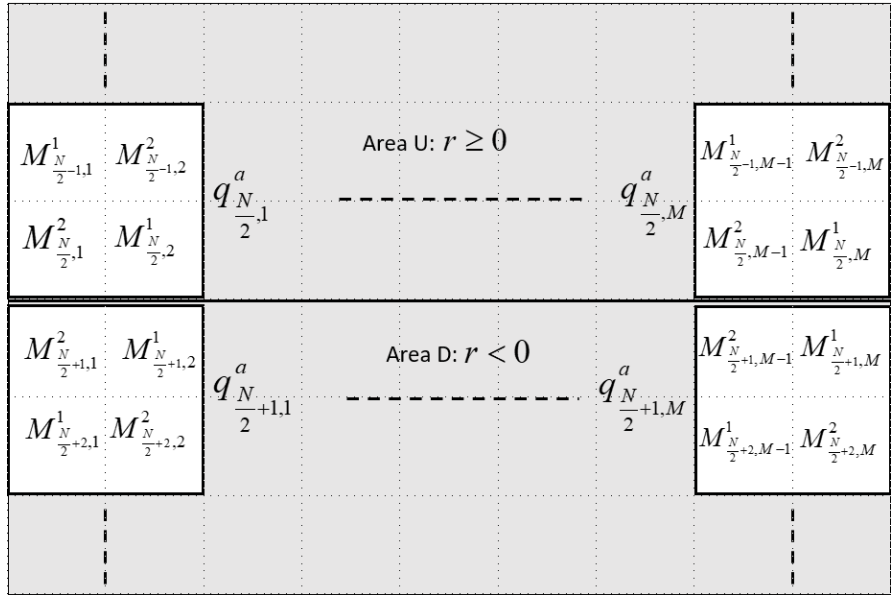


Fig. 3.3.4. The representation of the modified DPH at the LCD plane regarding selection 1.
Figure from [139] under the CC Attribution 3.0 Unported License.



3.3.5. The representation of the modified DPH at the LCD plane regarding selections 1 and 2.
The order of the distribution of values M_{nm}^1 and M_{nm}^2 in the transition area from U to D is changed. Figure from [139] under the CC Attribution 3.0 Unported License.

3.4. Phase retrieval algorithm

In this subsection, we review the iterative phase retrieval algorithm proposed by Fienup [41]. He demonstrated an iterative approach to reconstructing a general object from the modulus of its Fourier transform in order to solve the phase problem of the optical-coherence theory. The reconstructed digital method can be described as follows: Let $f(\mathbf{x})$ be the object and $F(\mathbf{u})$ its Fourier transform:

$$F(\mathbf{u}) = |F(\mathbf{u})| \exp(j\psi(\mathbf{u})) = \text{FT}[f(\mathbf{x})], \quad (3.4-1)$$

where the vector position \mathbf{x} represents a two-dimensional spatial coordinate and \mathbf{u} spatial frequency. The iterative algorithm requires prior knowledge of the problem, for instance, considering $f(\mathbf{x})$ as a real and nonnegative function, and the Fourier modulus ($|F(\mathbf{u})|$) is known. Fienup modified the original Gerchberg-Saxton algorithm [40] by setting a new set of object constraints. The principal constraints are that the object is nonnegative, and the diameter of the retrieved object is enforced not to exceed the known diameter (which can be obtained by the half diameter of the autocorrelation). The general iterative phase retrieval algorithm (the Gerchberg-Saxton algorithm) can be summarized as follows:

1. To start the iterations using a random estimation of the object $g_1(\mathbf{x})$
2. To apply the Fourier transform to $g_1(\mathbf{x})$ resulting $G_1(\mathbf{u}) = |G_1(\mathbf{u})| \exp(j\phi_1(\mathbf{u}))$
3. To reserve the obtained phase $\phi_1(\mathbf{u})$ and substitute $|G_1(\mathbf{u})|$ with the known Fourier modulus $|F(\mathbf{u})|$
4. To apply the inverse Fourier transform to $G'_1(\mathbf{u}) = |F(\mathbf{u})| \exp(j\phi_1(\mathbf{u}))$ resulting $g'(\mathbf{x})$
5. To form a new estimate of the object using the object-domain constraints:

$$g(\mathbf{x}) = \begin{cases} g'(\mathbf{x}) & x \notin \gamma \\ 0 & x \in \gamma \end{cases}, \quad (3.4-2)$$

in which γ indicates the region that all points corresponding with $g'(\mathbf{x})$ violate the constraints. The iteration can be continued by repeating steps 2 to 5 and monitoring the mean square error (MSE) at each iteration in the Fourier domain defined by

$$E_F^2 = \frac{\int \int_{-\infty}^{\infty} [|G_k(\mathbf{u})| - |F(\mathbf{u})|]^2 d\mathbf{u}}{\int \int_{-\infty}^{\infty} |F(\mathbf{u})|^2 d\mathbf{u}}, \quad (3.4-3)$$

where k indicates the k th iteration. In the object domain, the MSE is defined as

$$E_0^2 = \frac{\int \int_{\gamma} [g'_k(\mathbf{x})]^2 d\mathbf{x}}{\int \int_{-\infty}^{\infty} [g'_k(\mathbf{x})]^2 d\mathbf{x}}. \quad (3.4-4)$$

This approach is the so-called error-reduction approach. The disadvantage of this approach is a slow convergence to the solution, which requires a large number of iterations. In order to speed up the convergence process, Fienup developed an efficient approach, the so-called input-output approach, by defining a new constraint in the object domain. The iterative steps in the input-output approach are the same as those defined in steps 1 to 4, but step 5 is modified. The block diagram of the error reduction and the input-output approaches are shown in Figs. (4.1a) and (4.1b), respectively. As shown in Fig. (4.1b), the operation can be considered as a nonlinear system with an input $g(\mathbf{x})$ and output $g'(\mathbf{x})$. In other words, instead of modifying the last output, as in Eq. (3.4.2), the previous input can be modified to form a new input. Thereby, to drive the output to be nonnegative, a logical selection for the next input would be as follows:

$$g_{k+1}(\mathbf{x}) = \begin{cases} g_k(\mathbf{x}) & x \notin \gamma \\ g_k(\mathbf{x}) - \beta g'_k(\mathbf{x}) & x \in \gamma \end{cases} \quad (3.4-5)$$

where β is a constant. A method for choosing $g_{k+1}(\mathbf{x})$ is required depending on the different applications and different trade-offs inherent in the input-output approach. For instance, he demonstrated that a successful method for choosing $g_{k+1}(\mathbf{x})$ is a combination of the first line of Eq. (3.4-2) and the second line of Eq. (3.4-5). Also, he found out that the iterative algorithm works better by changing the method of choosing $g_{k+1}(\mathbf{x})$ after a few iterations rather than applying a method for all the iterations.

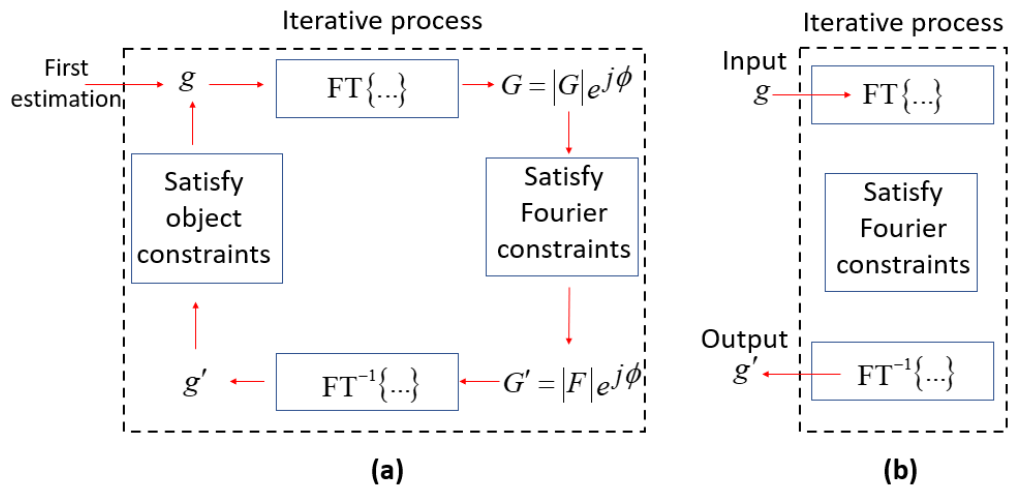


Fig. 3.4.1. (a) Block diagram of the error-reduction approach (Gerchberg-Saxton algorithm), (b) block diagram of the input-output system. Own sketch extracted from [41].

3.5. Machine learning

As defined in [86], machine learning is the application and science of algorithms that make sense of data, which is, arguably, the most exciting field of all the computer sciences. Using self-learning algorithms from the field of machine learning, we can turn data into knowledge. Despite manual approaches to infer rules and build models from processing a large amount of data, machine learning is able to capture the knowledge in data to gradually improve the performance of predictive models and make data-driven decisions. Among three main types of machine learning algorithms: supervised, unsupervised, and reinforcement learning, here we review those algorithms which belong to the supervised learning used in this thesis.

The main application of supervised learning is classification. The classification task is to classify the known data into discrete class labels in order to predict the categorical class labels of new observations. The known data used for training the machine is called the training dataset, and those known data which is not used for training the machine but used for estimating the predictive model is called the test dataset. The whole known dataset is often randomly split into two categories: the training dataset and the test dataset with a ratio of 80:20 or 70:30, respectively [140]. The predictive model is developed and optimized using the training dataset, whereas the test dataset is used to measure the performance of the final model. One of the most used metrics for evaluating the performance of the model is accuracy, the proportion of the number of the correctly predicted class labels by the model over the number of the whole test dataset. Then, the developed predictive model achieving high accuracy is ready to predict the class label of unseen data (new data). This classification process is summarized in the sketch shown in Fig. (3.5.1).

One of the most crucial steps in any machine learning application is to get raw data into a proper shape; this step is called pre-processing. To explain this, let us consider the dataset collected from a hospital. The number of examined patients is considered as the number of samples. Each patient is independently analyzed, for instance, with the temperature of the body, blood pressure, age, weight, etc., which provide a set of features regarding each sample (patient). This set of data shapes a matrix with a size of $N\text{-sample} \times M\text{-feature}$, where N is the number of samples (patients), and M is the number of features (the temperature, blood pressure, etc.). To generalize this, let us use a matrix and vector notation to refer to the dataset.

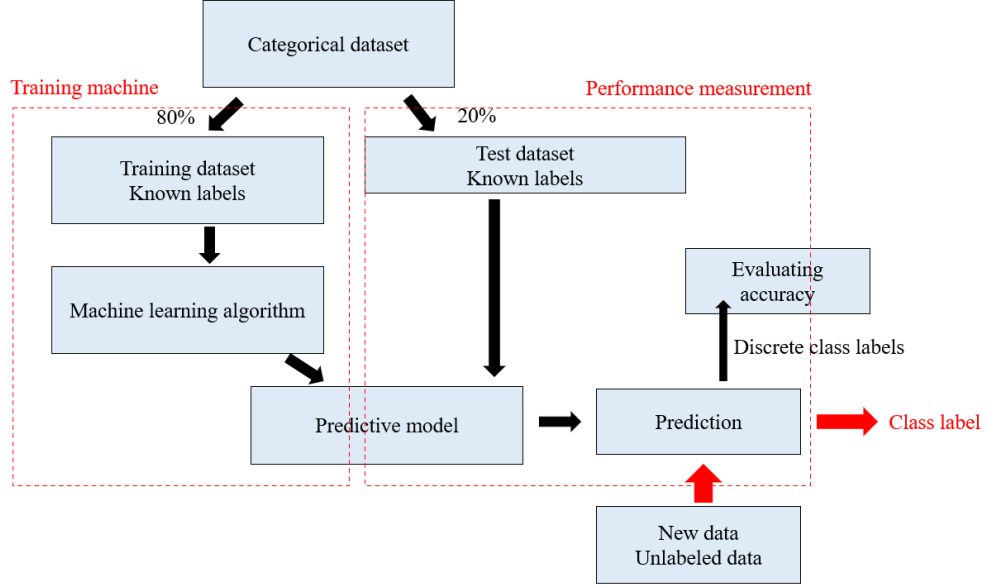


Fig. 3.5.1. The process of training and evaluating the machine. Own sketch extracted from [86].

Regarding N samples and M features, the feature matrix indicated by $\mathbf{X}_{N \times M}$ is presented as follows:

$$\mathbf{X}_{N \times M} = \begin{bmatrix} x_1^{(1)} & x_2^{(1)} & \cdot & \cdot & \cdot & x_{M-1}^{(1)} & x_M^{(1)} \\ x_1^{(2)} & x_2^{(2)} & \cdot & \cdot & \cdot & x_{M-1}^{(2)} & x_M^{(2)} \\ \cdot & \cdot & & & & \cdot & \cdot \\ x_1^{(n)} & x_2^{(n)} & \cdot & \cdot & \cdot & x_{M-1}^{(n)} & x_M^{(n)} \\ \cdot & \cdot & & & & \cdot & \cdot \\ \cdot & \cdot & & & & \cdot & \cdot \\ x_1^{(N)} & x_2^{(N)} & \cdot & \cdot & \cdot & x_{M-1}^{(N)} & x_M^{(N)} \end{bmatrix}, \quad (3.5-1a)$$

where $x_m^{(n)}$ represents the feature m regarding the sample n , in which $n \in [1, N]$ and $m \in [1, M]$. Each row of the feature matrix is called the feature vector of the corresponding sample. The feature vector extraction is a significant step for achieving a successful classification purpose in which these features can be obtained by statistical approaches, image or signal processing, and data mining, depending on the data type. Note that the feature vectors in deep learning algorithms are extracted by the used model without the necessity of applying the mentioned analysis.

Furthermore, the class labels or variable targets should be placed in a column matrix indicated by \mathbf{Y} as follows:

$$\mathbf{Y} = \begin{bmatrix} y_l^{(1)} \\ \cdot \\ \cdot \\ y_l^{(n)} \\ \cdot \\ \cdot \\ y_l^{(N)} \end{bmatrix}, \quad (3.5-1b)$$

where $y_l^{(n)}$ represents the class label of the sample n , and it is labeled from 0 to the number of classes. In addition, to reach an optimal performance of machine learning algorithms is necessary to scale the selected features similarly, for instance, by transforming the features in the range $[0,1]$ or a standard normal distribution.

After preparing data applicable for the machine, the learning algorithm should be appropriately selected corresponding to the problem. The three supervised machine learning algorithms: K-Nearest Neighbors (KNN), Support Vector Machine (SVM), and Convolutional Neural Network (CNN), applied in this thesis are described in the following subsections.

3.5.1. K-Nearest Neighbors

K-nearest neighbor classifier is a type of nonparametric supervised machine learning algorithm. Based on parametric models, new data can be classified without the necessity of the original training dataset. On the contrary, the nonparametric models can not be characterized by a fixed set of parameters, and the number of parameters grows with the training dataset. In parametric models, the machine learns a function from the training dataset, whereas the nonparametric models memorize the training dataset instead of learning a discriminative function from them. Although the KNN algorithm is relatively straightforward, but is powerful and can be used in various complex scenarios. This technique aims to train a dataset to label them into different known classes based on defined features. This algorithm can be described in three main steps:

1. To select the optimum number of neighbors k and a distance metric
2. To find the k nearest neighbors of the sample to be classified
3. To predict the class label by majority vote.

In those cases where there is no majority vote, the machine predicts the class label based on the defined weight.

For instance, we assume training datasets that are labeled with three classes (as shown in three different colors in Fig. (3.5.2)), and each sample is characterized by two features (x_1, x_2). As shown in Fig. (3.5.2), a new data point which is indicated by (?) is predicted as green color (class label) based on majority voting among its seven nearest neighbors ($k = 7$).

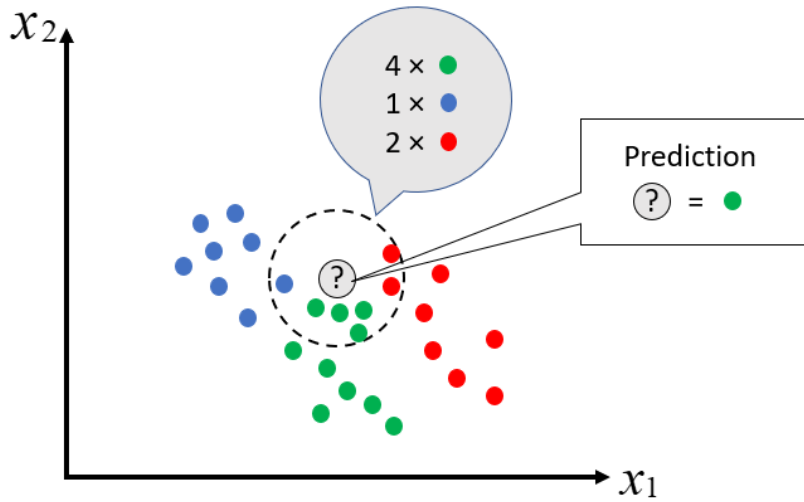


Fig. 3.5.2. The distribution of training datasets is shown with colored points in the feature spaces x_1 and x_2 . The sample points are classified with the KNN classifier in three different classes shown with three different colors. The new sample point indicated by (?) is predicted as a green color (class) based on majority voting among its seven nearest neighbors. Own sketch extracted from [86].

The optimum number of neighbors should be searched to find a good balance between over- and underfitting. In addition, a distance metric should be selected properly based on the feature vectors. The distance between k nearest neighbors can be measured by Minkowski distance which is a generalization of the Euclidean and Manhattan distance. The Minkowski distance of order p between two sample points $\mathbf{x}^{(1)} = (x_1^{(1)} \ x_2^{(1)} \ \dots \ x_M^{(1)})$ and $\mathbf{x}^{(2)} = (x_1^{(2)} \ x_2^{(2)} \ \dots \ x_M^{(2)})$ is defined as follows:

$$d(\mathbf{x}^{(1)}, \mathbf{x}^{(2)}) = \left(\sum_{i=1}^M |x_i^{(1)} - x_i^{(2)}|^p \right)^{\frac{1}{p}}, \quad (3.5-2)$$

in which, the Minkowski distance is metric for $p \geq 1$, and is equal to the Euclidean distance when $p = 2$, and the Manhattan distance when $p = 1$.

3.5.2. Support Vector Machine

The SVM is a supervised learning model that analyzes data for classification and regression purposes. SVMs are based on statistical learning frameworks, which are one of the most robust prediction methods. Basically, SVMs construct a hyperplane or set of hyperplanes in a feature space in which the training dataset can be classified into one or two categories. To explain this, assume the training dataset $T = \{(x^{(1)}, y_1^{(1)}), (x^{(2)}, y_1^{(2)}), \dots, (x^{(N)}, y_1^{(N)})\}$, where $x^{(n)}, n \in [1, N]$ indicates the sample points and $y_1^{(n)} \in [-1, +1]$ demonstrates the binary classification labels assigned to each sample. The objective of the binary classification is to find a separating hyperplane in the feature space in order to separate the sample points with different classes. Thus, the main issue in the SVM algorithm is to define a hyperplane in such a way that, on one side, the misclassification errors should be minimized. On the other side, the gap between sample points belonging to two different classes should be maximized. This gap is called margin and is defined as the distance between the separating hyperplane (decision boundary). Correspondingly, the sample points that are closest to this hyperplane are the so-called support vectors. These details are illustrated in Fig. (3.5.3).

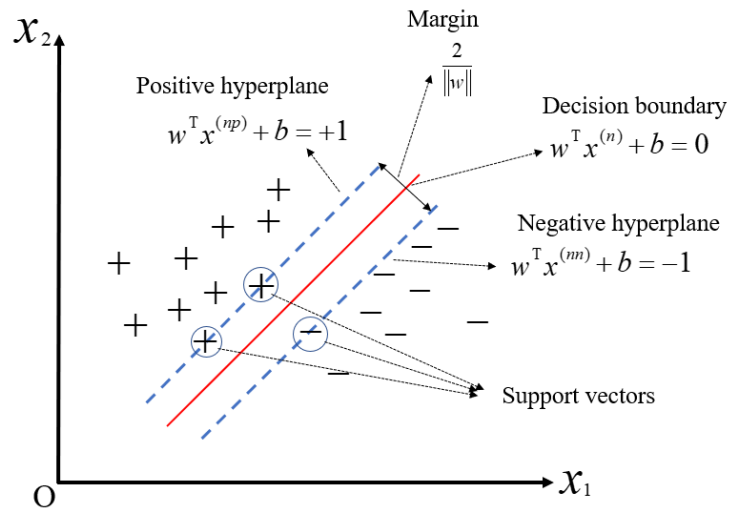


Fig. 3.5.3. Support vectors and margin. Own sketch extracted from [85, 86].

To find the maximum margin, let us formulate the separating hyperplane in the feature space as the following linear function:

$$w^T x^{(n)} + b = 0, \quad (3.5-3)$$

where $w = (w_1, w_2, \dots, w_M)$ is the normal vector, which defines the direction of the hyperplane, b is the bias, which defines the distance between the hyperplane and the origin, and $w^T x^{(n)}$ is the inner product defined as $\langle w, x^{(n)} \rangle$. In order to classify the sample points correctly, the hyperplane should satisfy the following conditions:

$$\begin{cases} w^T x^{(np)} + b \geq +1, & y_l^{np} = +1 \\ w^T x^{(nm)} + b \leq -1 & y_l^{nm} = -1 \end{cases}, \quad (3.5-4)$$

where $x^{(np)}$ and $x^{(nm)}$ indicate those sample points labeled as positive and negative classes, respectively. In addition, the distance from any sample points ($x^{(n)}$) in the feature space to the hyperplane is given by

$$r = \frac{|w^T x^{(n)} + b|}{\|w\|}, \quad (3.5-5)$$

where $\|w\| = \sqrt{\sum_{j=1}^M w_j^2}$ is the length of the vector w . Regarding Eq. (3.4-4), the separating hyperplanes (positive and negative), including support vectors, correspond to $w^T x^{(np)} + b = +1$ and $w^T x^{(nm)} + b = -1$, respectively. Hence, the total distance from two support vectors (positive and negative) to the hyperplane can be obtained by subtracting the support vector formulas as follows:

$$\frac{w^T(x^{(np)} - x^{(nm)})}{\|w\|} = \frac{2}{\|w\|}, \quad (3.5-6)$$

in which $\frac{2}{\|w\|}$ is the so-called margin that should be maximized. The margin can

be optimized by maximizing $\|w\|^{-1}$ or equivalently by minimizing $\|w\|^2$. As a result, Eq. (3.5-4) can be written as

$$\min_{w,b} \frac{1}{2} \|w\|^2, \quad y_l^{(n)}(w^T x^{(n)} + b) \geq 1, \text{ and } n = 1, 2, \dots, N. \quad (3.5-7)$$

This is the primal form of SVM, and the reciprocal term $\frac{1}{2} \|w\|^2$ can be solved by quadratic programming [85,141]. However, Eq. (3.5-7) is appropriate for those scenarios in that the datasets are linearly separable. Vapnik [141]

introduced a slack variable ζ to achieve a soft-margin classification to expand this concept to nonlinearly separable data. Subsequently, Eq. (3.5-4) can be rewritten by adding the positive-value slack variable to the linear constraints as follows:

$$\begin{cases} w^T x^{(n)} + b \geq +1, & y_i^n = 1 - \zeta^{(n)} \\ w^T x^{(n)} + b < -1 & y_i^n = 1 + \zeta^{(n)}. \end{cases} \quad (3.5-8)$$

Correspondingly, the new margin is obtained as $\frac{1}{2} \|w\|^2 + C \left(\sum_{i=1}^N \xi^{(i)} \right)$, where the

variable parameter C controls the width of the margin and tunes the bias-variance trade-off. Another interesting property of the SVM algorithm is its ability to be kernelized, which ables it to solve nonlinear classification problems. Generally speaking, the kernel method projects the linearly inseparable datasets distributed in the feature space onto a higher dimensional space via a mapping function $\phi(\bullet)$ in such a way that the datasets become linearly separable. To explain this mapping feature and kernel SVM, we need to go through details about the dual problem, solving quadratic programming, and the kernel trick, which is beyond the scope of this thesis. However, interested readers are referred to chapter 6 of reference [85]. As summarized in [86], the term kernel can be explained as a similarity function between a pair of samples. Practically, this similarity can be obtained by inner product among sample points defined by $\langle x^{(i)}, x^{(j)} \rangle = x^{(i)T} x^{(j)}$, where $i, j \in [1, N]$. In this regard, the kernel function κ is the inner product of the mapped feature vectors of $x^{(i)}$ and $x^{(j)}$ given by

$$\kappa(x^{(i)}, x^{(j)}) = \langle \phi(x^{(i)}), \phi(x^{(j)}) \rangle. \quad (3.5-9)$$

In other words, instead of the inner product of $x^{(i)}$ and $x^{(j)}$ in the feature space, the kernel function κ calculates the inner function in a higher-dimensional space introduced by the mapping function $\phi(\bullet)$. The choice of the kernel function should be searched in order to map the samples to a proper feature space. Some of these kernel functions are the Linear, Polynomial, Laplacian, Sigmoid, and Gaussian kernels. For instance, two of these kernel functions which are used in this thesis are the Gaussian kernel or the Radial Basis Function Kernel (RBF kernel) and the Sigmoid kernel. The Gaussian kernel is given by

$$\kappa(x^{(i)}, x^{(j)}) = \exp\left(-\gamma \|x^{(i)} - x^{(j)}\|\right), \quad \gamma = \frac{1}{2\sigma^2} \quad (3.5-10)$$

where γ is a free parameter that should be searched to optimize the performance of the kernel. The Sigmoid kernel is given by

$$\kappa(x^{(i)}, x^{(j)}) = \tanh(\beta x^{(i)\top} x^{(j)} + \theta), \quad (3.5-11)$$

where \tanh is the hyperbolic tangent function, $\beta > 0$, and $\theta < 0$. In conclusion, a kernel SVM is able to separate data points by a nonlinear decision boundary.

3.5.3. Convolutional Neural Network

In 1988, LeCun built the first CNN called LeNet [142]. The CNN algorithms are one of the most popular neural network architectures in deep learning. Deep learning is one of the most well-known representations of Machine learning nowadays. Deep learning applications have achieved notable accuracy and popularity in various fields, especially in the computer vision field. To explain deep learning and CNN, we need to have enough knowledge about Artificial Neural Networks (ANNs). However, the mathematics and theory behind the ANN are quite advanced, and it is beyond the purpose of this thesis. Here, we limit ourselves to introducing the general idea of deep learning, ANN, and CNN. Nevertheless, the interested readers are referred to reference [143].

In 1958, Rosenblatt introduced a model called perceptron, which can be considered as a primary neural network algorithm. As explained in [87], the principle of ANNs is to learn from distributed data in such a way that the generated data results from a nonlinear combination of a set of hidden factors (neurons) that can predict a new unseen set of data. The neural network architectures consist of an input layer, a hidden layer (a result of applying a nonlinear transformation to the input data), and an output layer. Besides, the weights of each connection including in the network and a bias are two parameters of an ANN model. A simple sketch of a neural network with just one hidden layer is shown in Fig. (3.5.4). In deep neural networks, there is more than one hidden layer. The neural network architecture illustrated in Fig. (3.5.4) consists of the input vector of size 5, the hidden layer of size 6, and the output vector of size 3.

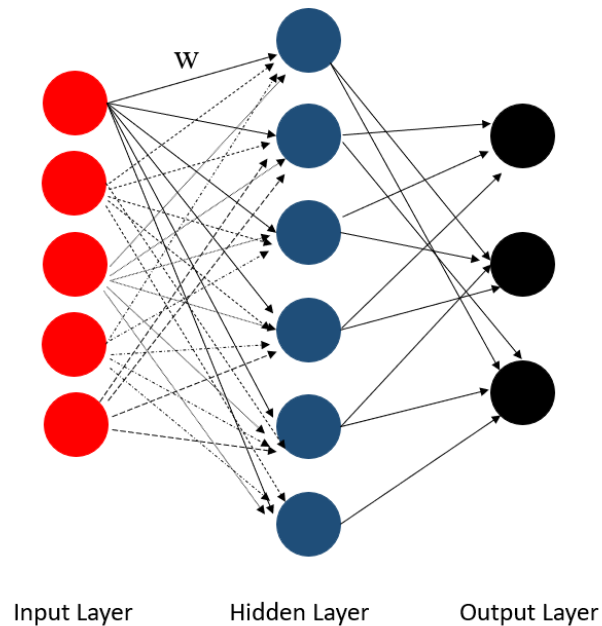


Fig. 3.5.4. A neural network structure. Neurons are indicated by circles. Neurons are connected by the parameter weight w . Arrows show the connection among neurons in different layers. Own sketch extracted from [87].

The learning process of an ANN can be summarized as follows:

- To select the structure of the network, including neurons and layers.
- To define the nonlinear transformation applying to each connection, in which transformation controls the activeness of each neuron in the network.
- To select a proper loss function applicable for supervised learning to optimize the output layer associated with the class label of each data point,

resulting in learning the parameters of the neural network, for instance, the value of each connection weight w . The parameters should be optimized using optimization methods and a method called backpropagation.

One of the promising deep learning algorithms which gained popularity in the computer vision domain is CNN due to its excellent performance on image classification tasks. As explained in [86], CNNs build many layers of feature detectors from the spatial arrangement of pixels in an input image. Despite different variants of CNNs, here we just summarize the general idea of CNN.

Using CNNs, the extracted feature vectors from an image are fully connected to the hidden layer resulting in connecting the input layer to a feature map. This approach can be described as overlapping windows that slide over the pixels of an input image to create feature maps. This process of extracting feature maps in this way is called convolution. In addition, the stride lengths of the window and the size of windows are the pre-defined hyperparameters of a CNN model, which can cause different feature maps. A structure of a CNN model is illustrated in Fig. (3.5.5).

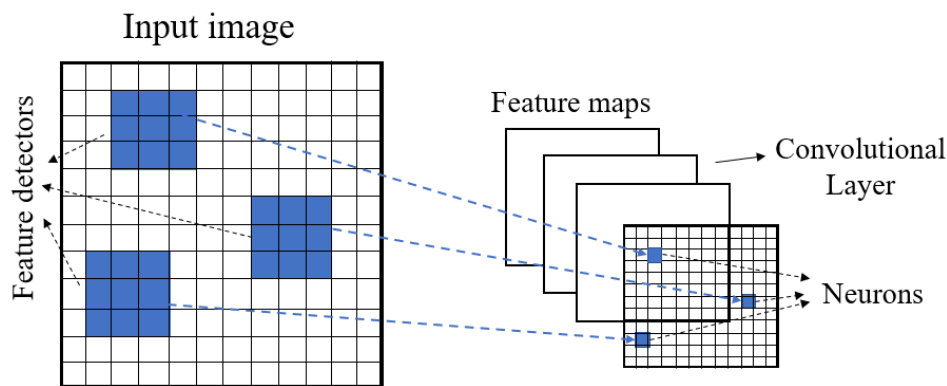


Fig. 3.5.5. A CNN architecture. Own sketch extracted from [85, 86, 87].

The convolutional layer connects the input pixels to neurons (units) in the feature map. Feature detectors or filters (kernels) detect features like edges or convex shapes, and a feature map is a convolution of the input image with a feature detector which is an element-wise multiplication of matrices considering pixelated input image as a matrix. Since the feature detectors are replicates, the model that maps the features to the neurons shares the same weight in the next layer. As a consequence, the number of parameters that need to be learned is dramatically reduced.

Recognizing objects of different sizes and different positions in an image is one of the interesting abilities of CNNs. In general, CNNs are broadly comprised of three types of layers: convolutional layer, pooling layer, and fully connected layer. In CNN schemes, a convolutional layer is usually followed by a pooling layer. In the pooling process, the number of feature detectors is reduced by taking the average or maximum value of a patch of neighboring features. This process is shown in Fig. (3.5.6).

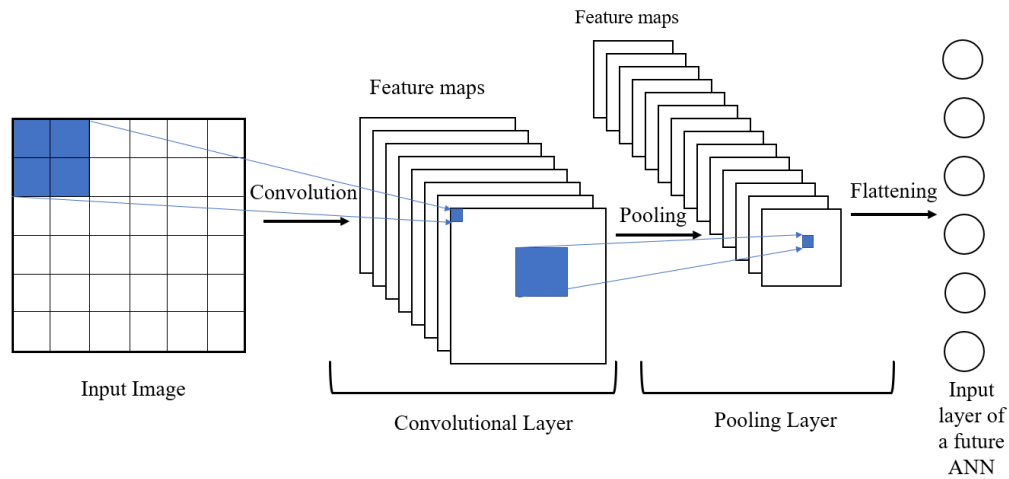


Fig. 3.5.6. The illustration of obtaining the input layer for an ANN structure using a convolutional layer followed by a pooling layer. Own sketch extracted from [85,86]

In order to build a model, the first step is to select a model structure which can be either a sequential model or a functional model. The basic model can be enriched by adding different layers such as the Drop out layer, the Dense layer, and the activation layer. Adding a set of layers should be based on the requirement of the model. The next step is the compilation of the model, defined as the configuration of the learning process. During the learning process, there are three main parameters as Optimizer, Loss function, and performance metrics. The optimizer specifies the actual optimization algorithm to train the model and minimize the error or loss. The loss function specifies the objective of minimizing loss to guarantee the best performance of the model over multiple epochs or iterations. In particular, a cross-entropy loss is used for classification purposes. The performance metric measures the learning process, for instance, accuracy for classification models.

4. Beam modulation with a twisted nematic liquid crystal display

Liquid crystal display devices are a kind of spatial light modulator (SLM). SLMs are able to relate electronic data to spatially modulated light beams. In particular, the twisted nematic liquid crystal (TNLC) spatial light modulators are kind of relatively low-cost electro-optics devices widely used in many branches of optical information processing such as digital holography [144,145], spatially-variant polarized beams [54], coherent diffraction imaging [146], generating vector beams [147-149], pattern recognition and optical correlators [150], Fresnel lenses [151,152], and optical cryptosystem [59,153,154].

Regarding specific situations, including the state of polarization, the wavelength of input beams, and applied voltages, three different modulations are mainly interesting: amplitude-only, phase-only, and complex phase-amplitude. The twisted angle and the birefringence of the TNLC are the two main parameters that control the modulation. There are several proposed methods and configurations to find these parameters to obtain the Jones matrix of a TNLC [155-167]. We briefly explain the optical property of a TNLC in the following subsection. To summarize the effects of a TNLC in the optical system, we introduce the following equation:

$$E_t = A \exp(-j\varphi) \quad (4.1)$$

where A stands for the transmitted amplitude and φ represents the imposed phase to the transmitted beam. The phase and amplitude of a transmitted beam are directly related to the optical setup configuration, the state of input polarization, the wavelength of the input beam, and the applied voltages. Characterizing a SLM aims to obtain Eq. (4.1). In this work, we used a translucent Holoeye HEO 0017 TNLC-SLM with a resolution of 1024×768 pixels and a pixel pitch (p) of $32 \mu\text{m}$. The mentioned SLM can provide the maximum phase shift of about 1.75π for a laser beam with a 514 nm wavelength.

4.1. Twisted nematic liquid crystal display

A twisted nematic liquid crystal display is constructed by sandwiching a nematic liquid crystal between two transparent glass plates. Different voltages impose an external electric field through the medium using electrodes connected to each glass plate. Nematic molecules inside the medium have a helical structure with an optical axis parallel to their elongated direction. In this

regard, TNLCs are a sort of birefringent medium with ordinary and extraordinary refractive indices (n_o, n_e). The birefringence of the medium is altered by applying different voltages resulting in tilting nematic molecules in the direction of the applied electric field. Hence, TNLCs can electrically be controlled to be used as optical wave retarders, modulators, and switches. In the absence of the applied electric field, nematic molecules are oriented with respect to each other in the plane parallel to the surface of the glasses. In the particular case that the input beam is linearly polarized parallel to the direction of the liquid crystal director (practically, it is unknown to users), the beam keeps its state of polarization traveling through TNLC but rotating as much as its twisted angle α , which is usually equal to 90° . In this condition, the TNLC acts as a polarization rotator. If the direction of polarization of the input beam is oriented concerning the LC director, the beam experiences phase retardation as $2\pi(n_e - n_o)d/\lambda$, where d is the thickness of LC display. In the presence of the applied electric field, the nematic molecules tilt to be aligned with the direction of the applied field. The amount of this tilt angle (θ) depends on the applied voltages causing different birefringence. So, LC becomes a variable retarder with retardation $\Gamma = 2\pi[n(\theta) - n_o]d/\lambda$. The retardation varies monotonically from 0 (when the molecules are not tilted, $\theta = 0$) to $\Gamma_{\max} = 2\pi[n_e - n_o]d/\lambda$ (when molecules are tilted 90° , $\theta = 90^\circ$). In summary, based on the physical configuration of the experimental setup, an input beam traveling through nematic liquid crystal cells might face only-twisted, twisted and tilted, or only-tilted nematic molecules. The twisted angle, the birefringence, and the director of LC should be obtained to introduce the Jones matrix of TNLC display [124].

4.2. Characterizing TNLC displays

Since SLMs change the properties of light, such as amplitude, phase, and polarization, it is necessary to find the proper operating conditions in order to control the response of the SLM. Martín-Badosa et al. proposed a method to characterize LCD based on the fringe analysis obtained by a Mach-Zehnder interferometer configuration without the necessity of finding the physical properties of LCD [168]. Nevertheless, their approach is based on counting the displacement of the fringes and is time-consuming. With the same optical setup and a different mathematical description, Wang et al. proposed a faster and more convenient way to obtain phase modulation [169]. They indicated that analyzing the phase values of those frequencies where ± 1 diffraction orders occurred is sufficient to obtain the imposed modulated phase. Since the interferometric patterns were obtained by propagating beam at a distance between LCD and

CCD camera, their mathematical approach was based on Fresnel diffraction considering the transfer function.

Since the digital holography approach used in this work is based on the double-pixel Arrizón's approach, the Mach-Zehnder interferometer should be modified in order to eliminate the off-axis diffraction orders caused by the codification algorithm (as explained in 3.3). Therefore, the optical setup used in this work is modified by adding a 4f-spatial filtering system. Accordingly, the mathematical analysis based on this experimental setup is presented. Apart from the phase calibration, the characterization of the amplitude with the same setup is obtained.

Different gray values displayed on a SLM correspond to the various applied voltages, resulting in different degrees of birefringence. Accordingly, the phase and intensity of the input beam are modified by passing through the SLM, as introduced in Eq. (4.1). This subsection aims to obtain Eq. (4.1) for each gray value ranging from 0 to 255.

The calibration setup is a Mach-Zehnder interferometer plus a 4-f spatial filtering system, as shown in Fig. (4.1). A collimated and linearly polarized green laser beam ($\lambda=514\text{nm}$) is divided into two arms of the interferometer by the first beam splitter (BS1). On the one hand, the right arm of the interferometer, which the object beam passes through, includes a half-wave plate (HWP1), a quarter-wave plate (QWP1), and the transmissive TNLCD. On the other hand, the left arm of the interferometer, which the reference beam passes through, includes a half-wave plate (HWP2). Subsequently, the interference occurs when the two beams reach the second beam splitter (BS2). Then the interference pattern passing through the second linear polarizer (LP2) reaches the sensor plane of the CCD camera by means of the 4-f spatial filtering system.

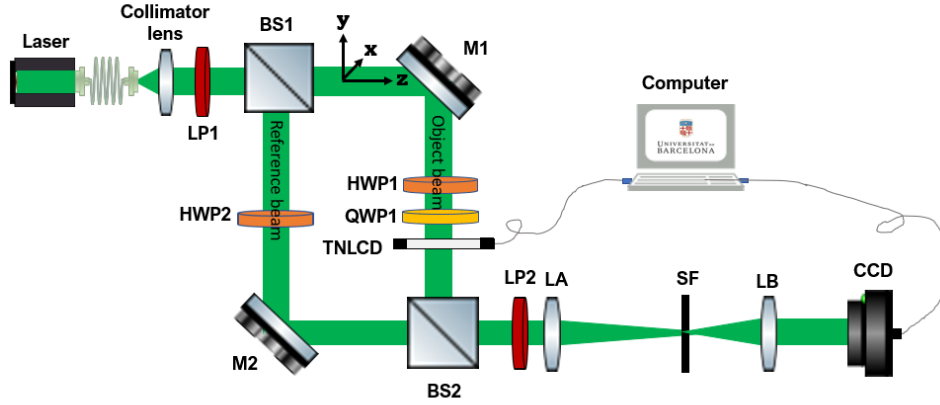


Fig. 4.1. The experimental setup. LP, BS, HWP, QWP, M, SF, and CCD stand for the linear polarizer, beam splitter, half-wave plate, quarter-wave plate, mirror, spatial filter, and charged-coupled device, respectively. Figure from [139] under the CC Attribution 3.0 Unported License.

Regarding the experimental setup, LCD is placed at the back focal plane of lens A (LA), and the CCD camera is located at the front focal plane of lens B (LB). Besides, the diffraction orders (except zero-order) caused by the pixelated structure of the LCD and the digital holography approach are eliminated using a spatial filter placed at the common focal plane of LA and LB. Mirror M2 is properly tilted in such a way that the fringes are aligned in the y-direction (vertical direction), as shown in Fig. (4.1a).

The fringe pattern recorded by the CCD can be expressed mathematically in the form:

$$g(x, y) = a(x, y) + b(x, y) \cos[2\pi f_0 x + \phi(x, y) + \varphi_m], \quad (4.2)$$

where $\phi(x, y)$ and φ_m are the phase of the object and the modulated phase imposed by SLM, respectively. Furthermore, $a(x, y)$ represents possible nonuniform background, $b(x, y)$ represents the local contrast of the pattern, and f_0 is the spatial-carrier frequency. As explained in [170], the fringe pattern can be rewritten in the following form:

$$g(x, y) = a(x, y) + c(x, y) \exp(j2\pi f_0 x) + c^*(x, y) \exp(-j2\pi f_0 x), \quad (4.3a)$$

with

$$c(x, y) = (1/2)b(x, y)\exp(j\phi(x, y))\exp(j\phi_m). \quad (4.3b)$$

The Fourier transform of Eq. (4.3) gives

$$G(f_x, f_y) = A(f_x, f_y) + C(f_x - f_0, f_y) + C^*(f_x + f_0, f_y), \quad (4.4)$$

where the capital letters denote the Fourier spectra, f_x and f_y are the spatial frequencies in the x and y-direction, respectively. In fact, $A(f_x, f_y)$ is the zero-order of the interference, C and C^* are ± 1 interference orders, respectively. Since the spatial variations of $a(x, y)$, $b(x, y)$, and $\phi(x, y)$ are slow compared with spatial frequency f_0 , the Fourier spectra are separated by carrier frequency f_0 , as shown in Fig. (4.2b).

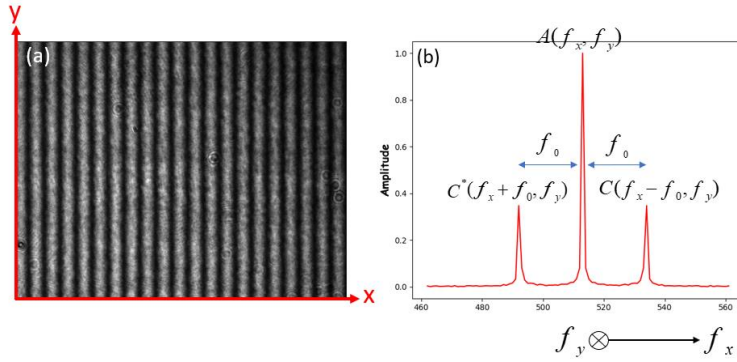


Fig. 4.2. (a) The interferometric pattern. (b) The corresponding frequency Fourier spectra. Figure from [139] under the CC Attribution 3.0 Unported License.

Note that here we are not interested in finding the phase of the object. We intend to find the phase shift resulting from loading the different gray values on the LCD. Once the configuration of the experiment, for instance, wavelength and the optical path difference between the reference and object beam, remains constant, the position of the peaks in the frequency domain remains unchanged. Thereby, the modulated phase can be obtained by analyzing either C or C^* . Complex value C can be rewritten as follows:

$$\begin{aligned} C(f_x, f_y) &= \text{FT} \left\{ (1/2)b(x, y)\exp[j(\phi(x, y) + 2\pi f_0 x)]\exp(j\phi_m) \right\} \\ C(f_x, f_y) &= |C|\exp(j\Phi)\exp(j\phi_m) \end{aligned} \quad (4.5)$$

where $\text{FT}\{\dots\}$ denotes the Fourier transform, and $|C|$ and Φ are the amplitude and phase of C in the frequency domain, respectively. Therefore, according to

the fact that the experimental parameters remain constant during the whole process of the measurement, the phase of $C(f_x, f_y)$ varies only with φ_m , that is, the modulated phase imposed by SLM according to gray values loading on LCD.

In conclusion, if we split the object into two parts which are separated by a reference gray value (zero) and variable gray values ranging from 0 to 255, the subtracting of the phase of $C(f_x, f_y)$ gives the phase shift as follows:

$$C(f_x, f_y)_{rg} = |C| \exp(j\Phi) \exp(j\varphi_{rg}), \quad (4.6a)$$

$$C(f_x, f_y)_{vg} = |C| \exp(j\Phi) \exp(j\varphi_{vg}), \quad (4.6b)$$

$$\Delta\varphi = \arg[C(f_x, f_y)_{vg}] - \arg[C(f_x, f_y)_{rg}] + \varphi_0, \quad (4.6c)$$

where subscripts rg , vg , and $\Delta\varphi$ indicate the reference and variable gray values, and the phase shift, respectively. Besides, φ_0 is chosen in which $\Delta\varphi = 0$ when the image loading on LCD has zero value. In the following, the experimental process is expressed in two main stages: phase modulation and amplitude modulation, step by step.

4.2.1. Phase modulation

Firstly, we synthesize gray-level images in such a way that the half-upper part of images varies from 0 to 255 while the half-lower part remains zero as a reference. Applying these images on SLM cause different phase shift between the upper and lower part of the interference pattern resulting in a displacement of fringes. The amount of this phase shift can be obtained by Eq. (4.6c). The first row of Fig. (4.3) shows the provided gray-level images loaded on the LCD, whereas the second row indicates the corresponding interference patterns which were recorded by the CCD camera.

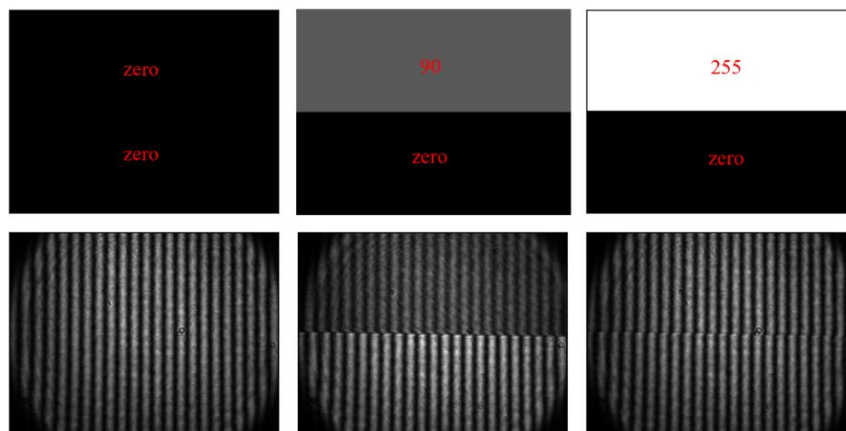


Fig. 4.3. Three examples of gray-level images loaded on the TNLC display and corresponding interference patterns recorded by the CCD camera are shown in the first and the second row, respectively. Figure from [139] under the CC Attribution 3.0 Unported License.

We used the LabVIEW (program language) in order to load 256 gray-level images on the LCD, record the interference patterns by CCD camera and save them automatically. Note that it is necessary to apply a delay between loading images and capturing them regarding the molecules of the TNLC being aligned with the applied voltages (around $100 \mu\text{s}$) and relaxing back to their original state (around 20 ms). The next step is analyzing the interference patterns to obtain the phase modulation imposed by each gray value. Accordingly, two equal parts of the upper and lower part of each interference pattern are chosen, as shown in Fig. (4.4b), separated by red rectangles. Then, we calculate the 2D fast Fourier transform of the selected upper and lower part to find the frequency $C(f_x, f_y)$ that first order of the interference occurs, as shown in Fig. (4.4c). This point in the frequency domain should be the same not only for the upper and lower part but also for all 256 interference patterns. Subsequently, the phase shift between variable gray values (the upper part) and zero value (the lower part) is calculated separately for each gray-level image by means of Eq. (4.6).

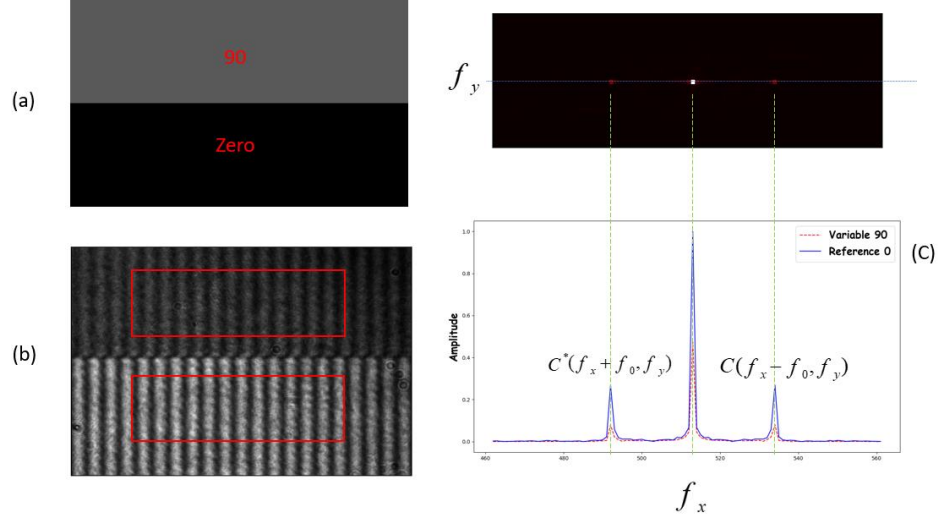


Fig. 4.4. (a) a gray-level image loaded on LCD, which is separated with two different gray values. (b) Fringe displacement in the x-direction. The red selected rectangles are used for calculating the 2D Fourier transform. (c) The corresponding modulus of the Fourier transform. Figure from [139] under the CC Attribution 3.0 Unported License.

Therefore, the possible imposed phase versus each gray value is adjustable from zero to the maximum available one. In this case, the maximum achievable phase imposed by SLM is around 1.75π . However, this value depends on the TNLC physical properties, the optical wavelength, and the polarization state of the incoming light. Thus, finding the proper modulation curve is a practical task. In regard to the experimental setup (Fig. (4.1)), we set the axis of LP1 parallel to the axis x while the axis of LP2 was parallel to the axis y. The role of HWP2 is to control the contrast intensity of the interference pattern. We applied the HWP1 in order to remove the necessity of rotating the axis of LP1. Hence, the desired modulation has been obtained by some practical attempts by rotating the fast axes of HWP1 and QWP1 with respect to each other. In this regard, the fast axis of HWP2, HWP1, and QWP1 were rotated -20, -63, and 45 degrees with respect to the axis x, respectively. The obtained phase curve versus gray values is shown in Fig. (4.5a).

4.2.2. Amplitude modulation

With the same setup without changing the direction axes of linear polarizers or retarders, the amplitude curve was obtained as follows: Firstly, we blocked the left arm of the Mach-Zehnder interferometer. Then, we provided 256 gray-level images in which the entire images had the same value ranging from 0 to 255, corresponding with each gray value. Each gray-level image was loaded on the

SLM, and the images were subsequently recorded by the CCD camera. By calculating the square root of the mean value of the recorded images and normalizing them to the maximum obtained amplitude, the modulated amplitude versus each gray value was obtained. Also, this process can be done by using an intensity detector. Note that all the attribution of the camera, such as Brightness, Shutter, and Contrast, should be constant during the measurement, and the other attributions, such as Gamma and Gain, must be disabled. The obtained amplitude curve is shown in Fig. (4.5b).

Finally, Eq. (4.1) was obtained for each gray value by combining the amplitude and phase responses of the SLM in consequence of the present configuration. This process is called the characterization or calibration of SLM. The polar plot of the obtained complex amplitude-phase modulation is shown in Fig. (4.5c).

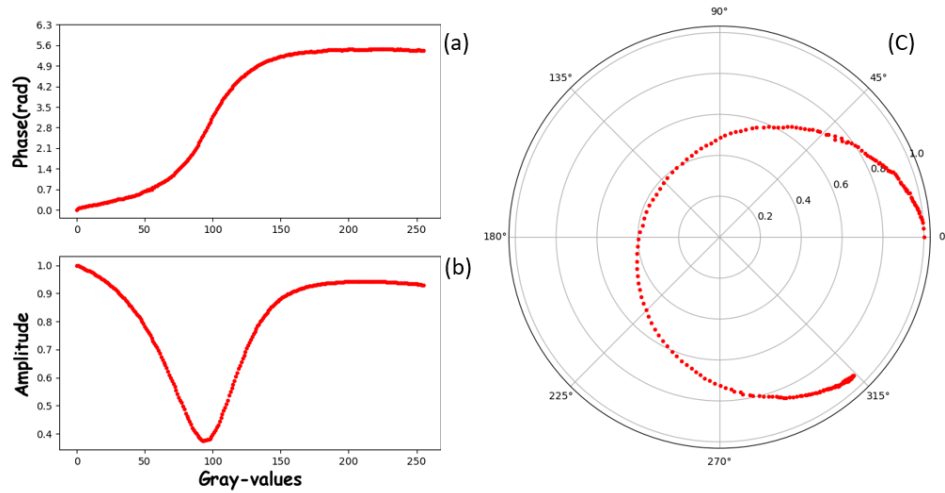


Fig. 4.5. (a) The phase modulation. (b) The amplitude modulation. (c) The polar plot shows the complex amplitude-phase modulation curve. Figure from [139] under the CC Attribution 3.0 Unported License.

4.3. Fast generating DPHs using KNN classifier

As explained in subsection 3.3, the DPH approach proposed by Arrizón is able to produce an on-axis CGH into a low-resolution SLM for encoding arbitrary complex modulation. Since the modulation points on the modulation curve (shown in Fig. (4.5c)) are limited, we applied Eq. (3.3-4) to expand the accessible modulations beyond the restricted SLM responses according to DPH's approach. All the possible complex values which can be obtained by means of Eq. (3.3-4) and the phase-mostly modulation curve are shown with the green points in Fig. (4.6). Among all possible complex values, only those that fall inside the blue circle with radius $A_0 = 0.29$ can encode a complex function with the amplitude ranging from 0 to A_0 and the phase ranging from 0 to 2π .

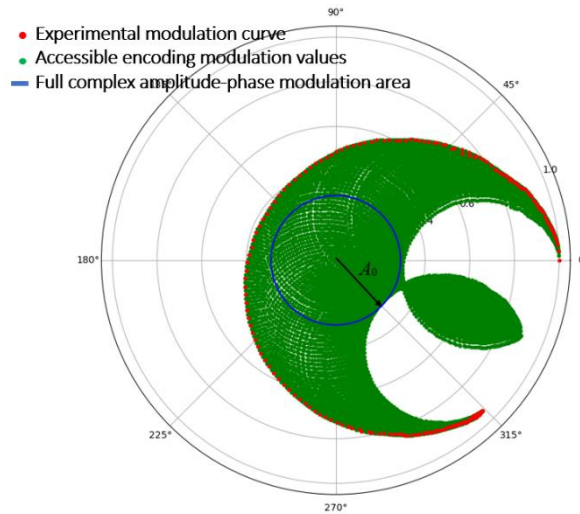


Fig. 4.6. The Red and green points show the experimental modulation curve and all possible complex values using the DPH approach, respectively. The green points inside the blue circle with the radius $A_0=0.29$ are those accessible complex values to encode a complex function.

Figure from [139] under the CC Attribution 3.0 Unported License.

The encoding procedure can be summarized as follows: Let $q_{nm} = |q_{nm}| \exp(j\tau_{nm})$ be a complex modulation value to be encoded in the holographic cell $[n,m]$, where $|q_{nm}|$ and τ_{nm} stand for the amplitude and the phase of q_{nm} . Let a be a point that belongs to the set of accessible values

obtained using the DPH approach (for instance, green points in Fig. (4.6)). Among all possible points ($q_{nm}^a = |q_{nm}^a| \exp(j\tau_{nm}^a)$), we select the one that fulfills that the Euclidean distance between q_{nm} and q_{nm}^a is minimum (see Eq. (3.3-12)). This calculation requires an extensive search of the minimum Euclidean distance between the desired complex values and the accessible ones. In other words, This involves the use of several nested loops to search the minimum Euclidean distance for each cell to find the nearest available complex value q_{nm}^a provided by the experimental modulation curve (see Fig. (4.6)) to the desired complex value (q_{nm}). This conventional calculation is time-consuming. For instance, to generate a CGH with 768×1024 pixels, and since four pixels at the SLM plane provide one holographic cell, there are $(768 \times 1024)/4 = 196,608$ holographic cells that should be mapped among all accessible complex values. Thereby, we present a fast method using the KNN machine learning algorithm in order to classify all accessible modulation values and predict the nearest complex value to the desired one.

We used the Scikit-learn Python library to implement the KNN algorithm. Regarding the KNeighborsClassifier module, three parameters should be determined, such as k, weight, and metrics, as explained in section 3.5.1. Besides, to train the machine, a matrix with a-samples and b-features should be defined (see section 3.5).

In our case, the number of samples is the number of all accessible complex points, while the features are chosen based on the real and imaginary values of each accessible complex point (green points fall inside the blue circle in Fig. (4.6)). Regarding the modulation curve shown in Fig. (4.6), the total number of classified samples is $a=3540$ with two features ($b=2$). The machine is trained based on data that comes from the experimental modulation curve (as shown in Fig (4.6)), whereas the nearest accessible complex values to the desired ones will be predicted by the machine for each holographic cell. The optimum results were obtained by choosing $k=1$, weights= distance, and metrics= Euclidean distance for each CGH.

On the one hand, we provided a look-up matrix from all accessible complex values (q_{nm}^a), as shown in Fig (4.7a). On the other hand, we trained the machine, as shown in Fig (4.7b).

Index	q^a	M_g^1	M_g^2	Label	Real value of q^a	Imaginary value of q^a
0	3.39+0.34j	5	102	0	3.39	0.34
1	3.4+0.32j	5	103	1	3.4	0.32
⋮	⋮	⋮	⋮	⋮	⋮	⋮
⋮	⋮	⋮	⋮	⋮	⋮	⋮
⋮	⋮	⋮	⋮	⋮	⋮	⋮
3539	-1.6+0.72j	93	255	3539	-1.6	0.72

Fig. 4.7. (a) The provided look-up matrix with 3540 rows and three columns. (b) The configuration of the labeled training dataset with 3540 samples and two features. Figure from [139] under the CC Attribution 3.0 Unported License.

So, the machine predicted the class label of the nearest accessible complex value to the desired one. Then, the pair of gray-level (M_g^1, M_g^2) corresponding with the predicted label has been distributed to the related holographic cell, as shown in either Fig (3.3.4) or Fig (3.3.5).

In order to evaluate the advantage of using the KNN classifier over the conventional calculation, we compared the processing time to build a CGH with different resolutions. We tested the method by calculating the DPH associated with this function: $B(r, \theta) = \sqrt{r} J_1(2\pi \rho_0 r) \exp(j\theta)$, where r and θ are polar coordinates, J_1 is the first order of Bessel function, and ρ_0 is the radial spatial frequency of the beam. Numerical calculations have been carried out using Python 3.7.5, a laptop with CPU i7-4510U (2 GHz) and 6 GB RAM. Besides, the processing time was obtained by the timeit module. The results are shown in Table. (4.1), which are averages of 10 runs.

Table. 4.1. Processing time (in seconds)

Resolution	250×250	512×512	768×1024	1152×1920
k-NN Classifier	0.45	1.45	4.67	12.78
Conventional calculation	30.35	126.54	383.13	1095.57

The first row of Fig. (4.8) demonstrates the amplitude and phase distribution of $B(r, \theta)$, whereas the second row shows their nearest values predicted by the KNN classifier. The absolute value of MSE between the actual function and the

predicted one is 0.0003, due to the limited number of accessible modulation points. Note that the MSE was the same for both approaches: mapping by the KNN classifier and conventional calculations. The corresponding CGH and the recorded intensity pattern of the wavefunction are shown in Fig. (4.9).

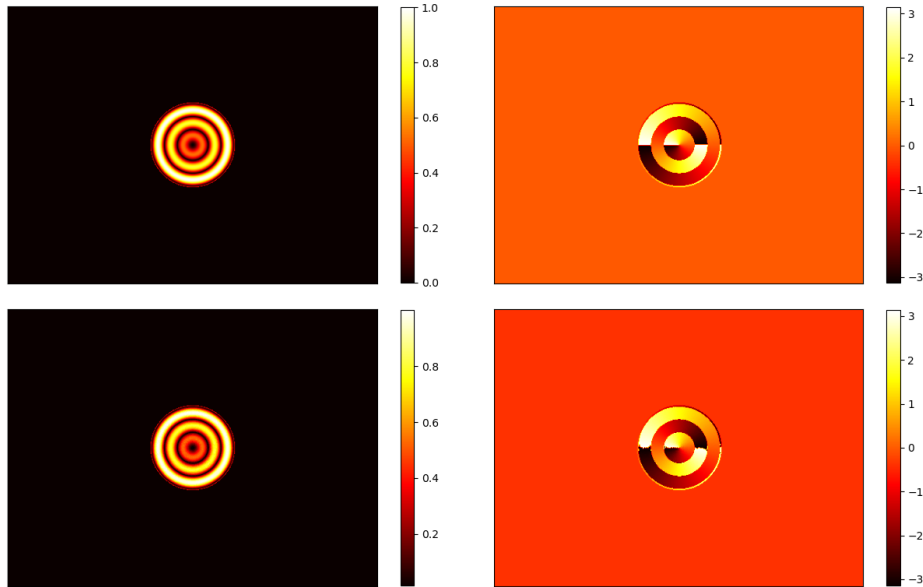


Fig. 4.8. The first row shows the distribution of the amplitude and phase of $B(r, \theta)$, respectively. The second row shows their nearest values predicted by the KNN classifier.

The results demonstrate that the KNN Classifier speeds up the numerical calculation for generating CGHs around 80 times without losing precision. However, since the KNN classifier is a type of nonparametric supervised machine learning algorithm, increasing the number of accessible modulation points causes the curse of dimensionality [86]. In this regard, performing KNN using the RAPIDS cuML library on GPUs not only can solve this problem, but also dramatically accelerates the numerical calculations. As reported in [171], implementing KNN by the RAPID cuML library on GPUs is 600 times faster than performing KNN applying the Scikit-learn library on CPUs. In conclusion, this proposed approach can generate double-pixel computer-generated holograms in real-time.

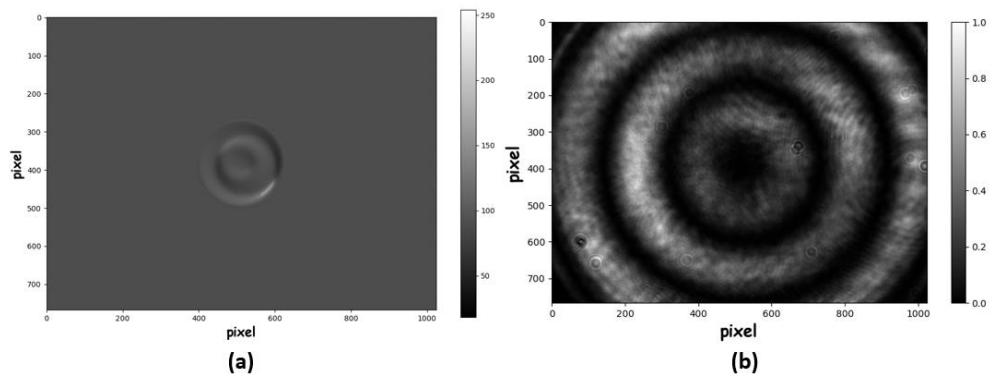


Fig. 4.9. (a) The CGH corresponding with $B(r, \theta)$ and (b) the corresponding intensity pattern recorded by the CCD camera.

5. Encoding character codes in an optical beam

In this section, we introduce the Circular Encoder (CE), in which binary information can be distributed in the radial and azimuthal parts of a circular environment adjusted to an optical beam. Then, the synthesized CE is encoded into holographic cells to be propagated in free space.

Character codes define a relationship between specific characters and sequences of bits. For instance, ASCII (American Standard Code for Information Interchange) is 7-bit, and the Extended ASCII is an 8-bit character code. The number of characters is expanded by other standard encoding designs such as Unicode (16-bit) and UTF-32 (32-bit Unicode Transformation Format). Besides, character codes facilitate the processing, transmission, and display of texts from numerous languages and technical disciplines, including mathematical and musical icons and symbols accompanied by control characters (non-printable characters). This section aims to propose an approach to encode binary information into a laser beam, which might be used in auto-detection applications, free-space optical communication, and optical encryption.

5.1. Configuration of CEs

A CE consists of several annuli (concentric rings) and several parts (angular sectors) defined by r and φ , respectively. The radial direction is divided into several annuli according to the number of characters, while the azimuthal direction is divided into angular sectors according to the number of bits. This design is illustrated in Fig. (5.1).

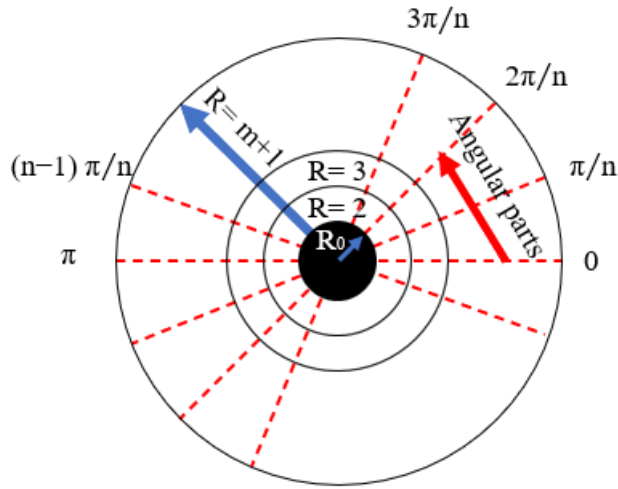


Fig. 5.1. Circular Encoder design. The CE is divided into the $m+1$ annulus in the radial direction ($r_{\max} = R$) and $2n$ angular sectors (φ) to encode m n -bit character codes. R_0 is an arbitrary radius regarding a null region.

As shown in Fig. (5.1), the first region is a null and opaque area with an arbitrary radius (R_0). The encoding area ($R_0 \leq r \leq R$) is divided into m annuli, and each annulus is divided into n angular sectors where n is an integer equal to the number of bits. Each angular sector from $\varphi\pi/n$ to $(\varphi+1)\pi/n$, where $\varphi \in [0, n-1]$, corresponds to the digit position from the most valuable position of digits to the lowest ones, respectively. Binary values, 0 and 1, are encoded into CE as opaque and transparent angular sectors. Besides, CEs are designed radially symmetric.

For instance, consider the list of letters as ['K', 'a', 'v', 'a', 'n'] to be encoded in this way. Letters are transferred to decimal values regarding the ASCII table, then to binary values, and finally, the binary codes are distributed in a CE, as shown in Fig. (5.2).

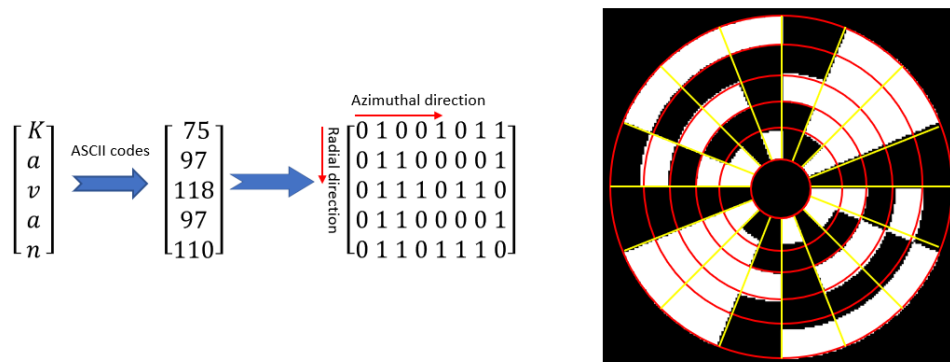


Fig. 5.2. CE corresponds to the list of letters ['K', 'a', 'v', 'a', 'n']. The red concentric rings separate each annulus corresponding with each letter, whereas the yellow lines separate each angular part corresponding with binary values.

5.2. Experiment and results

The message of Fig. (5.2) is encoded into holographic cells according to DPH Arrizón's approach. Then the synthesized laser beam can be propagated in free space. The experimental setup is sketched in Fig. (5.3). A green laser accompanied by a Lens L1 provides a collimated coherent beam. Linear polarizer LP1 and quarter-wave plate QWP accompanied by linear polarizer LP2 are used to characterize TN-LCD, as explained with details in subsection 4.2. The 4f-imaging system images the synthesized laser beam at the sensor plane of the CCD.

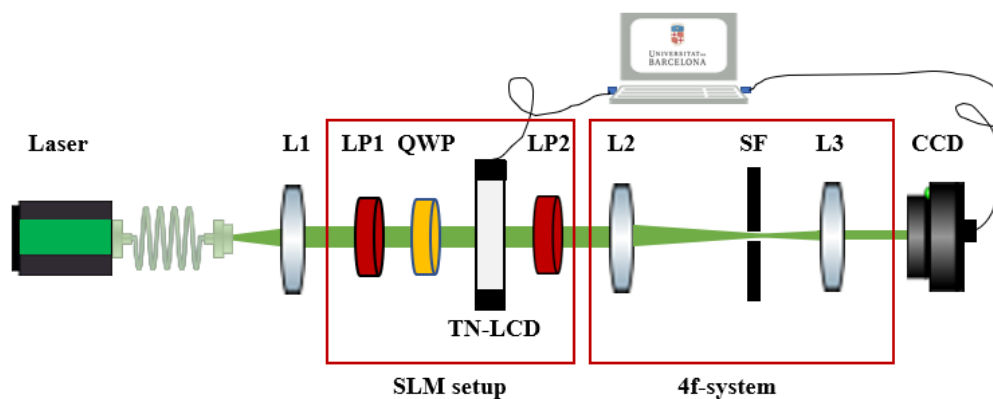


Fig. 5.3. The experimental setup.

A spatial filter is used to eliminate the orders of diffraction caused by the DPH approach and pixelated display except for the zero-order. The magnification of the 4f-system is tuned to adjust the size of the laser beam into the sensor size of the CCD. In order to synthesize the laser beam based on the CE configuration shown in Fig (5.2), we calculated the corresponding CGH with the fast approach introduced in subsection 4.3. Figure (5.4a) demonstrates the corresponding CGH, whereas Fig. (5.4b) indicates the associated intensity pattern recorded by CCD.

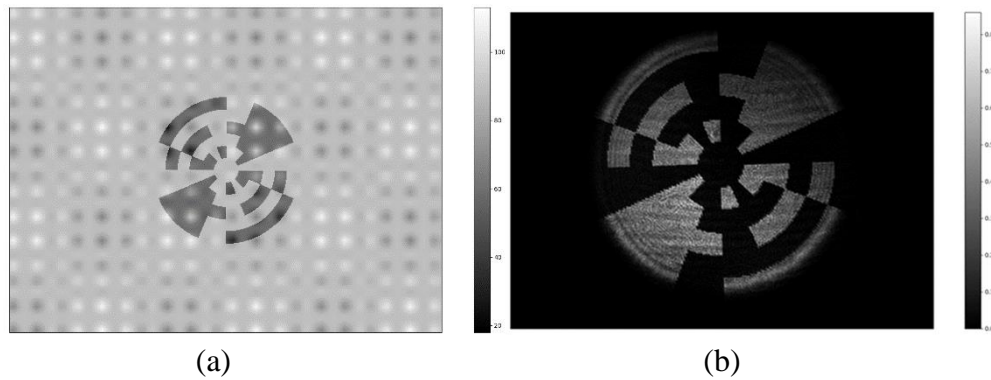


Fig. 5.4. (a) CGH corresponds to CE shown in Fig. (4.2). (b) The corresponding intensity pattern recorded by the CCD camera.

Finally, binary values will be decoded by averaging and binarizing the intensity of all pixels located on each angular part that belongs to each annulus. Accordingly, the encoded character code can be recovered.

In Fig (5.5), we provide another more complex example in order to include 15 8-bit character codes in a laser beam with a radius equal to 5.3 mm, and each annulus is separated by a radial distance equal to 320 μm .

In conclusion, this approach might be used to transfer character codes in free space by encoding character codes into holographic cells. However, there is a limitation regarding the maximum possible number of character codes that can be included in a laser beam. The maximum number of character codes depends on the physical properties of the spatial light modulator, such as pixel pitch and resolution, the radius of the laser beam, and the approach used to generate CGHs.

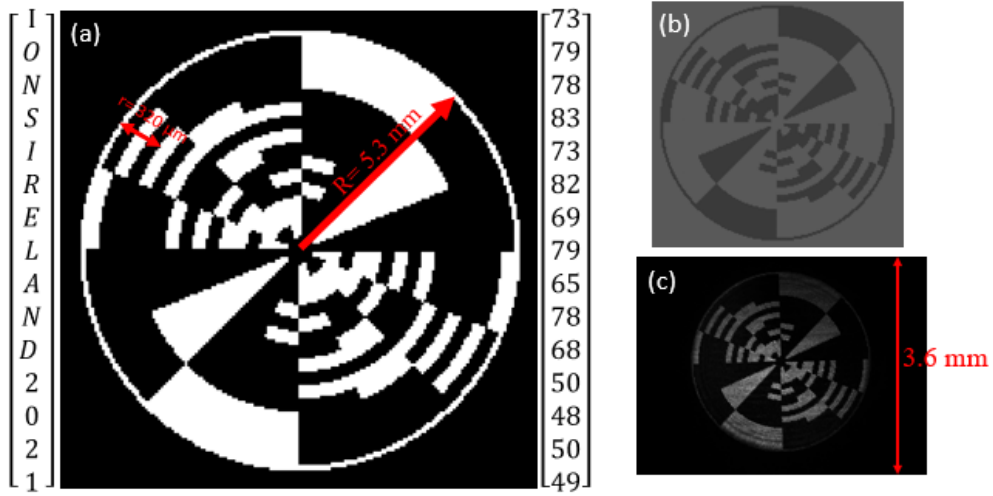


Fig. 5.5. (a) CE encodes the list of letters and numbers ['I', 'O', 'N', 'S', 'I', 'R', 'E', 'L', 'A', 'N', 'D', '2', '0', '2', '1']. (b) The corresponding CGH and (c) the recorded intensity pattern by the CCD camera.

We applied this method to synthesize optical beams at the entrance pupil of a focusing system in order to manipulate the intensity patterns of the focused beam at the focal plane. This approach helped us to obtain a training dataset for pattern classification using deep learning. The method is explained in section 8.

6. Generating highly focused EM fields and recovering their transverse and longitudinal components in the focal area

Highly focused beams and their potential applications in many fields such as nonlinear optics, microscopy, and plasmonics have been studied over the last years [172-189]. A combination of optical techniques such as diffraction, interferometry, and holography might be used in order to control the complex amplitude and polarization distributions of the input field, for instance, see [190-200].

This section describes the experimental setup for generating highly focused beams with arbitrary complex amplitude and phase distributions and introduces a relatively simple method to retrieve the corresponding vector components from their corresponding intensity patterns recorded in two observed planes.

In subsection 6.1, we describe an optical setup appropriate for generating beam profiles with arbitrary intensity and phase distribution. The quality of the produced beams using a spatial light modulator and a digital holography technique is assessed at the entrance pupil and at the focal plane of a high-NA microscope objective.

Despite the intensity patterns that can be easily recorded, the phase information of optical fields can not be obtained by means of a CCD camera. In subsection 6.2, we apply a phase retrieval algorithm to retrieve the complex amplitudes of the transverse components of a highly focused EM field in the focal area.

In subsection 6.3, we propose a method for retrieving the longitudinal component of highly focused EM fields using a conventional imaging system.

6.1. Optical setup

The experimental setup is sketched in Fig. (6.1), which is developed by modifying the optical setup sketched in Fig. (4.1).

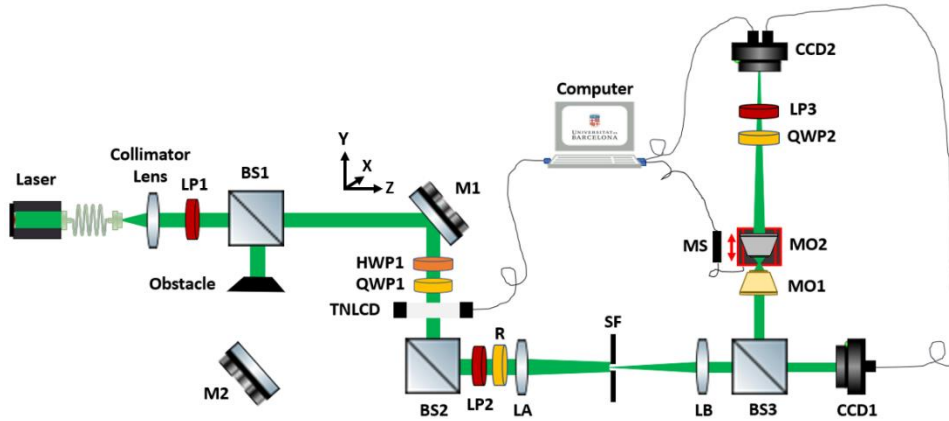


Fig. 6.1. The sketch of the experimental setup. R stands for a retarder which can be a QWP or Vortex for providing circularly or radially polarized beam, respectively. MO stands for microscope objective. MS stands for the movable stage. Figure from [139] under the CC Attribution 3.0 Unported License.

According to the optical setup sketched in Fig. (6.1), the fiber end of a pig-tailed laser (Thorlabs LP520-SF12@ 514 nm) is located at the back focal plane of a lens in order to collimate the laser beam. Then, the optical beam is modulated by means of LP1, HWP1, QWP1, TNLC display, and LP2, as explained in subsection 4.2. Note that the left arm of the Mach-Zehnder interferometer is blocked by an obstacle. A vortex retarder (ThorLab, WPV10L-532) or a QWP denoted by R is added after LP2 to provide a radially or circularly polarized beam, respectively. In order to provide radial polarization, the fast axis of the vortex retarder was placed parallel to the y-axis. In order to provide a circular polarization, the fast axis of QWP was rotated 45° with respect to the x-axis. Note that for providing a linearly polarized beam, retarder R (vortex retarder or QWP) can be easily removed.

The beam is separately imaged at the entrance pupil of microscope objective MO1 (Nikon Plan Fluorite N40X-PF with NA=0.75) and at the sensor plane of CCD1 by means of the 4f-system and beam splitter BS3. Microscope objective MO2 (Nikon with NA=0.8) is mounted on a movable stage driven by a motorized device (Newport LTA-HL) with uni-directional repeatability of ± 100 nm. MO2 has been used to scan different planes close to the focal plane of MO1

and image them to the sensor plane of the CCD2 camera (Stingray with a 14-bit depth and a pixel pitch of $3.75\ \mu\text{m}$). Note that MO2 has a larger NA than MO1 to collect the entire beam. Furthermore, the actual magnification of the imaging system (as shown in Fig. (6.2)) provided by MO2 was obtained by imaging a USAF target placed in the front of MO2, resulting in a 100x and spatial sampling of 37.5 nm. LP3 and QWP2 were used to obtain a set of six polarimetric images, as explained in subsection 3.1.

The performance of the experimental setup can be summarized in three parts: Polarized beam generator, Focusing system, and Imaging system, as shown in Fig. (6.2).

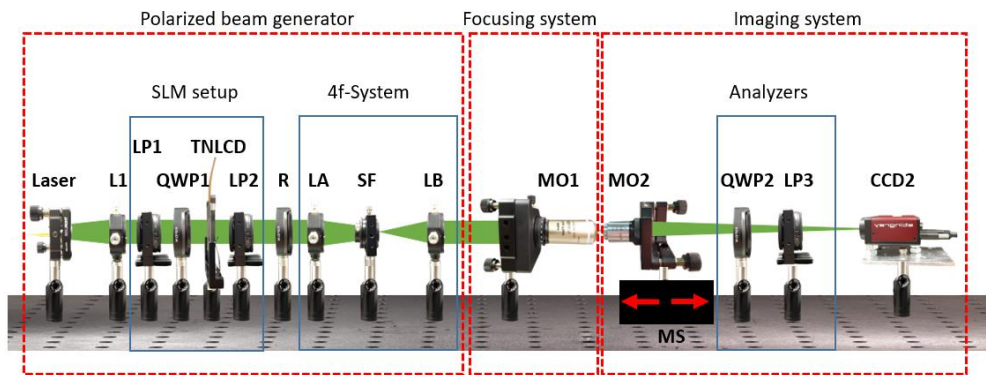


Fig. 6.2. The effective illustration of the experimental setup included three main parts: polarized beam generator, focusing system, and imaging system. Figure adapted from [201] under a Creative Commons By 4.0 license.

The operation condition of the first part (Polarized beam generator) is explained in subsection 4.2, including characterizing the TNLC display and a 4f spatially filtering system to remove the diffraction orders caused by DPH Arrizón's approach and pixelated structure of the display. In part 2 (Focusing system), the modulated and polarized laser beam that reached the entrance pupil of MO1 is focused.

In part 3 (Imaging system), since the MO2 is mounted on a movable stage, different planes near the focal plane of MO1 can be scanned and imaged at the sensor plane of CCD2.

In order to evaluate the operation of the experimental setup, we considered two differently polarized wave functions and compared the experimentally recorded polarimetric images with the numerical ones.

The first example is a (1,1)-Hermite-Gaussian (HG_{11}) with the wave equation given by

$$\text{HG}_{11} = \frac{4xy}{w_0^2} \exp\left(-\left(\frac{r}{w_0}\right)^2\right) \text{circ}\left(\frac{r}{R}\right), \quad (6.1)$$

where $r = \sqrt{x^2 + y^2}$, w_0 is the beam waist ($w_0 = R/2$), and R is the radius of the circular beam support, which is equal to 3.75 mm. The first row of Fig. (6.3) indicates the amplitude and phase of HG_{11} , respectively, whereas the second row demonstrates the nearest accessible values predicted by the KNN classifier, as explained in subsection 4.3.

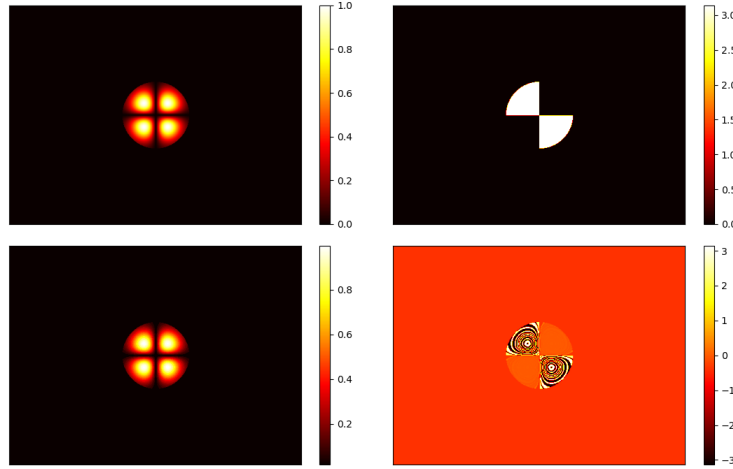


Fig. 6.3. The first row shows the distribution of the amplitude and phase of HG_{11} , respectively. The second row shows their nearest values predicted by the KNN classifier. Figure from [139] under the CC Attribution 3.0 Unported License.

The second example is a (0,1)-Laguerre-Gaussian (LG_{01}), in which the complex wave equation is

$$\text{LG}_{01} = \left[\left(\frac{2x}{w_0}\right) + j \left(\frac{2y}{w_0}\right) \right] \exp\left(-\left(\frac{r}{w_0}\right)^2\right) \text{circ}\left(\frac{r}{R}\right). \quad (6.2)$$

The amplitude and phase distribution of LG_{01} and their nearest accessible values predicted by the KNN classifier are shown in the first and second rows

of Fig. (6.4). The corresponding CGHs for HG_{11} and LG_{01} are shown in Fig. (6.5).

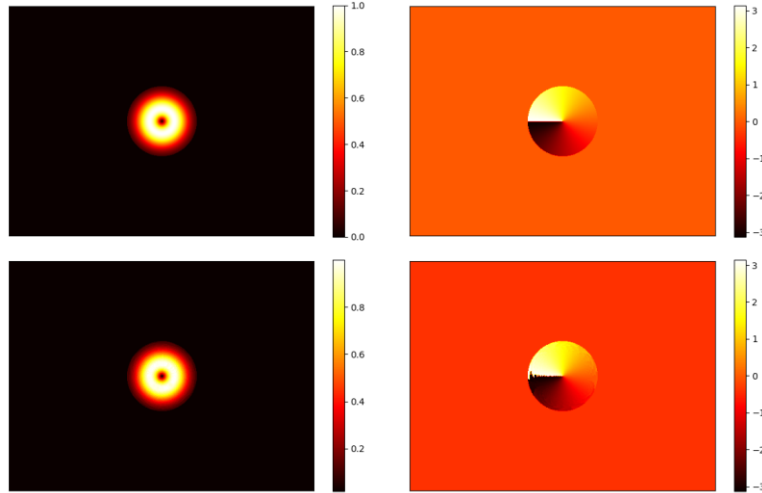


Fig. 6.4. The first row shows the numerical distribution of the amplitude and phase of LG_{01} , respectively. The second row shows their nearest values predicted by the KNN classifier. Figure from [139] under the CC Attribution 3.0 Unported License.

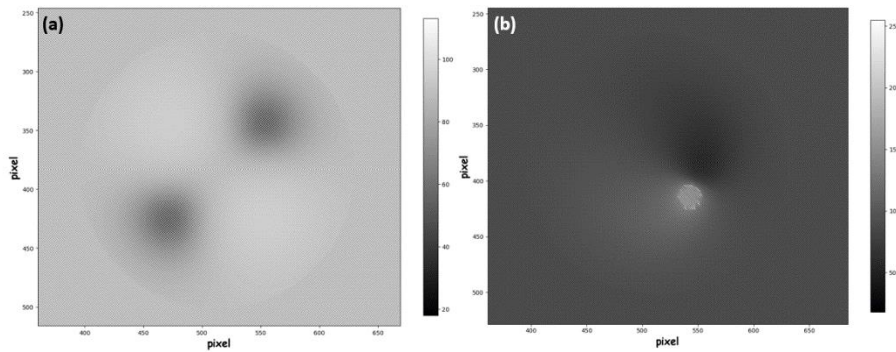


Fig. 6.5. The CGHs corresponding with (a) HG_{11} and (b) LG_{01} . The practical part of CGHs is selected for illustration purposes. Figure from [139] under the CC Attribution 3.0 Unported License.

The required time for generating the CGHs corresponding with HG_{11} and LG_{01} with a resolution of 768×1024 pixels were 1.92 and 5.53 seconds, respectively. Since the intensity pattern of a beam at the focal plane strongly depends on its polarization state at the entrance pupil of MO1, two different states of polarization were considered to compare the experimental results with the numerical ones. The numerical calculations have been implemented by

applying the focused field calculation method, as explained in subsection 3.2.1. Figures (6.6a) and (6.6b) show the intensity patterns of beam HG_{11} and LG_{01} recorded by CCD1.

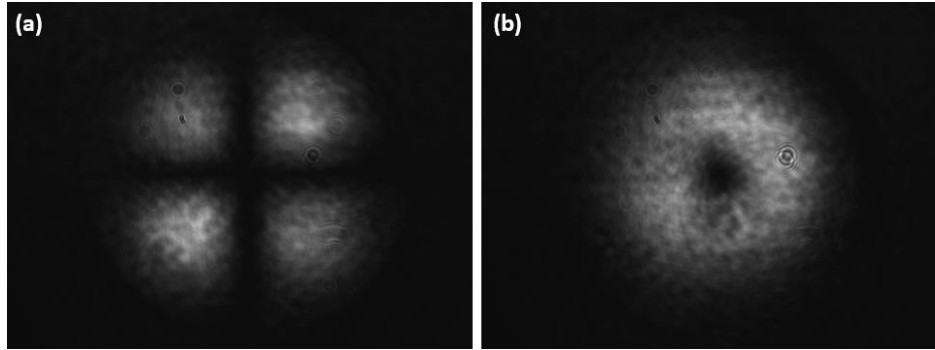


Fig. 6.6. The intensity patterns corresponding to beams (a) HG_{11} and (b) LG_{01} recorded by CCD1. Figure from [139] under the CC Attribution 3.0 Unported License.

Fig. (6.7) indicates the intensity patterns of the circularly polarized HG_{11} beam at the focal plane of MO1. The first row indicates the Stokes images, which are obtained numerically, whereas the second row shows the intensity measurement of the Stokes images, which are recorded by CCD2. The Stokes images are denoted by $I_{\delta,\theta}$, where θ and δ are the rotation angle of the axis of LP3 and the phase delay introduced by means of QWP2 with respect to the x-axis, respectively. Moreover, the polarimetric images are normalized by the maximum intensity of the transverse components of the electromagnetic field.

In a similar way, Fig. (6.8) indicates the Stokes images correspond to the radially polarized LG_{01} beam. As results show, the obtained Stokes images are in excellent agreement with the numerical ones. However, the state of polarization is altered slightly due to the imperfection of applied retarders. In conclusion, the results validate the performance of the optical setup for generating highly focused beams and correspondingly recording the intensity patterns of the transverse components. In order to retrieve the complex amplitude of transverse components, their phase distributions should be obtained, which is explained in the next subsection.

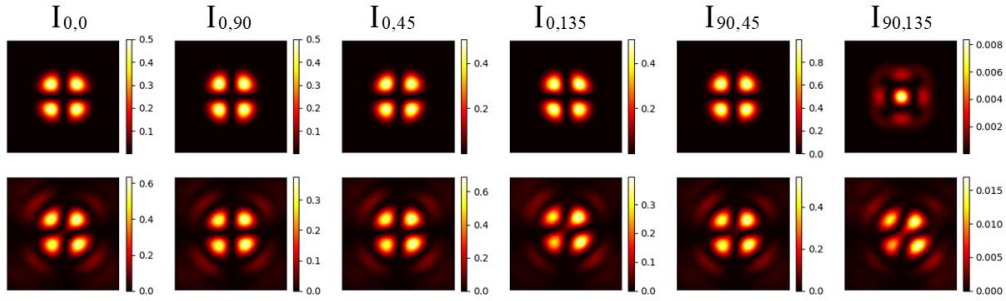


Fig. 6.7. The stokes images correspond to the circularly polarized HG_{11} beam at the focal plane. The first row shows the numerical results, while the second row demonstrates the recorded intensity by CCD2. The size of each image is $3 \mu\text{m}$. Note that the values on the color bar corresponding to $I_{90,135}$ are very small compared to the other polarimetric images. Figure from [139] under the CC Attribution 3.0 Unported License.

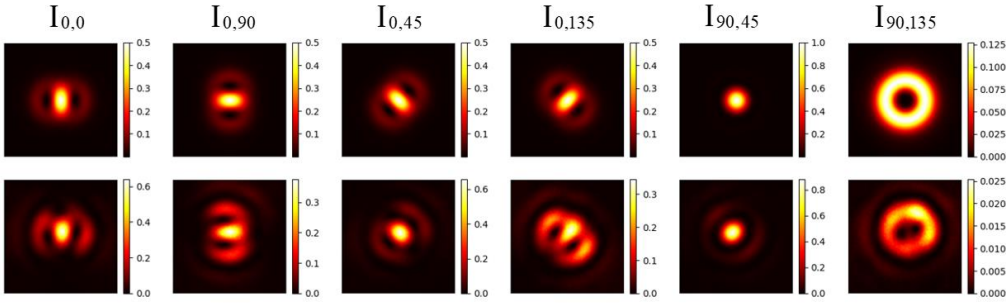


Fig. 6.8. The stokes images correspond to the radially polarized LG_{01} beam at the focal plane. The first row shows the numerical results, while the second row demonstrates the recorded intensity by CCD2. The size of each image is $3 \mu\text{m}$. Note that the values on the color bar corresponding to $I_{90,135}$ are very small compared to the other polarimetric images. Figure from [139] under the CC Attribution 3.0 Unported License.

6.2. Recovering the transverse components

Despite the amplitude of the transverse components, their phase distribution can not be inferred from a conventional camera. Here, we apply an iterative phase retrieval algorithm based on a derivative approach from the Gerchberg-Saxton algorithm and the input-output Fienup algorithm [202, 203].

Since optical beams considered in this work propagate in free space, the planes perpendicular to the direction of the propagation are computationally connected by means of the Fresnel transfer function [204]. Note that the theory of

propagation of the EM field in free space is explained in subsection 3.2.2.1, and the input-output Fienup phase retrieval algorithm is explained in subsection 3.4.

In order to obtain the phase distribution of the transverse components, we apply an iterative algorithm (see subsection 3.4) on the recorded modulus of each transverse component of the EM field separately at two different planes perpendicular to the z-axis

$$A_{i1}^2 = |E_i(x, y, z_1)|^2, \quad (6.3a)$$

$$A_{i2}^2 = |E_i(x, y, z_2)|^2,$$

(6.3b) with $i = x, y$. The relationship between two planes separated a distance $z = z_2 - z_1$ is

$$U(x, y, z) = \frac{1}{4\pi^2} \iint_{k_x^2 + k_y^2 \leq k^2} \hat{U}(k_x, k_y, 0) \exp(jk_z z) \exp[j(k_x x + k_y y)] dk_x dk_y, \quad (6.4)$$

where $\hat{U}(k_x, k_y, 0)$ is the spectrum at the first plane ($z = z_1$), and $U_{i1}(x, y, z_1) = A_{i1} \exp(j\phi_{i1})$ and $U_{i2}(x, y, z_2) = A_{i2} \exp(j\phi_{i2})$. The propagation of the EM field is performed using the angular spectrum of plane waves and the free space transfer function (see Eqs. (3.2-13) and (3.2-18)). Note that other propagation methods could be used as long as the size of the window is not modified [205, 206].

The iterative algorithm begins with an initial guess (random distribution) of ϕ_{i1} . The iterative algorithm includes propagating $U_{i1}(x, y, z_1)$ to plane z_2 applying Fresnel propagation, reserving the obtained phase (ϕ_{i2}) and replacing the obtained modulus with the measured modulus at plane z_2 (A_{i2}), back-propagating $U_{i2}(x, y, z_2)$ to plane z_1 , reserving the obtained phase (ϕ_{i1}) and replacing the obtained modulus with the measured modulus at plane z_1 (A_{i1}). For each iterative process, the error is measured, and the process continues until arriving the measured error close to zero. Note that the detailed discussion about the phase retrieval algorithm used in this work, such as accelerating the algorithm [207] and solving the stagnation at local minima of the error function [208] is beyond the scope of this thesis. For obtaining more information, see [201].

By means of this algorithm, the phase of the transverse components, $E_x(x, y, z_1)$ and $E_y(x, y, z_1)$, can be retrieved. However, there is a relative phase between

the two transverse components that can be obtained by means of polarimetric analysis according to the measurement of Stokes images in the observation planes [209]. Once the electric field is determined at a given plane, the beam can be propagated to any new location [210].

Note that for doing this experiment, we had to replace the fiber of the pig-tailed laser with another one (Thorlabs LP520-SF115) with a wavelength of 520 nm due to a technical problem. Correspondingly, the magnification and the resolution of the imaging system were measured in a similar way that is explained in subsection 6.1, resulting in $M=50x$ and spatial sampling of 75 nm.

Two different beam profiles were considered to recover their corresponding transverse and longitudinal components in the focal region. Retrieving the longitudinal component is explained in subsection 6.3.

The first beam is a radially polarized Gaussian-like beam with a vortex phase given by

$$E_i(\rho, \phi) = [\cos \phi, \sin \phi]^T \rho \exp(j\phi) \exp\left(-\frac{\rho^2}{f^2 \text{NA}_e^2}\right) \text{circ}\left(\frac{\rho}{f \text{NA}_e}\right), \quad (6.5)$$

where $\rho = (x, y, 0)$, ϕ is the azimuthal coordinate, and $f = 5$ mm is the focal length of MO1. NA_e is the effective pupil size of the beam, which was determined according to the present size of the beam.

The second beam is a linearly polarized (1,1)-Hermite-Gauss with the wave function given by

$$E_i(\rho) = \left[0, \text{H}_1\left(\frac{\sqrt{2}x}{f \text{NA}_e}\right), \text{H}_1\left(\frac{\sqrt{2}y}{f \text{NA}_e}\right) \right]^T \exp\left(-\frac{\rho^2}{f^2 \text{NA}_e^2}\right) \text{circ}\left(\frac{\rho}{f \text{NA}_e}\right). \quad (6.6)$$

We replaced NA (numerical aperture of MO1) with NA_e , because each optical element's aperture limits the size of the beam as it propagates. So, the size of the beam is limited by propagating through each optical element, specifically by the EP of MO2 (the EP of the objective is not physically accessible nor measurable). Since the spectra of each component are limited by the physical size of the EP of the microscope, all generated beams are band limited. Then, the diameter of the effective pupil size for each beam was obtained by calculating the half diameter of the autocorrelation of the corresponding intensity.

The calculation of the autocorrelation of the recorded intensity regarding the radially polarized vortex and the Hermite–Gauss beams gave $\text{NA}_e = 0.406$ and

$NA_e = 0.379$, respectively. Note that the diameter of the autocorrelation is twice the diameter of the beam. The Stokes parameters for two experimentally measured planes (first and second rows) for the radially polarized vortex beam are shown in Fig. (6.9). The Stokes parameters were obtained by means of Eqs. (3.1-12), and the distance between the two observed planes was $2 \mu\text{m}$. Our investigation shows that obtained phases converge to a spherical wave regardless of the shape of the beam for distances shorter than $2 \mu\text{m}$.

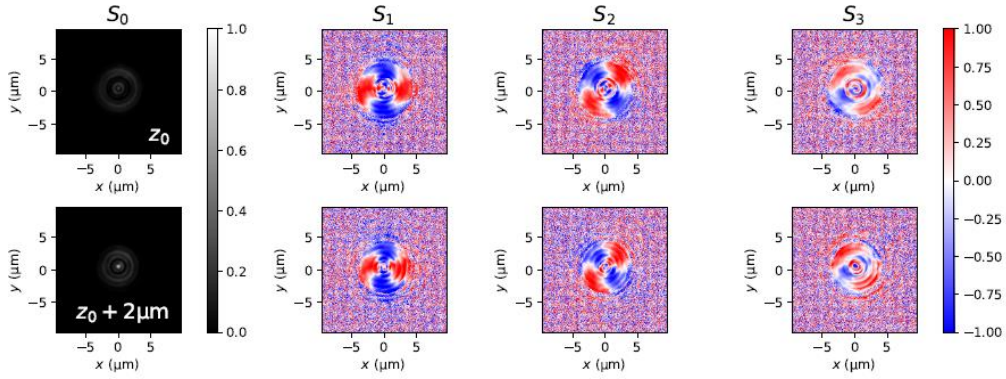


Fig. 6.9. Stokes parameters for the radially polarized vortex beam measured at two planes perpendicular to the optical axis. The distance between these two planes is $2 \mu\text{m}$. Figure from [201] under a Creative Commons By 4.0 license.

The position z_0 shown in Fig. (6.9) is close to the focal plane. As the Stokes parameters indicate, the polarization state of the beam is a complex combination of radial and circular polarizations distributed along the width of the beam. Nevertheless, the exact polarization state of the beam alters as it propagates, especially near the center of the beam. This might be attributed to the spiral phase of the beam, which curls and uncurls while changing the phase difference between components. Fig. (6.10) demonstrates the recovered phases, ϕ_x and ϕ_y , by means of the iterative phase retrieval algorithm on amplitudes $\sqrt{I_{0,0}}$ and $\sqrt{I_{0,90}}$ at planes z_0 and $z_0 + 2 \mu\text{m}$, respectively.

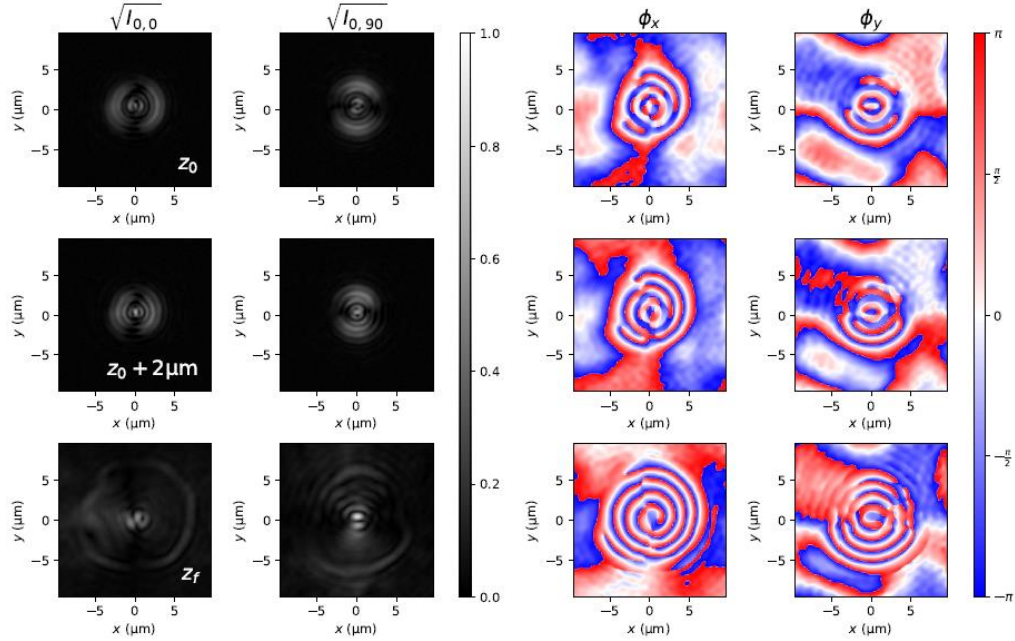


Fig. 6.10. Vortex beam: Amplitudes and phases of the two experimentally observed planes (first two rows) and the synthetically refocused focal plane (bottom row). Figure from [201] under a Creative Commons By 4.0 license.

Since each phase is recovered separately, the origin of phases for both ϕ_x and ϕ_y might be different. We determined this constant random phase difference δ_0 at the maximum irradiance of the beam $\max(I_{0,0} + I_{0,90})$ to be the one given by the Stokes parameters (Fig. (6.9)), $\delta_0 = \arctan(S_3/S_2)$. With this information, the beam was propagated up to the focal plane (z_f).

Note that z_f cannot be easily set experimentally with enough precision. Hence, it is numerically estimated as the plane where the circle of the smallest size of the beam can be, or the beam is tightly concentrated. The results show that the phase difference (δ_0) in the focal plane is $\phi_x - \phi_y = 0.062$ rad, whereas it theoretically should be $\pi/2$ rad. This discrepancy might be due to some optical elements introducing an uncontrolled phase difference between components caused by aberrations, misalignment, and the error of the codification algorithm (DPH Arriz3n's approach). In this regard, the discrepancy observed experimentally was compensated by including the phase difference between theory and experiment in the simulations of the beam in Eq. (6.5).

Since the Hermite–Gaussian beam is linearly polarized, calculation of the Stokes parameters was unnecessary. Figure (6.11) indicates the transverse amplitudes of the experimentally measured beam and the synthetically refocused at the focal plane. The x-component, although present, is very weak in comparison with the y-component and does not affect the shape of the total irradiance. Its presence can be attributed to the imperfection of used retarders and polarizers.

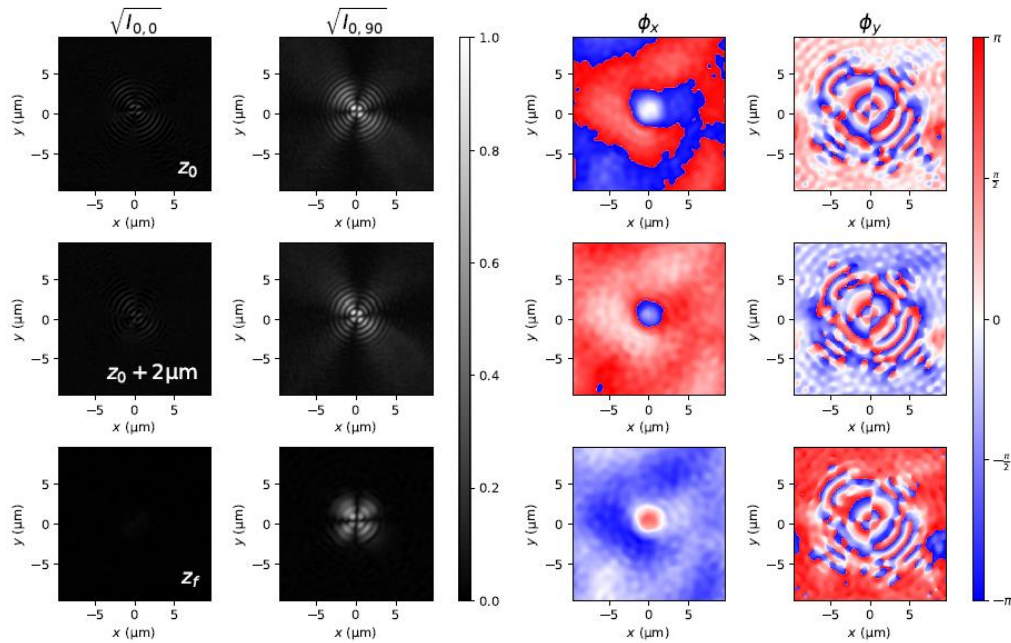


Fig. 6.11. Hermite–Gauss beam: Amplitudes and phases of the two experimentally observed planes (first two rows) and the synthetically refocused focal plane (bottom row). Figure from [201] under a Creative Commons By 4.0 license.

6.3. Recovering the longitudinal component

In contrast to the intensity patterns of transverse components of a highly focused EM field that can be recorded by an imaging system, the longitudinal component can not be recorded or observed directly by a conventional imaging system [70, 71]. However, several techniques have been reported for direct measuring of the longitudinal component, which are typically complex or designed for specific applications [211-220].

In this subsection, we propose a new method by estimating the longitudinal component using Gauss' theorem, provided the complex amplitude and polarization of the transverse field are known.

In subsection 3.2.2.1, the numerical method was described for obtaining the longitudinal component of a highly focused EM field from its transverse components. Subsequently, in subsection 6.2, we retrieved the complex amplitude of the transverse vector $\mathbf{E}_\perp(\mathbf{k}_\perp; z=0)$ using the phase retrieval algorithm. Correspondingly, the retrieved longitudinal components $\mathbf{E}_z(\mathbf{k}_\perp; z=0)$ for two beams considered are shown in Fig. (6.12), which are obtained by applying Eq. (3.2-20) on the retrieved $\mathbf{E}_\perp(\mathbf{k}_\perp; z=0)$.

The results demonstrate an acceptable agreement between the theoretical and experimentally estimated longitudinal components. However, the discrepancy observed for the radially polarized vortex beam (as explained in the previous subsection) causes a difference between the theoretically expected longitudinal component and the recovered one. Although the shape of the longitudinal component for a radial vortex beam should be a doughnut, the two protruding lobes (shown in Fig. (6.12b)) were obtained theoretically by modifying Eq. (6.5), according to an unforeseen phase difference that was observed experimentally. This phase difference might be caused by aberrations introduced by optical elements in the experimental setup or/and the imperfections in the hologram at the EP of the optical system, mainly due to the DPH method used.

The results regarding the Hermite–Gauss beam demonstrate an excellent agreement between theory and experiment due to this beam being linearly polarized, and the stokes analysis was not necessary to be carried out.

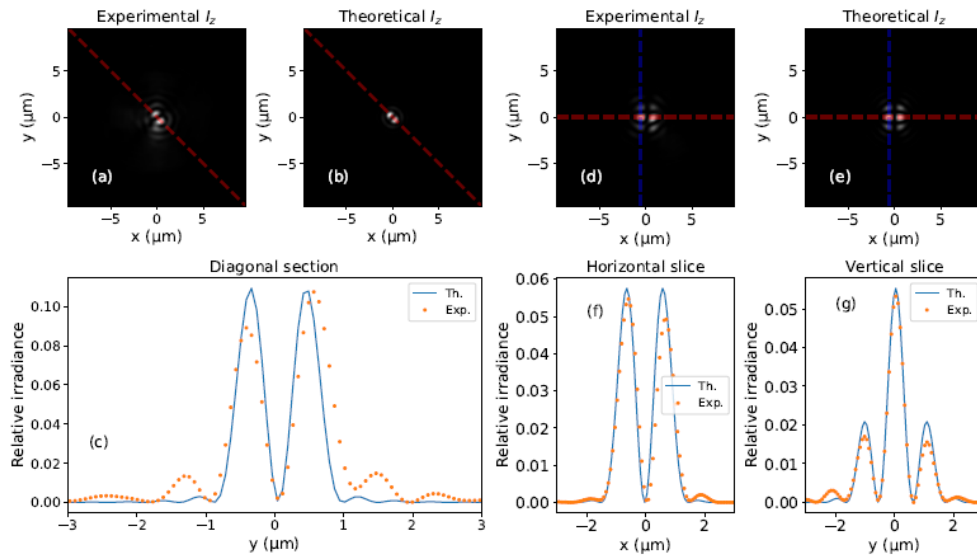


Fig. 6.12. Estimation and theoretical irradiances at the focal plane of the microscope objective: (a-c) vortex beam: (a, b) 2D irradiance distribution; (c) profile of the irradiance across the diagonal depicted in red. The solid blue line and the orange dots correspond to the theoretical and experimental values, respectively. (d-g) Hermite-Gauss beam: (d, e) 2D irradiance distribution; (f, g) irradiance profiles across the horizontal and vertical lines superimposed on the experimental image. As in the previous case, orange points represent values obtained from experimental measures, whereas the blue line has been obtained from theoretical calculations. Figure from [201] under a Creative Commons By 4.0 license.

7. Estimation of Zernike polynomials for a highly focused EM field using polarimetric mapping images and neural networks

In the previous section, we described a relatively simple method for visualizing the longitudinal component of highly focused beams using conventional imaging systems. Since recovering the longitudinal component depends directly on the quality of retrieving the transverse components, considering any possible error in the optical setup is essential. In general, one of the main errors in a complex optical system is the aberration caused by optical elements and the misalignment.

Aberration is a well-known topic in adaptive optics, astronomy [221], optometry [222], coherent diffractive imaging [223], and ptychography [224]. An aberrated wavefront can be measured by a Hartmann-Shack wavefront sensor [225] or conventionally by interferometric methods [226,227]. However, the first one requires the device, and the interferometric techniques require a complex optical setup, high-resolution cameras, and controlling the vibration between two arms of the interferometer.

Since simulated artificial neural networks (ANN) have been proved to be a very powerful tool in many fields of research, ANNs have also been used for aberration measurements in several optical systems. For instance, applying neural networks to determine the spherical aberration coefficient of a confocal objective from an axial intensity response [228] or using neural networks designed to estimate optical aberrations of the Hubble Space Telescope [229]. Furthermore, neural networks have been used for wavefront reconstruction considering aberrated wavefronts [230, 108].

In particular, White et al. proposed a practical method applicable for reconstructing the wavefront of a focused beam from a measured diffraction pattern [108]. Since the phase property of optical waves can not be recorded by intensity detectors (for instance, CCD cameras), they applied a phase-retrieval framework based on a neural network to solve the phase problem. In their approach, the neural network was trained by the labeled training datasets obtained by simulating aberrations according to Zernike polynomials. On the one hand, the labeled objects (outputs of the neural network) were obtained by applying the Fourier transform to a Gaussian beam which was multiplied by random phases consisting of Zernike polynomials with random scalar coefficients. On the other hand, the neural network inputs were diffraction

patterns obtained by simulating the propagation of the objects through a diffractive mask consisting of a thin, absorbing metal film on a silicon nitride membrane with holes. In this work, we used the way they applied to simulate the aberrated wavefronts to obtain a training dataset.

In this section, we present an alternative approach to estimating the Zernike polynomials at the focal plane regarding a highly focused EM field by means of the polarization property of optical beams. Despite the phase, the polarization state of optical waves is simply measurable using a linear polarizer followed by a quarter-wave plate and a CCD camera. In this regard, a radial polarization is imposed on randomly aberrated Gaussian-like beams. Then the focused fields are simulated through a high-NA microscope objective to calculate the Stokes images at the focal plane. Accordingly, we introduce the polarimetric mapping images (PMI) to a convolutional neural network in order to map the Zernike polynomials based on the polarimetric information. Our approach takes advantage of recording the Stokes images at a single plane (focal plane) and eliminating the necessity of phase retrieval.

The following text is organized as follows: Subsection 7.1 reviews the Zernike polynomials. Subsection 7.2 describes the simulation procedure, including the training dataset and the neural network model. Subsection 7.3 discusses the results with possible improvements.

7.1. Zernike polynomials

The Zernike expansion represents wavefront aberration functions, which is a set of polynomials indexed by the nonnegative integers corresponding with the degree of polynomials that are orthogonal on a circular pupil. The even and odd Zernike polynomials are defined by $Z_n^m(\rho, \varphi) = R_n^m(\rho)\cos(m\varphi)$ and $Z_n^{-m}(\rho, \varphi) = R_n^m(\rho)\sin(m\varphi)$, respectively, where n and m are nonnegative integers with the condition $n \geq m \geq 0$, φ and ρ are the azimuthal angle and the radial distance, respectively, and $R_n^m(\rho)$ are the radial polynomials given by

$$R_n^m(\rho) = \begin{cases} \sum_{k=0}^{\frac{n-m}{2}} \frac{(-1)^k (n-k)!}{k! \left(\frac{n+m}{2} - k\right)! \left(\frac{n-m}{2} - k\right)!} \rho^{n-2k} & (n-m) = \text{even} \\ 0 & (n-m) = \text{odd} \end{cases},$$

(7.1) with a special value $R_n^m(1) = 1$.

7.2. Simulation

Here we consider a numerical framework adjustable to the experimental setup that we used to estimate the longitudinal component of highly focused beams, as explained in subsection 6.1. Without loss of generality, our approach can be adapted to any complex optical system dealing with aberrations and focused fields. The numerical calculations have been carried out using Python 3.7.5 and a Laptop with CPU i7-1165G7 (2.8 GHz) and 16 GB RAM. Besides, the neural network has been implemented by TensorFlow 2.1 on GPU: NVIDIA Geforce M450.

7.2.1 Training dataset

The training dataset was obtained by calculating aberrated focused fields corresponding with a radially polarized Gaussian-like beam with random phases described by Zernike polynomials. Hence, the input beam is

$$E_0 = \sqrt{r} \exp\left(-\left(r/w_0\right)^2\right) \exp(j\phi_z), \quad (7.2)$$

where $r = \sqrt{x^2 + y^2}$ and w_0 is the beam waist. The phase distortion caused by aberrations is introduced by ϕ_z , which is obtained by a combination of random coefficients of the first four order (15 Zernike polynomials) as follows:

$$\phi_z = c_1 Z_0^0 + c_2 Z_1^{-1} + c_3 Z_1^1 + c_4 Z_2^0 + \dots + c_{15} Z_4^4, \quad (7.3)$$

where c_i denotes a randomly-selected coefficient ranging from 0 to 0.01. Note that this range should be scaled and calibrated based on the experimental measurements for the specific application. For instance, in [228], the authors calibrated the aberration coefficient $[-0.7\lambda \sim 0.3\lambda]$ into $[0.05 \sim 0.95]$. The vector components of the focused field for the radially polarized input beam E_0 (Eq. (7.2)) is calculated by means of Eqs. (3.2-3), (3.2-5), and (3.2-7), resulting in

$$E_x(x, y, 0) = -\frac{jf\lambda}{4\pi^2} \text{FT} \left[E_0 \cos \varphi \sqrt{\cos \theta} \right], \quad (7.4)$$

$$E_y(x, y, 0) = -\frac{jf\lambda}{4\pi^2} \text{FT} \left[E_0 \sin \varphi \sqrt{\cos \theta} \right], \quad (7.5)$$

$$E_z(x, y, 0) = -\frac{jf\lambda}{4\pi^2} \text{FT} \left[E_0 \sin \theta / \sqrt{\cos \theta} \right]. \quad (7.6)$$

We considered 2000 random possibilities of ϕ_z , introduced into Eq. (7.2). Then, for each possibility, the vector components of the focused field were obtained using Eqs. (7.4) to (7.6). Subsequently, the corresponding Stokes images were calculated at the focal plane by the matrix multiplication of the transverse components of the focused field and a linear polarizer and a quarter-wave plate in which their axes were rotated appropriately based on the Jones matrix representation (see subsection 3.1). Besides, the Stokes parameters were obtained by means of Eq. (3.1-12). Finally, for each possibility, we formed an image named polarimetric mapping image (PMI) based on the calculated Stokes parameters. Actually, PMIs are multidimensional arrays, but we name them images for the sake of simplicity. To the best of our knowledge, this is the first report of PMIs for pattern classification and object recognition.

In this work, a PMI consists of three channels: S_1/S_0 , S_2/S_0 , and S_3/S_0 . Thereby, these PMIs are the inputs of the CNN model for training the machine. We calculated 2000 PMIs corresponding to 2000 random possibilities of ϕ_z . Furthermore, the number of elements of the dataset was increased to 18000 by adding Gaussian noises with a variance ranging from 0 to 0.25 to each channel of every PMI.

Figure. (7.1) shows the Stokes images obtained for a radially polarized Gaussian-like beam without aberrations at the focal plane. Figure. (7.2) indicates the Stokes images obtained for a radially polarized Gaussian-like beam with the coefficients of Zernike polynomials equal to $c_1= 4.8 \times 10^{-3}$, $c_2= 4.8 \times 10^{-3}$, $c_3= 2.4 \times 10^{-3}$, $c_4= 6.2 \times 10^{-5}$, $c_5= 4.7 \times 10^{-3}$, $c_6= 6.8 \times 10^{-3}$, $c_7= 8.5 \times 10^{-3}$, $c_8= 4.4 \times 10^{-4}$, $c_9= 5.9 \times 10^{-3}$, $c_{10}= 4.7 \times 10^{-3}$, $c_{11}= 8.1 \times 10^{-3}$, $c_{12}= 4.5 \times 10^{-4}$, $c_{13}= 5.9 \times 10^{-3}$, $c_{14}= 4.8 \times 10^{-3}$, $c_{15}= 5.1 \times 10^{-3}$, $c_{16}= 5.2 \times 10^{-3}$. Figure. (7.3) shows the normalized Stokes parameters, which form a PMI, corresponding with Stokes images shown in Figs. (7.1) and (7.2). Finally, the total dataset was split into two sets: 80% for the training dataset (14400 PMIs) and 20% for the test dataset (3600 PMIs).

7.2.2 Neural network model

The applied neural network model is a sequential model summarized in Fig. (7.4). The model consists of three convolutional layers with 32, 64, and 128 filter sizes and a kernel size of 3, accompanied by the hyperbolic tangent activation function. The batch normalization and average pooling layers are applied after each convolutional layer. Then, the resulting feature map is flattened into an one-dimensional array as an imaging outcome. Correspondingly, the image outcome is connected to 3000 neurons applying a dense layer by means of the sigmoid function. Next, 25% of connected neurons

are removed by a drop-out layer. Finally, the last dense layer provides 2000 probability distributions ranging from 0 to 1 by means of the softmax activation function, which is used to label 2000 possibilities of ϕ_z .

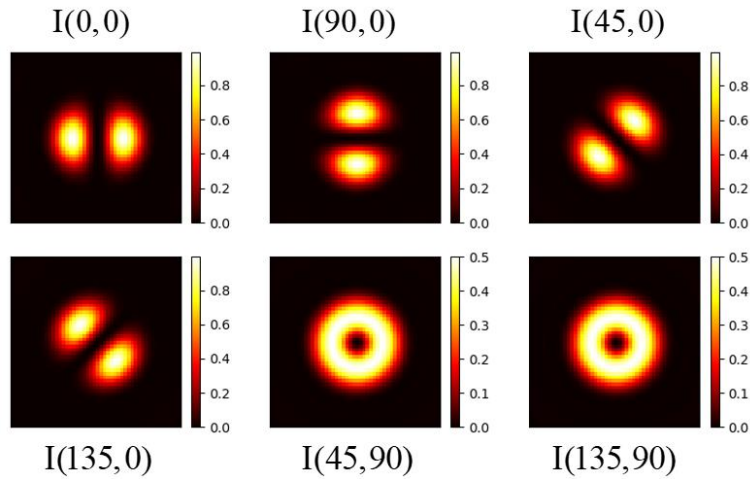


Fig. 7.1. Stokes images obtained at the focal plane corresponding to a radially polarized Gaussian-like beam.

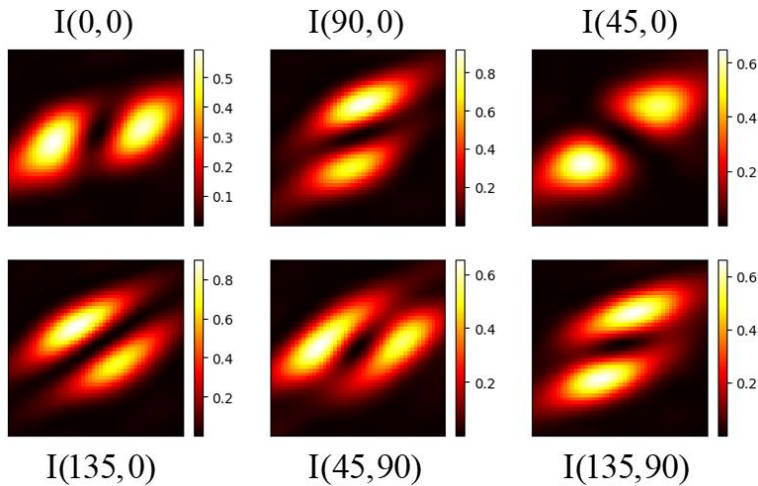


Fig 7.2. Stokes images obtained at the focal plane corresponding to a radially polarized Gaussian-like beam with a random phase obtained by Zernike polynomials.

Besides, the model was compiled with the root-mean-square error, the cross-entropy loss, and the accuracy as the optimizer, loss function, and performance metrics, respectively. To avoid overfitting, we monitored the accuracy and the

loss obtained after each epoch by separating a randomly-selected 20% of the training dataset as a valid test dataset. Note that the valid test dataset differs from the test dataset mentioned previously. In this regard, the training process was stopped after 50 epochs, when the error loss was decreasing while the valid error loss began increasing.

To sum up, the input of the model is PMIs with a size of $50 \times 50 \times 3$, and the output is the predicted Zernike polynomials coefficients, which were saved previously regarding each class label. The obtained accuracy and the loss error of the classification are 0.989 and 0.033, respectively. The obtained accuracy for predicting the test dataset is 0.978, which shows a high rate of success for predicting the unseen dataset.

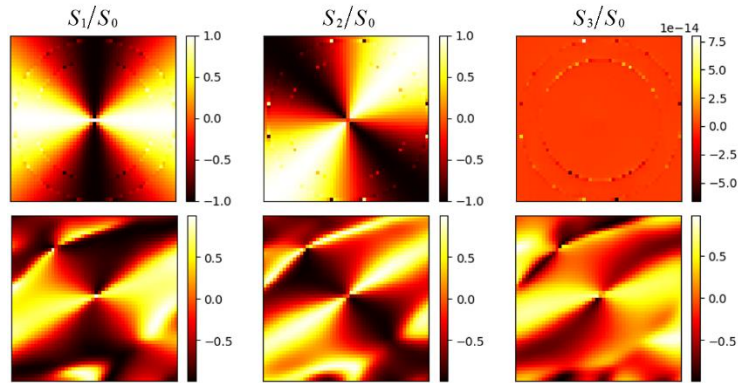


Fig. 7.3. The normalized Stokes parameters corresponding to a radially polarized Gaussian-like beam without aberrations (the first row) and with a random phase obtained by Zernike polynomials (the second row).

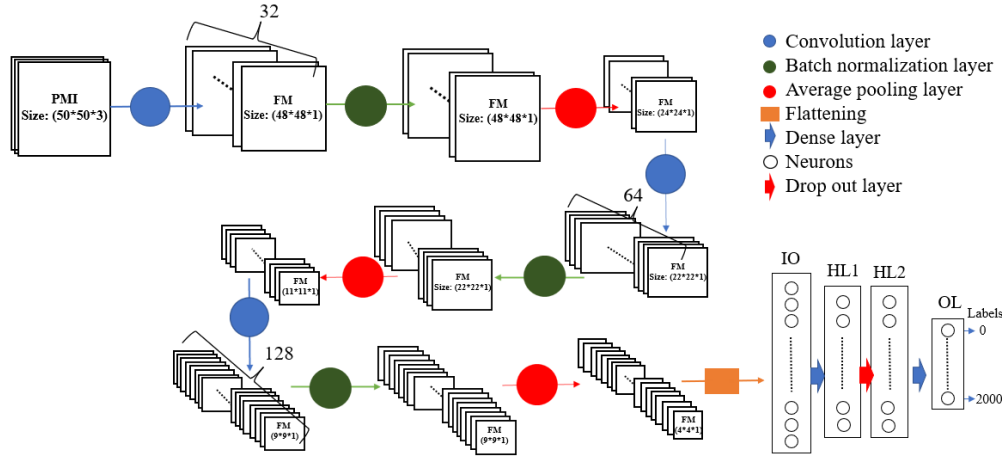


Fig. 7.4. CNN model. PMI, FM, IO, HL, and OL stand for polarimetric mapping image, feature-map, image-outcome, hidden layer, and output layer, respectively.

7.3. Discussion and conclusions

We demonstrated that by means of PMIs, the neural network model could successfully predict the Zernike polynomial coefficients of the aberrated beam based on polarimetric information. However, the training dataset can be easily enriched by adding more possibilities. The first fifteen aberrations were considered, including oblique astigmatism, horizontal and vertical coma, primary spherical, defocus (longitudinal position), tilt in x- and y-direction, etc.

This set of aberrations can be modified based on the experimental setup used for a specific application. As a result, the training dataset can be practically modified based on the type of application. Although we considered a uniform range ($[0,0.01]$) of the Zernike polynomials coefficients (c_i) but also this range might be practically selected as non-uniform coefficients based on the used experimental setup.

We imposed a radial polarization on the incident beam in order to provide different intensity patterns of the Stokes images. Other polarization states that fulfill this condition can be applied, for instance, spiral polarization or spatial-variant polarization.

Our approach aims to encode phase information into polarimetric information. In the future, we plan to extend the application of our approach for instant detection of the aberrated longitudinal component of highly focused fields

without the necessity of fully retrieving the transverse components. Figure (7.5) indicates the corresponding longitudinal component of the Stokes parameters shown in Fig (7.3).

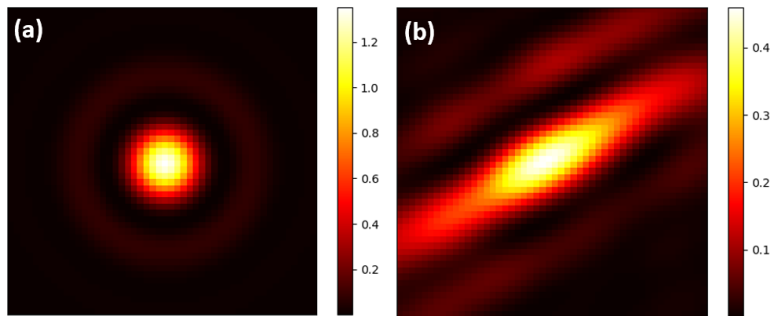


Fig. 7.5. Longitudinal component of a focused radially polarized Gaussian-like beam (a) without aberration (b) with aberrations obtained by the Zernike polynomials.

In conclusion, this approach can be applied for two purposes as follows:

- In order to calibrate a complex optical setup by detecting the Zernike polynomials coefficients at the focal plane by synthesizing a properly polarized beam at the EP of a focusing system.
- Instant reconstruction of aberrated wavefronts based on polarimetric information provided the beam used is known. In this case, applying phase recovery algorithms is not necessary anymore for wavefront sensing applications.

8. Secret sharing of optically obscured character codes in a highly focused EM field

In subsection 3.2.2, we described a method to obscure data into a highly focused EM field depending on the state of the input polarization and physical properties of the concentrated beam that requires a method for recovering encrypted data in the longitudinal component.

In section 6, we described a relatively simple method to recover the longitudinal component using conventional imaging systems that can be applied for decoding the encrypted information. However, due to the complexity of the experiment and according to the fact that the longitudinal component should be obtained by its lateral electric field, decoding the original data might be failed.

Very often, the practically obtained results suffer from the misalignment of optical elements, imperfection of polarizers/retarders, and aberrations such as spherical and distortion. All mentioned errors might cause various undesirable results in the decoding process, which demand a new encoding and decoding processes approach.

In recent years, applying Deep Neural Networks (DNNs) in phase retrieval algorithms has been increasing due to the ability of DNNs to make the algorithm robust [103-108, 231,232]. However, most of the reported algorithms are based on supervised learning, which demands a pre-defined training dataset.

In this section, we implement a visual object recognition technique using a supervised deep learning algorithm [233] by recording Stokes images at the focal plane. To implement this method, we use CEs (as explained in section 5) to encode 10-bit character codes into the holographic cells in order to synthesize laser beams at the entrance pupil of the focusing system to provide a supervised training dataset. Regarding the decoding process, we use the polarimetric mapping images (PMIs) at the focal plane to classify and correspondingly retrieve the original codes using a CNN model. Moreover, character codes are encrypted by Moni Naor and Adi Shamir's secret sharing technique [113] using the bitwise XOR operation.

8.1. Encrypting and encoding character codes into an optical beam

One of the well-known visual secret sharing schemes was developed by Moni Naor and Adi Shamir. Regarding the proposed scheme, an image is split into n shares ($n \geq 2$). Accordingly, the original image only can be decoded when all n -shares are accessible, and any $n-1$ shares unmask no information about the

original image. To provide a secure communication channel, we use the secret sharing scheme. Since each character code is transferred into 10-bit binary values, we split each character code into two shared-character codes by means of the bitwise XOR operation. A bitwise XOR is a binary operation that performs the logical inclusive OR operation on each pair of corresponding bits. The output of a logical function (XOR) is one if the inputs are not identical, whereas it is zero if the inputs are the same. Therefore, applying the bitwise XOR operation on two 10-bit binary values results in another 10-bit binary value. Each bit's binary value (0 or 1) is obtained by applying the XOR operation on each pair of corresponding bits.

The encryption process can be explained in three steps:

- According to the Unicode table, the original character code is transferred into the decimal value and correspondingly into 10-bit binary values, denoted by CE_{OR} .
- To define a 10-bit random key named CE_1 .
- To apply the bitwise XOR operation on CE_{OR} and CE_1 to obtain another CE named CE_2 , such as $CE_{OR} \text{ XOR } CE_1 = CE_2$.

Then two cipher-character codes CE_1 and CE_2 are encoded into holographic cells, as explained in section 4. For instance, we encrypt the character code ñ with decimal value 328 correspond to [0 1 0 1 0 0 1 0 0 1] binary values, in this way. Additionally, a 10-bit random key can be a character code like á with decimal value 225 and correspond to [0 0 1 1 1 0 0 0 0 1] binary values. Applying the bitwise XOR gives $CE_2 = [0 1 1 0 1 0 1 0 0 1]$, which is equal to decimal value 425, corresponding to character code Σ . Hence, each character code (CE_{OR}) is split into two cipher-character codes (CE_1 and CE_2) in order to share with two different optical systems A and B. Correspondingly, the original character code can be obtained by $CE_A \text{ XOR } CE_B = CE_{OR}$. The configuration of used CEs in this work is shown in Fig. (8.1).

The circular area is divided into two regions (concentric rings). The first region is a null and opaque area with a radius of $r = 1.8$ mm, as shown in black space. In contrast, the rest is the encoding area with a maximum radius of $R = 3.75$ mm, equivalent to the radius of the laser beam. Here, we limit ourselves to encoding 10-bit character codes, so we just consider CEs that consist of an annulus with ten angular sectors. However, the proposed algorithm can be applied for any arbitrary binary set, for instance, the full 16-bit Unicode set.

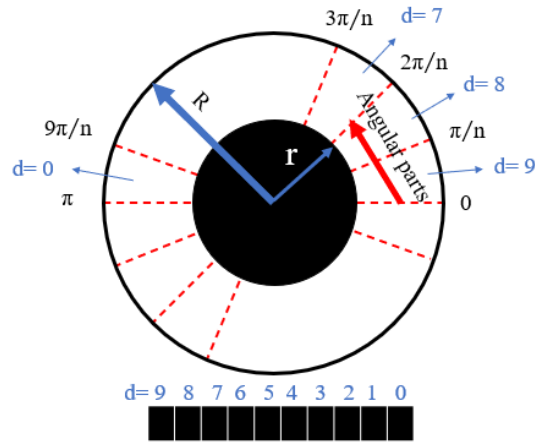


Fig. 8.1. Design of the Circular Encoder to encode 10-bit binary values. R and r denote the radius of the laser beam and the null region, respectively, while d stands for digit position. The encoded area is divided into 20 angular sectors divided by red dashed lines, while the black area shows the null region.

The advantage of the proposed binary approach is to synthesize the objects at the entrance pupil of the focusing system and correspondingly encode 1024 character codes, including most European alphabets, numbers, symbols, and punctuation characters. Significantly, CEs give a facility to obtain the supervised training datasets at the focal plane to eliminate the necessity of retrieving the vector components of a highly focused EM field. Three CEs, which encode character codes \check{n} , \acute{a} , and Σ are shown in Fig. (8.2).

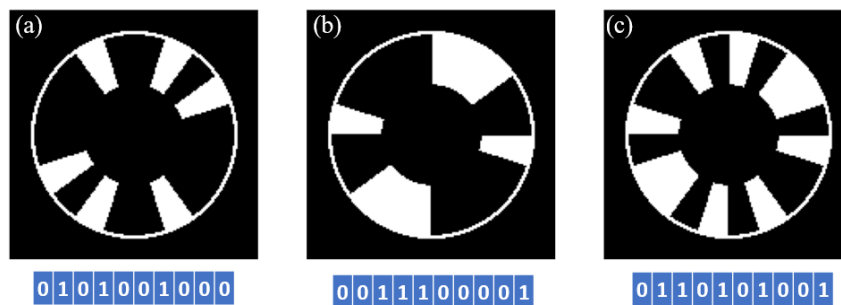


Fig. 8.2. CEs that encode character codes (a) Latin small letter N with caron, \check{n} , with decimal value 328. (b) Latin small letter A with acute, \acute{a} , with decimal value 225. (c) Greek capital letter Esh, Σ , with decimal value 425. Accordingly, the 10-bit binary values related to each CE are shown below of them.

8.2. Obscuring CEs into the longitudinal component

In subsection 3.2.1, we explained the vector behavior of an EM field $\mathbf{E}=(\mathbf{E}_x,\mathbf{E}_y,\mathbf{E}_z)$ in the focal area. In subsection 3.2.2, we described a method to obscure data into a longitudinal component of a highly focused beam. We rewrite Eq. (3.2-8) as follows:

$$\mathbf{E}_z(x, y, 0) = \text{FT}_{\lambda f} \left[\frac{\mathbf{E}_{\infty z}}{\cos \theta} \right] = \text{FT}_{\lambda f} \left[(\mathbf{E}_{ix} \cos \varphi + \mathbf{E}_{iy} \sin \varphi) \frac{\sin \theta}{\sqrt{\cos \theta}} \right]. \quad (8.1)$$

On the one hand, the longitudinal component of the focused field is connected to the transverse components of the input beam, according to Eq. (8.1). On the other hand, the transverse components of the input electric field are related to each other based on the state of the input polarization. Hence, by manipulating the state of the polarization and synthesizing the intensity pattern of the input beam, the vector components of the focused EM field alter accordingly. Here, we consider an input beam with spiral polarization. When the input field is spirally polarized, the transverse components are related by means of

$$\mathbf{E}_{ix} = -\mathbf{E}_{iy} \tan(\varphi + \omega), \quad (8.2)$$

where ω is a constant angle to be tuned. By substituting Eq. (8.2) into Eq. (8.1), the transverse components of the input field are obtained as follows:

$$\mathbf{E}_{ix} = \frac{\sqrt{\cos \theta}}{\sin \theta} \psi_x \text{FT}^{-1}[\mathbf{E}_z], \quad \psi_x = \frac{1}{\cos \varphi - \sin \varphi \cot(\varphi + \omega)} \quad (8.3)$$

$$\mathbf{E}_{iy} = \frac{\sqrt{\cos \theta}}{\sin \theta} \psi_y \text{FT}^{-1}[\mathbf{E}_z], \quad \psi_y = \frac{1}{\sin \varphi - \cos \varphi \tan(\varphi + \omega)}. \quad (8.4)$$

Depending on ω different polarization states across the beam section can be obtained, ranging from azimuthal (when $\omega=0$) to radial (when $\omega=\pi/2$) [234]. Since the azimuthal polarization provides a purely transverse focused field, $\omega=0$ is not our interest in this communication.

Since \mathbf{E}_z is embedded by \mathbf{E}_x and \mathbf{E}_y , we encode CEs in the inverse Fourier transform of the z-component. Subsequently, $E_0^e = \left(\sqrt{\cos \theta} / \sin \theta \right) \text{CE}$, where $\text{FT}^{-1}[\mathbf{E}_z] = \text{CE}$. So, by substituting Eqs. (8.3) and (8.4) into Eq. (3.2-8), the encoded vector components of the focused electric field (denoted by uppercase e) are obtained as follows:

$$\mathbf{E}_x^e = \text{FT}_{\lambda_f} \left[\frac{E_0^e}{\sqrt{\cos \theta}} \left(\psi_x (\sin^2 \varphi + \cos^2 \varphi \cos \theta) + \psi_y \sin \varphi \cos \varphi (\cos \theta - 1) \right) \right], \quad (8.5)$$

$$\mathbf{E}_y^e = \text{FT}_{\lambda_f} \left[\frac{E_0^e}{\sqrt{\cos \theta}} \left(\psi_x \sin \varphi \cos \varphi (\cos \theta - 1) + \psi_y (\sin^2 \varphi \cos \theta + \cos^2 \varphi) \right) \right], \quad (8.6)$$

$$\mathbf{E}_z^e = \text{FT}_{\lambda_f} \left[\frac{E_0^e}{\sqrt{\cos \theta}} \sin \theta \right] = \text{FT}_{\lambda_f} [\text{CE}]. \quad (8.7)$$

Note that there are no singularities in Eqs. (8.5) and (8.6) due to the specific design of CEs.

Accordingly, the intensity pattern of the encoded transverse components depends on the physical properties of the focusing system (θ), the intensity pattern (the design of CEs), and the angle ω . As a result, manipulating the longitudinal component of a highly focused EM field causes different intensity patterns and polarization vectors of the transverse components of the focused field.

Subsequently, to decode the original data, we need to obtain the longitudinal component at the focal plane according to Eq. (8.7). One possible method to obtain \mathbf{E}_z was introduced in section 6. Nevertheless, the algorithm proposed in section 6 or the other method based on a phase retrieval algorithm demands recording the intensity pattern of the electric field at different planes that can be the pair of the object and focal plane or a couple of at least two planes through the propagation path of the beam. Since we synthesize the optical beam (CEs) at the entrance pupil of a microscope objective, we use CNN as a supervised machine learning algorithm to classify and recover the obscured CEs by introducing PMIs.

8.3. Polarimetric mapping images and CNN model

Here we present an alternative algorithm to retrieve the CEs or decode character codes at the focal plane using polarimetric information. The proposed algorithm demonstrates that recording Stokes images at the focal plane is sufficient input into CNN to classify and retrieve the encoded character codes. The training dataset was obtained as follows:

- i. To provide 1024 CEs to encode all 10-bit character codes with decimal values ranging from 0 to 1023. Note that each CE encodes just one character code.
- ii. To calculate the encoded transverse components of the focused EM field using Eqs. (8.5) and (8.6) for each CE. Moreover, we obtained the other Stokes images using Jones matrix formalism (see subsection 3.3).

- iii. To compress the numerical Stokes images into a multidimensional array image named PMI corresponding with each CE. In the present works, PMIs consist of six channels comprising the 6 Stokes images as $I_{0,0}$, $I_{0,90}$, $I_{0,45}$, $I_{0,135}$, $I_{90,45}$, and $I_{90,135}$, respectively. Hence, 1024 PMIs were obtained corresponding with all CEs or 10-bit character codes.
- iv. To classify and label the PMIs from 0 to 1023 by applying a CNN model. Moreover, the number of the training dataset was increased by adding Gaussian noises to each polarimetric image and rescaling images to provide 8 PIMs for each character code. Particularly, we provided 1024×8 PIMs with 50×50×6 sizes, which 20% of them were randomly selected as a test dataset, while the other 80% were used as the training dataset.

We repeated these steps to obtain two different types of training datasets regarding two optical systems named A and B with differently polarized input beams. The numerical training dataset corresponding with optical systems A and B were obtained by substituting $\omega=\pi/8$ and $\omega=\pi/2$ into Eqs. (8.5) and (8.6), respectively. So, the machine was trained separately for optical systems A and B. The total numerical dataset is 8192, and 1639 of them were selected randomly as test datasets, and the rest was used to train the machine (6553 images).

Figure. (8.3) demonstrates the configuration of a PMI. The simulation parameters to obtain the training dataset are based on the physical properties of the used experimental tools. These details were explained in subsections 6.1 and 6.2. We implemented CNN using python 3.7 and TensorFlow 2.1, and a Laptop with GPU NVIDIA GeForce MX450.

The applied CNN model is a sequential model that is summarized in Fig. (8.4). The model consists of three convolutional layers with 32, 64, and 128 filter sizes and a kernel size of 3, accompanied by the hyperbolic tangent activation function. Moreover, batch normalization and average pooling layers are applied after each convolutional layer. The feature map obtained by different layers is flattened into one-dimension 2048 arrays as an imaging outcome. The image outcome is connected to 1843 neurons using a dense layer accompanied by the sigmoid activation function. Then, 25% of connected neurons are removed by a drop-out layer. Finally, the last dense layer provides 1024 probability distributions ranging from 0 to 1 applying the softmax activation function, which is used to label 1024 character codes.

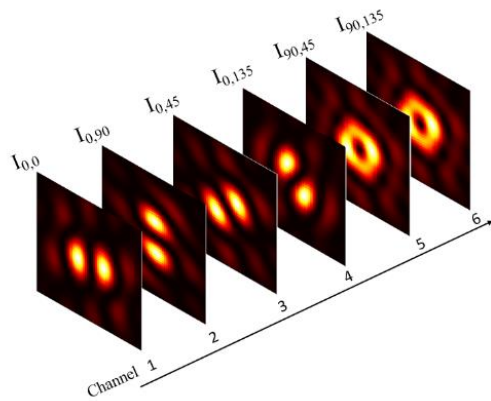


Fig. 8.3. An example of a PMI with a height and width of 50 pixels and 6 channels. These images are used as the inputs of the CNN model.

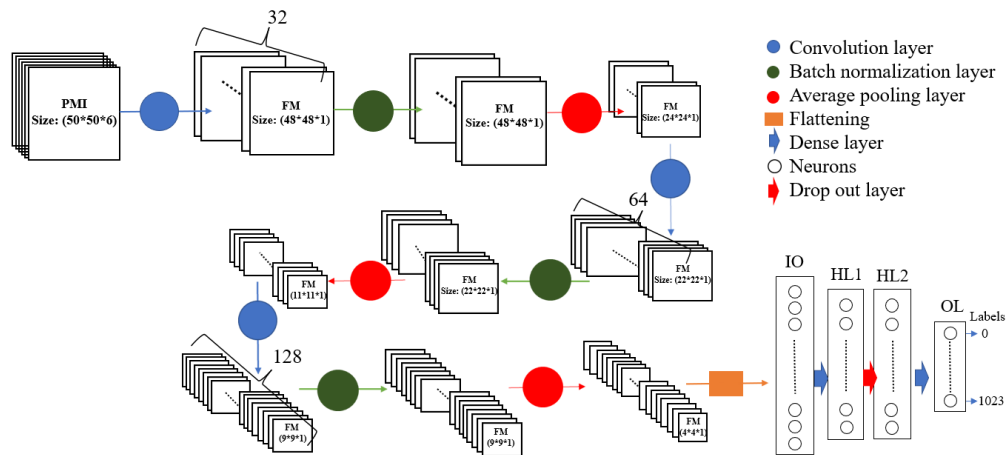


Fig. 8.4. CNN model. PMI, FM, IO, HL, and OL stand for polarimetric mapping image, feature-map, image-outcome, hidden layer, and output layer, respectively.

To compile the model, ‘rmsprop’, ‘sparse_categorical_crossentropy’, and ‘accuracy’ have been used as optimizer, loss, and metrics, respectively. Furthermore, the model was fitted with 30 and 40 epochs for optical systems A and B, respectively.

The obtained accuracy and loss values are shown in Table (8.1) for optical systems A and B. The obtained scores prove that the machine successfully classifies 1024 character codes using PMIs. Moreover, the class labels of randomly selected test datasets are predicted with high precision.

Table. 8.1. Network accuracy and loss

	Accuracy		Loss
System A ($\omega = \pi/8$)	Training dataset	0.997	0.011
	Test dataset	0.967	
	Experiment	0.901	
System B ($\omega = \pi/2$)	Training dataset	0.992	0.028
	Test dataset	0.925	
	Experiment	0.921	

8.4. Optical implementation and results

The sketch of the experimental setup is shown in Fig. (8.5). Since the optical systems A and B are identical, we display both in one illustration. The difference between the two optical systems is related to providing different spirally polarized input beams at the entrance pupil of microscope objective

MO1. The orientation of the fast axis of vortex retarder VR with respect to the axis of linear polarizer LP2 defines the parameter ω in Eqs. (8.3) and (8.4), indicated in the red rectangle, up and down of the common part of the optical setup A and B, respectively.

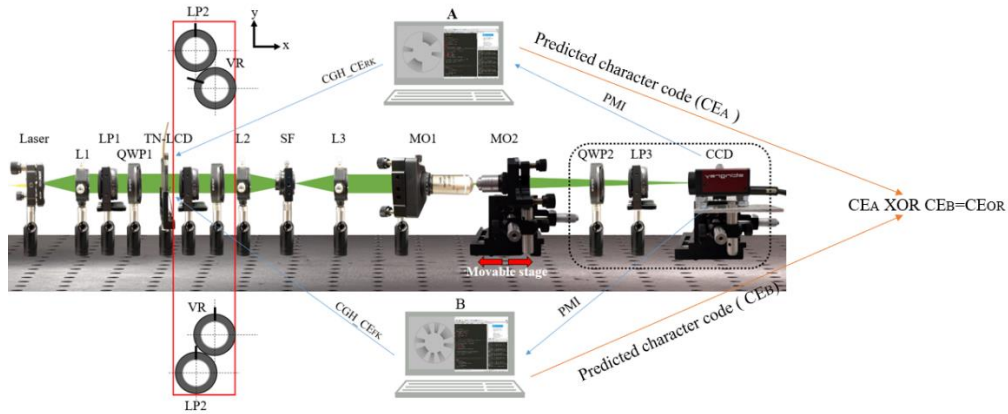


Fig. 8.5. The experimental setup. L, LP, QWP, TNLCD, VR, SF, MO, and CCD present lens, linear polarizer, quarter-wave plate, twisted nematic liquid crystal display, vortex retarder, spatial filter, microscope objective, and charge-coupled device. Figure adapted from [201] under a Creative Commons By 4.0 license.

The optical elements and the operation of the experimental setup were explained in detail in subsection 6.1. In optical setup A, the fast axis of VR was rotated 157.5° , while the polarizer axis of LP2 was rotated 90° with respect to the x-axis to polarize the encoded beam spirally ($\omega = \pi/8$). In optical setup B, the fast axis of VR and the polarizer axis of LP2 were oriented 90° concerning the x-axis to polarize the encoded beam radially ($\omega = \pi/2$). By moving precisely MO2 on the optical axis, forward and backward to MO1, we could practically find the back focal plane of MO1 or at least the nearest accessible plane using the movable stage. Once the focal plane was imaged on the sensor plane of the CCD, the position of MO2 and CCD camera remained constant during the whole experimental process.

We randomly selected 210 character codes equal to 20% of all 10-bit character codes to implement the experiment. Subsequently, their CEs and E_0^e were calculated, and corresponding CGHs were obtained and loaded on the LCD.

Figure. (8.6) demonstrates three examples of CEs (the first row), E_0^e (the second row), and CGHs (the third row) regarding character codes \check{n} , \acute{a} , and Σ , respectively. For each optical system (A and B), $210 \times 2 \times 6$ images have been recorded independently. Note that due to the instability of the laser intensity and the possible imposed noises caused by the CCD camera, recording 6 Stokes images has been repeated twice for each CGH. Then, experimentally obtained Stokes images were cropped and compressed into an image with $50 \times 50 \times 6$ sizes.

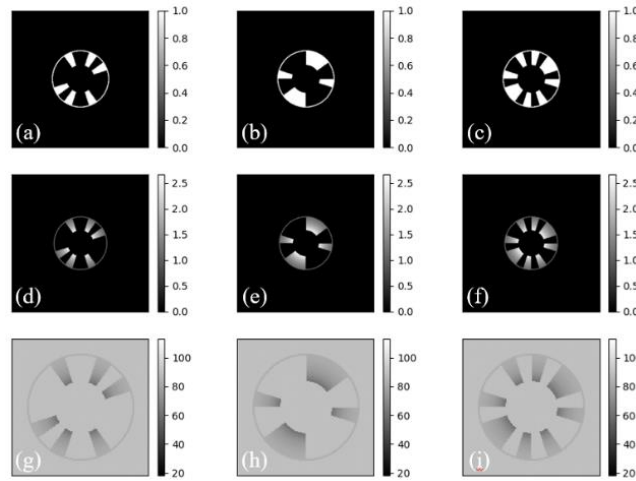


Fig.8.6. The first row shows CEs corresponding with character codes (a) \check{n} , (b) \acute{a} , and (c) Σ . The second row shows E_0^e 's corresponding with character codes (d) \check{n} , (e) \acute{a} , and (f) Σ . The third row indicates CGHs corresponding with character codes (g) \check{n} , (h) \acute{a} , and (i) Σ . Note that CGHs have twice the size of the CEs, because of DPH Arrizón's approach.

Particularly, 410 PMIs were recorded for each optical system to be predicted by the CNN model. Figure. (8.7) indicates the numerical and experimental Stokes images regarding character code \acute{a} in two optical systems A (separated by the red dashed line) and B (separated by the blue dashed line). In contrast, Figure. (8.8) shows the Stokes images in regard to two character codes \acute{a} (separated by the red dashed line) and Σ (separated by the blue dashed line) in optical system A.

Interestingly, the obtained accuracies of the predicted class labels by the machine are 0.901 and 0.921 for optical systems A and B, respectively, as

shown in Table. (8.1). The results show an excellent agreement between the numerical and experimental results.

Generally speaking, we consider two optical systems (A and B), which are differentiated by providing different spirally polarized input beams. Each CGH corresponds to a cipher-share character code that can be transferred between a sender and a couple of receivers with individual optical systems. On one side, each cipher-share character code can be decoded by authorized receivers that access the proper optical system. On the other side, none of the receivers have access to the original data. The original data can be decoded by applying the bitwise XOR operation on the cipher-shared character codes, as sketched in Fig. (8.5).

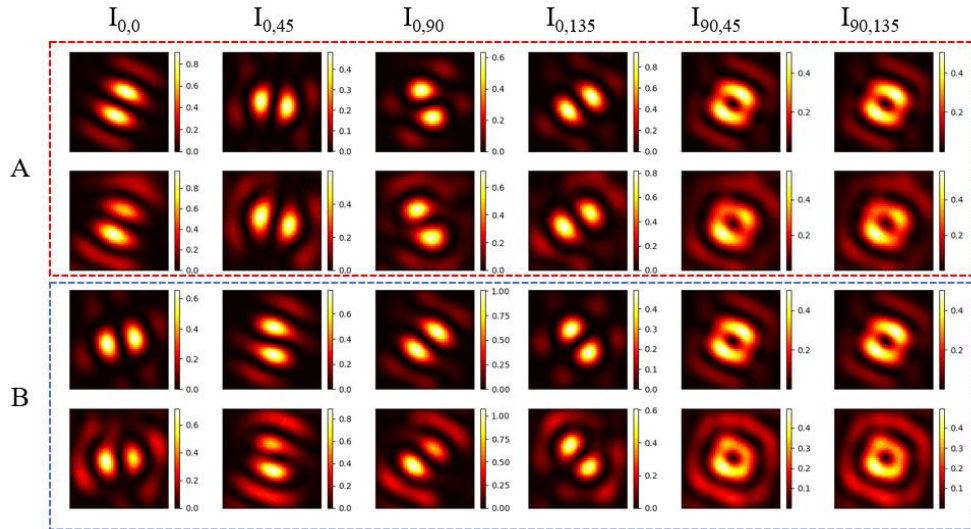


Fig. 8.7. The first and second rows of the red dashed rectangle indicate the numerically and practically obtained Stokes images corresponding with character code \acute{a} in optical system A, respectively. The first and second rows of the blue dashed rectangle indicate the numerically and practically obtained Stokes images corresponding with code \acute{a} in optical system B, respectively.

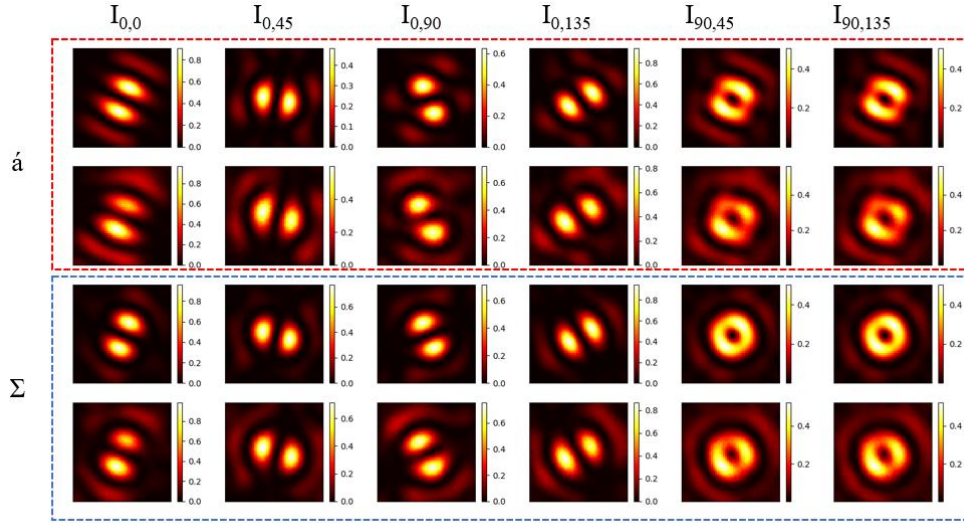


Fig. 8.8. The first and second rows of the dashed red rectangle indicate the numerically and practically obtained Stokes images corresponding with character code \acute{a} , respectively. The first and second rows of the blue dashed rectangle indicate the numerically and practically obtained Stokes images corresponding with character code Σ .

8.5. Analyzing the operation of the system

We previously claimed that the training dataset depends on the design of CEs. In subsection 8.5.1, we evaluate the recognition ability of the CNN model for recovering the character code with the PMIs that are obtained from three CEs with different designs. In subsection 8.5.2, we evaluate the channels of PMIs and their effect on recovering the character codes.

8.5.1 Design of CEs

Radii R and r can be considered as design variables of CEs. The training dataset might be completely different by changing these values. In case the codes to be optically analyzed use other radii values, it is very likely that recognition will not be possible. Figures (8.9) and (8.10) demonstrate synthetically produced PMIs for code 328 (\check{n}) using different values R and r in systems A and B, respectively.

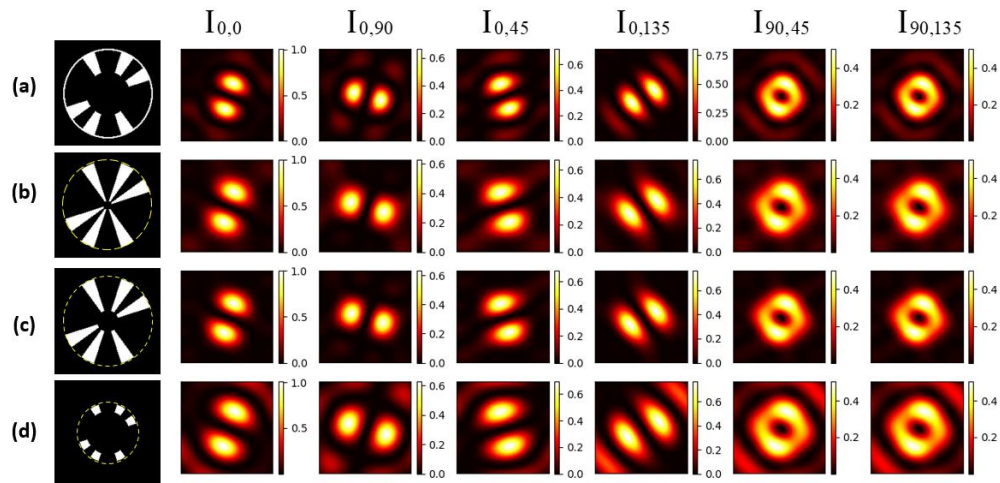


Fig. 8.9. CE corresponding to code 328 in system A with (a) $R = 3.75$ mm and $r = 1.8$ mm, (b) $R = 3.75$ mm and $r = 0.36$ mm, (c) $R = 3.75$ mm and $r = 1.8$ mm, and (d) $R = 2.5$ mm and $r = 1.8$ mm.

Table. (8.2) indicates the predicted class labels corresponding with code 328 using the CNN model regarding the four CEs depicted in Figs. (8.9) and (8.10). The results show that the model can predict the correct class label only if the PMIs obtained from the correct physical properties of CEs.

Table. 8.2. Predicted class labels by the CNN model regarding different CE designs

CEs	Predicted class label by machine (System A)	Predicted class label by machine (System B)
CE (a): code 328	328 Correct	328 Correct
CE (b): code 328	421 Wrong	437 Wrong
CE (c): code 328	420 Wrong	724 Wrong
CE (d): code 328	980 Wrong	724 Wrong

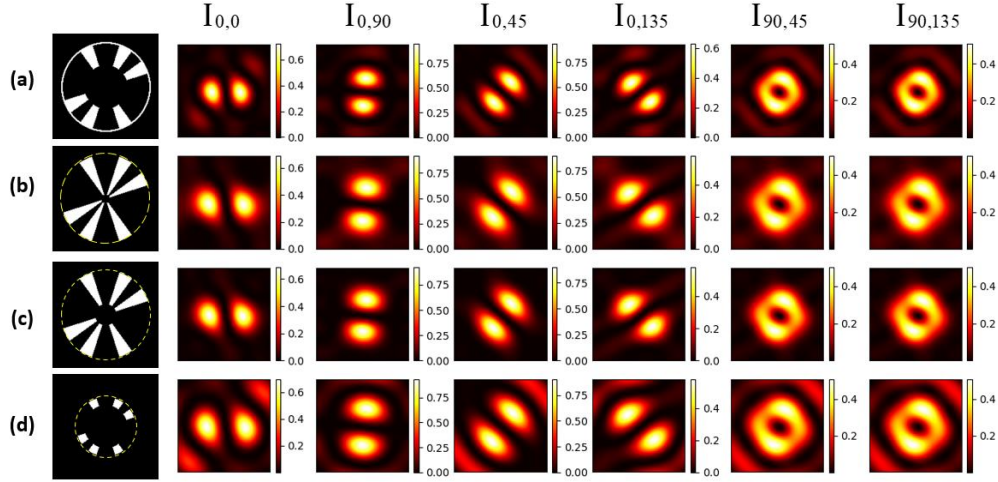


Fig. 8.10. CE corresponding to code 328 in system B with (a) $R = 3.75$ mm and $r = 1.8$ mm, (b) $R = 3.75$ mm and $r = 0.36$ mm, (c) $R = 3.75$ mm and $r = 1.8$ mm, and (d) $R = 2.5$ mm and $r = 1.8$ mm.

8.5.2. PMIs

In this subsection, we consider two analyses. The first one evaluates the requirement of the order of channels in the configuration of PMIs. The second analysis investigates the possibility of recovering codes while one channel of PMIs is missed.

As shown in Fig. (8.3), the configuration of PMIs used for training the machine consists of 6 channels in this order: $I_{0,0}$, $I_{0,90}$, $I_{0,45}$, $I_{0,135}$, $I_{90,45}$, and $I_{90,135}$. We provided a new test dataset of PMIs obtained from 500 codes (total code is 1024) with different orders of channels to be predicted (or recognized) by the machine. The results corresponding to this analysis are shown in Table. (8.3), which demonstrates that if the order of channels is not the same as the order of channels used for training the machine, the machine is not able to predict the corresponding codes.

Table. 8.3. Test accuracy for a different order of channels

Order of channels	System A(spiral)	System B(radial)
$I_{0,90}, I_{0,0}, I_{0,45}, I_{0,135}, I_{90,45}, I_{90,135}$	0.008	0.006
$I_{0,90}, I_{0,0}, I_{0,135}, I_{0,45}, I_{90,45}, I_{90,135}$	0.002	0.022
$I_{0,45}, I_{0,90}, I_{0,0}, I_{0,135}, I_{90,45}, I_{90,135}$	0.132	0.11
$I_{0,135}, I_{0,45}, I_{0,90}, I_{0,0}, I_{90,45}, I_{90,135}$	0.008	0.006

We provided a new test dataset for the second analysis by considering one of the six channels is missed and replaced by random noise. For doing this analysis, we considered 500 codes, and for each one, one of the channels was missed (see Fig. (8.11)). Note that since $I_{90,45}$ and $I_{90,135}$ are very similar, we just consider that knowing one of them provides the other one. An example of a test dataset corresponding to code 328 in system B is shown in Fig. (8.11). The obtained accuracies corresponding with the test dataset are shown in Table. (8.4).

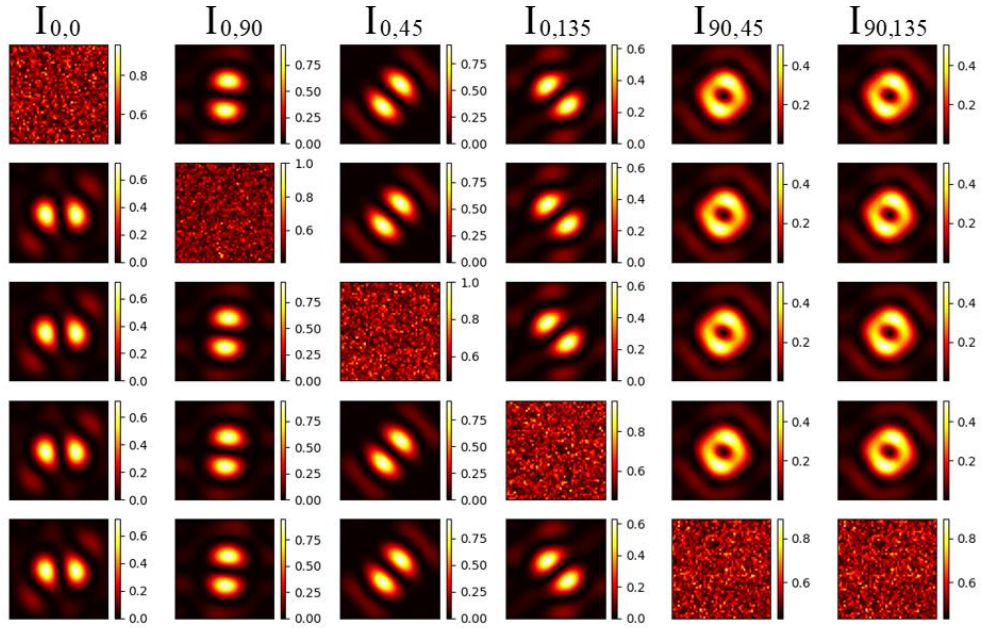


Fig. 8.11. Test dataset corresponding with code 328 in System B with one missed channel. The missed channel is replaced with Gaussian noise with a variance of 0.3.

The results justify that the four channels $I_{0,0}$, $I_{0,90}$, $I_{0,45}$, and $I_{0,135}$ must be provided in order to recover the code. Since the system is illuminated with non-uniform linear polarized light (radial and spiral), the contribution of channels $I_{90,45}$ and $I_{90,135}$ is less critical for the recognition process. Interestingly, if we simultaneously remove the information from the $I_{90,45}$ and $I_{90,135}$ channels, the accuracy value depends on the polarization of the illuminating beam. In particular, when using radial polarization, it is enough to use the channel set:

$I_{0,0}$, $I_{0,90}$, $I_{0,45}$, $I_{0,135}$ to achieve a high accuracy value. However, this is no longer true for spiral polarization. As a result, to avoid false recognition, it is required not to ignore any channel.

Table. 8.4. The accuracies of test dataset corresponding to missed channels.

Missed channel	System A(spiral)	System B(radial)
$I_{0,0}$	0.012	0.014
$I_{0,90}$	0.012	0.012
$I_{0,45}$	0.026	0.038
$I_{0,135}$	0.008	0.056
$I_{90,45}$ and $I_{90,135}$	0.436	0.96

8.6. Robustness of the system against noise and occlusion attack

In this subsection, we evaluate the recognition ability of codes under noise and occlusion attacks.

8.6.1 Noise

Noise can be added to the beam during the propagation and recording of the optical information. In this regard, we have already considered this issue by adding Gaussian noise with a variance ranging from 0 to 0.25 to each channel of every PMI. Figure (8.12) demonstrates an example of a training dataset considering Gaussian noise. Note that for each character code (CE), we considered 8 PMIs in which five of them correspond with additive Gaussian noise, and the other ones are related to rescaling the original PMIs.

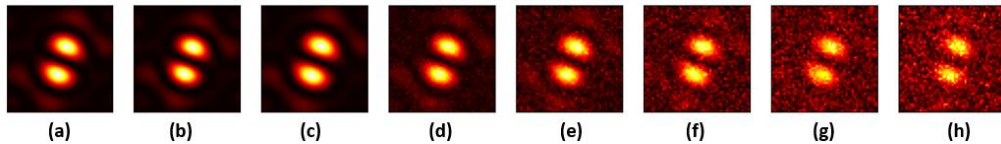


Fig. 8.12. The first channel of the 8 PMIs for code 328 calculated for polarization case A. (a) original PMI, (b) zoomed with scale factor = 0.95, (c) zoomed with scale factor = 1.05; PMIs degraded with additive Gaussian noise with a variance of (d) 0.05 (e) 0.1 (f) 0.15 (g) 0.2 (h) 0.25. Note that all noises are added to each channel, but we just show the first channel of each PMI for illustration purposes.

As a result, the recognition ability of the neural network is robust against a severe amount of noise. Taking into account that the other types of noise can be considered in the training dataset.

8.6.2. Occlusion attack

Information occlusion or losing information is one of the most common attacks in optical cryptosystems. In order to evaluate the robustness of the system against occlusion attacks, we produced three 500-character PMI test sets. Every set contains no information in continuous areas equivalent to 6%, 10%, and 16% of the total pixels. Figure (8.13) shows the first channel of the synthesized occluded PMIs with 5 different positions corresponding with codes 0, 100, 200, 300, and 400 obtained for system B.

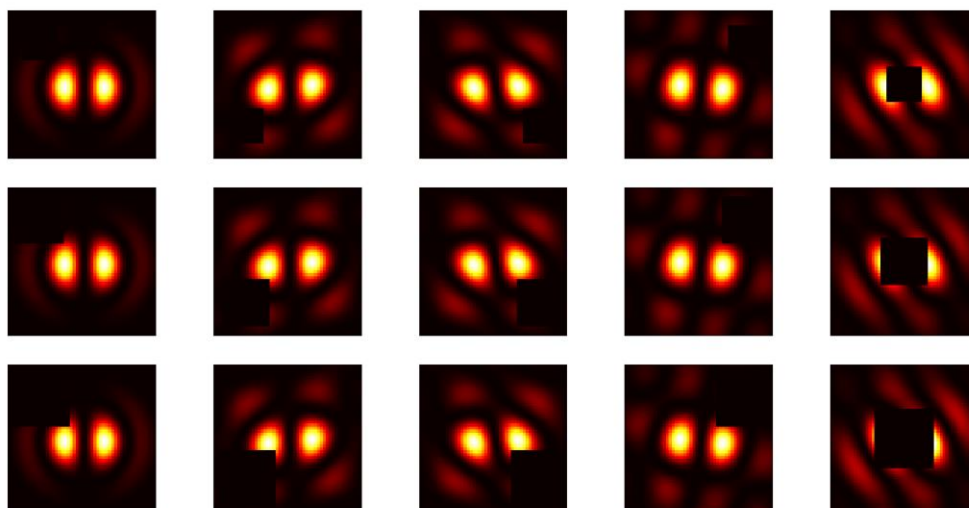


Fig. 8.13. The first row demonstrates the first channel of PMIs regarding codes 0, 100, 200, 300, and 400, respectively, in which 6% of their pixels are occluded with 5 different positions. The second and third rows contain the same information, but 10% and 16% of their pixels are occluded, respectively. Note, PMIs are related to radial polarization (System B).

Table. (8.5) indicates the corresponding accuracies. The results indicate that the model is robust against the occlusion attack below 10% loss of information. Nevertheless, the accuracy decreases rapidly for more than 10% of occluded information. This can be explained by the specific design of the CNN model. We designed the model for pattern recognition and classification purposes to be efficient for a visual encryption system.

Table. 8.5. Test accuracy for PMIs containing random information. Test dataset: 500 codes

Test set	System A	System B
Area occluded: 6%	0.974	0.976
Area occluded: 10%	0.980	0.974
Area occluded: 16%	0.820	0.810

A possible solution for avoiding this attack for higher occluded information is to train the machine with a large set of occluded PMIs. This methodology is equivalent to the proposed design of PMIs to avoid noise.

To sum up, we designed a successful optical setup and a coding procedure able to implement visual encryption. Some of the design variables can be modified in order to deploy alternative systems with similar performance:

1. The characters were encoded assuming the longitudinal component E_z was described by the Fourier transform of CE. Alternative implementations of \mathbf{E} can also be considered, provided the network is trained accordingly.
2. The system has been demonstrated using a high NA microscope objective and spiral polarization. However, low NA lenses or other polarizations might be used as well.
3. The character set used was limited to 1024 codes, but the method can be easily scaled to include any arbitrary binary set.
4. Here, we transfer CGHs between a sender and a couple of receivers with individual optical systems. However, the polarimetric images can be transferred accordingly. Regarding the obtained results from analyzing the PMIs, the CNN will provide a correct answer only if the complete group of polarimetric images is available. Thereby, the number of recipients can be increased up to twelve.
5. Since the channels $I_{0,0}$, $I_{0,90}$, $I_{0,45}$, and $I_{0,135}$ play the main role in recovering character codes, one of the channels can be encrypted by the photon counting model (see subsection 3.2.2.2). In other words, new training datasets (PMIs) can be obtained considering a photon-limited channel for authentication purposes.

9. Polarimetric identification of 3D-printed nanoparticle encoded optical codes

This section describes a method to obtain unique optical codes using 3D physical keys. 3D physical keys are obtained by a low-cost 3D printer using low-cost materials sensitive to the state of polarization of EM fields. Each 3D physical key can be used for authentication purposes.

As previously explained, optical authentication can arguably be considered as a well-established research field (see [235] for a comprehensive tutorial on this topic). In particular, photonics devices produced with metamaterials play a key role in optical security technology [236]. Besides, the polarimetric signature is one of the properties that has been used to authenticate and classify samples [79-81]. Very likely, providing the samples sensitive to the state of polarization of optical beams requires advanced technologies using specific materials. In this regard, the number of samples produced might be highly restrictive due to the production costs associated with the used technology.

The term 3D printing can be considered as a synonym for additive manufacturing [237-244]. Additive manufacturing is a process that builds parts layer by layer by depositing material based on digital 3D design data. This process is able to join or solidify some materials through a computer-controlled system to fabricate 3D physical models. Since the mechanical properties of 3D printed samples depend on different variables, many publications have been dedicated to observing the effects of these variables. These variables mainly include the composition of powder, temperature during manufacturing, binder, binder saturation level, building orientation, layer thickness, filling pattern, type of filaments, etc. [239]. In general, additive manufacturing techniques results in anisotropic mechanical properties that have been investigated by measuring fracture strength, tension, stress, etc. [240]. Those measurements or tests that usually cause damaging the samples proved that the microstructure and the mechanical properties of each 3D production are directly dependent on the many variables during additive manufacturing processes.

Thanks to optics, in this work, we used a contactless approach without damaging the samples to show, on the one hand, the microstructure of 3D printed samples depends on the 3D printing parameters. On the other hand, the microstructure of 3D printed samples filled with metallic powder is not predictable, which shows the possibility of considering 3D printed samples as Physical Unclonable Functions (PUFs) [245, 246]. Therefore, a 3D printed

sample filled with metallic powder can be used as a physical key to obtaining synthesized optical codes for security authentication.

We used a 3D printer to produce different types of structures using several materials and with different types of filling patterns. In particular, 3D printing allowed us to create a relatively large number of samples with an excellent degree of freedom to be categorized into different classes. In the experiments, we discuss the classification of a single class of codes and how a 3D printed sample can be distinguished from a group of samples to be rejected. Experimental results and theoretical analysis verify the feasibility of the proposed approach. The samples in the experiments are created using commercially accessible materials and a low-cost 3D printer. In particular, we used polylactic acid (PLA), which is a particular type of thermoplastic filament used in 3D printing, combined with metallic powder. Then, we obtained synthesized optical codes which are comparable with polarimetric signatures generated by samples made of metallic nanoparticles or thin-film structures.

9.1. Design of 3D printed samples

Here we used an inexpensive Anet A8 DIY 3D printer accompanied by PLA filaments filled with metallic powder: Aluminum, Brass, and Copper (AptoFun wire, produced by Aptotec UG, Tübingen, Germany). In this work, we suggest attaching encoded data such as QR codes on the flat surface of each 3D printed sample and using its coarse surface for verification. Since the production of each 3D sample required a set of design variables such as the filling pattern, the bed and nozzle temperatures, the filling pattern density, the diameter of the filaments, and the 3D printer extrusion type, the manufacturing process provides an excellent degree of freedom to produce different samples, in which each one can be classified as different categories.

We produced samples with four different filling patterns: Hilbert, Archimedean, Octagram, and Rectilinear, which are configurable by 3D printers, while the other 3D printing parameters remained identical for all produced samples.

Figure (9.1) shows four produced samples made of PLA-Aluminum with different filling algorithms. As shown in Fig. (9.1), the coarse surfaces of printed samples have a random irregular look, concentric circles, a Malta cross look, and parallel lines for the Hilbert, Archimedean, Octagram, and Rectilinear filling algorithms, respectively. Note that the back surface of all produced samples is flat without specific differences, so we did not show these surfaces.

A description of the printing algorithms used can be found elsewhere. See, for instance, [247].

We provided 12 different classes of samples with a combination of the three different PLA filaments and the four different filling algorithms. We produced 19 samples with a size of $20 \times 20 \times 2 \text{ mm}^3$ in order to implement the polarimetric signature experimentally. Table (9.1) shows the number of printed samples. Note that, the other printing variables have been kept constant for all the samples with the following details: Fill pattern density: 5%; nozzle temperature: $190 \text{ }^\circ\text{C}$; bed temperature: $50 \text{ }^\circ\text{C}$; filament diameter: 1.75 mm; layer height: 0.3 mm. Taking into account that changing printing parameters can produce a different class of samples.

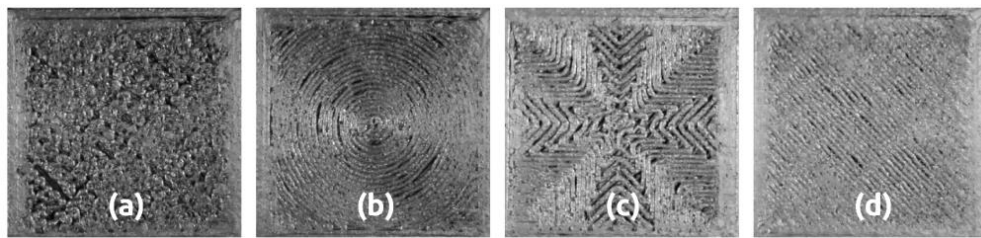


Fig. 9.1. Four examples of 3D printed samples made of PLA- Aluminum with different filling algorithms: (a) Hilbert, (b) Archimedean, (c) Octagram, and (d) Rectilinear. The size of each sample is $20 \times 20 \times 2 \text{ mm}^3$. Figure from [248] under a Creative Commons By 4.0 license.

Using a confocal microscope, we were able to take images of the surface topography in order to provide information on the characterization of the metallic powder (aluminum, copper, and brass) solidified in the PLA wire. Note that the manufacturer of the filaments does not provide any information on the characteristics of the metallic powder used in the fabrication of the PLA filament. The size of the topographical images is 770×576 pixels corresponding to an area of $85 \mu\text{m} \times 64 \mu\text{m}$ with a pixel depth of 8 bits, which were obtained using a Sensorfar PL μ 200 microscope with a 150x NA=0.95 Nikon objective and the resolution depth of $25 \mu\text{m}$ with elevation values ranging from 43 to 255. Note that the topography of the samples shown in Fig. (9.2a) to (9.2c) is irregular and does not follow any pattern.

Table. 9.1. Produced samples categorized into 12 classes. The numbers indicate the number of produced samples. The abbreviations distinguish each class label.

	Archimedian	Hilbert	Rectilinear	Octagram
PLA-Aluminum	2 (AA)	5 (AH)	2 (AL)	2 (AO)
PLA-Brass	1 (BA)	1 (BH)	1 (BL)	1 (BO)
PLA-Copper	1 (CA)	1 (CH)	1 (CL)	1 (CO)

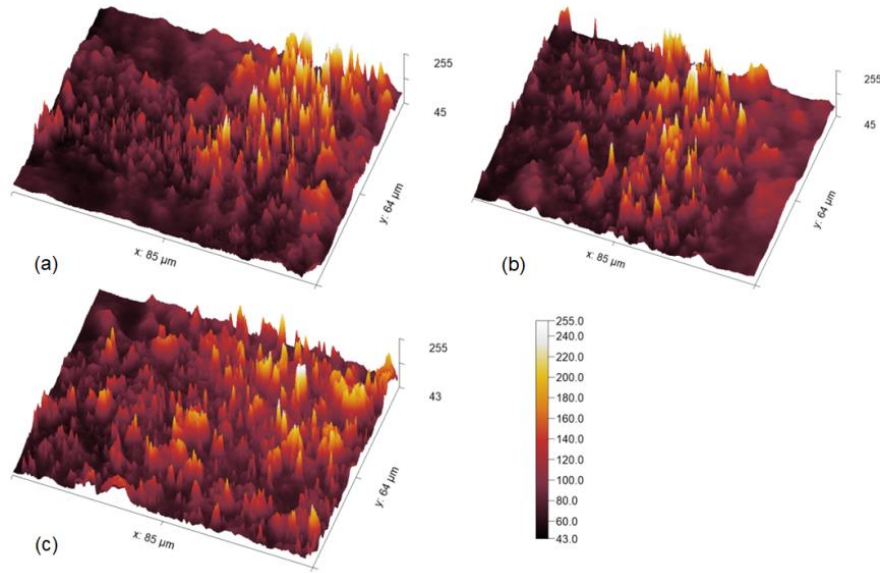


Fig. 9. 2. The confocal microscope images obtained for the Hilbert filling algorithm corresponding with PLA-: (a) Aluminum; (b) Brass (c) Copper. The size is $85 \times 64 \mu\text{m}^2$ and the peak-to-valley depth is $25 \mu\text{m}$ (elevation values range from 43 to 255). Figure from [248] under a Creative Commons By 4.0 license.

9.2. Experimental procedure: Polarimetric signature codes

The experimental setup is shown in Fig. (9.3), which has been designed to implement the polarimetric signature in order to obtain synthesized polarimetric codes from illuminating 3D printed samples, which are considered as 3D physical keys. Note that each 3D printed sample has two faces: one face has a flat surface proper for attaching the encoded data, and the other face, which has a coarse surface was used for the experiment.

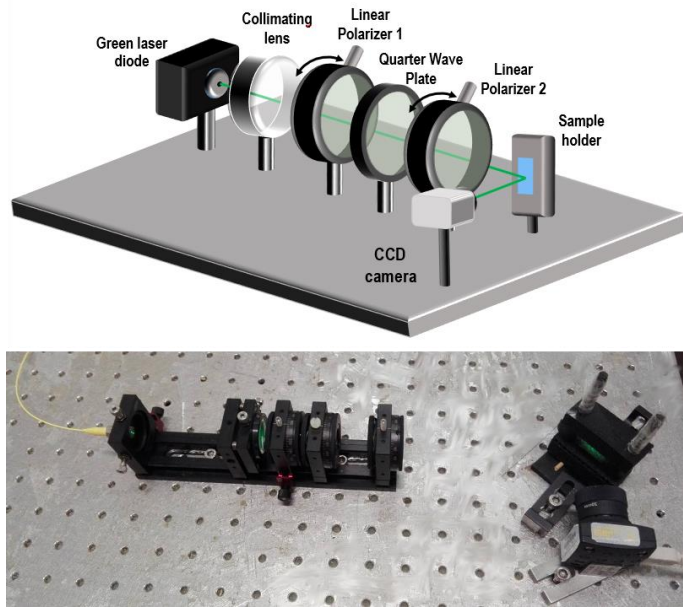


Fig. 9.3. The optical setup. Figure from [248] under a Creative Commons By 4.0 license.

A green laser diode ($\lambda=532$ nm) is placed at the back focal plane of the lens to provide a collimated coherent optical beam. Since the used laser source is linearly polarized, we used a linear polarizer followed by a quarter-wave plate in order to produce a circularly polarized beam. The second linear polarizer (Linear polarizer 2) is used to implement the polarimetric signature by means of rotating its polarizer axis. In other words, the optical beam passing through Linear polarizer 2 is linearly polarized with different directions of polarization. Moreover, we used a custom-made holder properly turned with respect to the optical axis to provide the incident angle of the incoming light at 55° and reflect the outgoing beam with the same angle forward to an 8-bit CCD camera, which is placed at a fixed distance. Since the beam is coherent and the surface of each sample is rough, the reflected beam forms a speckle pattern which is recorded by the CCD camera.

Each obtained speckle pattern is considered a polarimetric signature code corresponding with the orientation angle of the polarizer axis of Linear polarizer 2. The polarizer axis of Linear polarizer 2 has been oriented from 0 to 175° in steps of 5° . Moreover, for each orientation angle, ten speckle patterns were recorded continuously by the CCD camera. Hence, 360 speckle patterns were obtained for each sample corresponding with 36 orientation angles and 10 repeated measurements.

The strongest dependence of the reflected intensity as a function of the direction of polarization of the incident beam has been found by placing the samples at 55° with respect to the optical axis corresponding with the Brewster angle of the samples made of PLA (the refractive index of PLA is $n_d = 1.465$ [249]). Three examples of recorded speckle images corresponding to AA, BA, and CA samples (see Table (9.1) for nomenclature) are shown in Fig. (9.4).

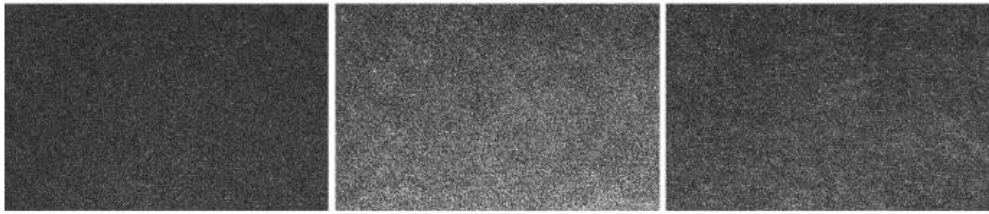


Fig. 9.4. Three examples of recorded speckle images corresponding with AA (left), BA (center), and CA (right). In the three cases, the second polarizer is set to 0° . Figure from [248] under a Creative Commons By 4.0 license.

In general, our total dataset consists of $36 \times 10 \times 19$ speckle patterns, which are corresponding to 36 orientation angles of the polarizer axis of Linear polarizer 2 (polarimetric signature), 10 times recording of each polarimetric signature, and 19 samples. In order to extract meaningful characteristics from each speckle pattern, we implemented statistical analysis, which is explained in the following subsection.

9.3. Statistical analysis: Feature extraction

In this subsection, we analyze statistically speckle patterns obtained optically. In the first step, we assess the histograms obtained from every speckle image, which demonstrate the intensity distribution of each speckle pattern. The histograms and cumulative histograms (normalized to the number of pixels) calculated from a speckle image for one sample of the 12 classes are displayed in Fig. (9.5). Since the direction of the second polarizer is set to 0° for all the depicted cases, the shape of histograms is partially or totally different regarding different filaments or/ and different filling algorithms. As a result, the intensity patterns of reflected beams have been altered based on the design variables.

Furthermore, we obtained the mean and standard deviation of each histogram to compare with a Gamma probability distribution. Interestingly, the shape of these curves (histograms) calculated from recorded images statistically are compatible with a Gamma Probability Distribution [250]:

$$P(g) = \left(\frac{n_0}{\bar{g}}\right)^{n_0} \frac{g^{n_0-1} \exp(-g n_0 / \bar{g})}{\Gamma(n_0)} ; n_0 = \left(\frac{\bar{g}}{\sigma}\right)^2, \quad (9.1)$$

where g is the corresponding gray level, and \bar{g} and σ are the mean and the standard deviation of the experimental recorded image; $\Gamma()$ stands for the Gamma function. We also displayed $P(g)$ in Fig. (9.5) (see dotted line curves, labeled with ‘(T)’ in the legend). Interestingly, the $P(g)$ distributions approximately reproduce the experimental histograms. This fact is confirmed when the cumulative histograms are analyzed (see the second row of Fig. (9.5)).

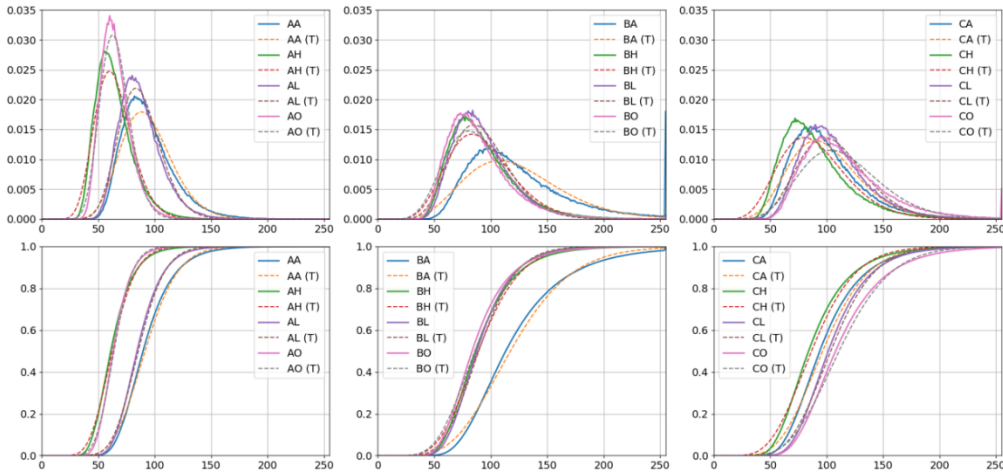


Fig. 9.5. The first row shows the Probability Density Function for one example of each class of printed sample (left: aluminum, center: brass, right: copper) at 0° of incident polarization direction as a function of gray level g . The corresponding theoretical estimation curve is labeled with (T), according to $P(g)$ [Eq. (9.1)]. The second row shows the corresponding cumulative histograms. Figure from [248] under a Creative Commons By 4.0 license.

As previously explained, the speckle characteristics of the reflected beam strongly depend on the direction of polarization of the incident light. This can

be explained based on the Fresnel formulae, in which p- and s- polarization depends on the angle of incidence and the refraction index of the sample material. Indeed, the presence of metallic powder with complex refractive indexes (aluminum: $n=0.938 + 6.420j$, brass: $0.568 + 2.589j$, and copper: $1.116 + 2.596j$ [249]) modifies slightly the refractive index of the PLA samples.

Moreover, the angle of incidence varies at each point of the surface due to the different topographical characteristics at the microscopic level (Fig. (9.2)), and thus, each sample can be considered unique.

Figure (9.6) compares the obtained probability distributions regarding three samples: {AH, BH, CH} while the orientation angles of Linear Polarizer 2 were placed at the following angles: $\{0^\circ, 20^\circ, 40^\circ, 60^\circ, 80^\circ\}$. These results prove that the shape of histograms depends on the direction of the fluctuation of the incoming EM field reaching the surface of 3D printed samples.

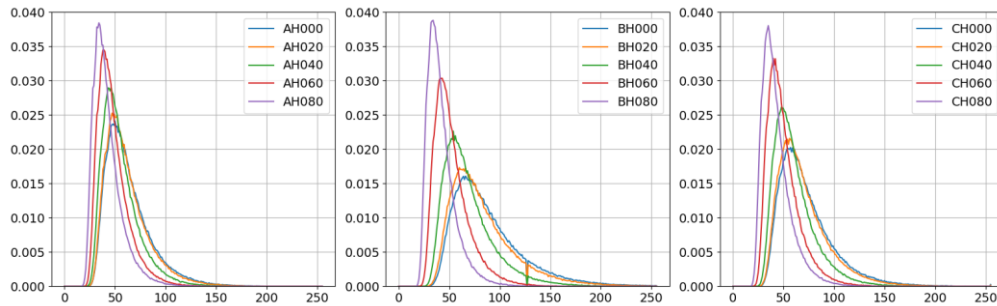


Fig. 9.6. The Probability Density Functions corresponding with AH sample (left), BH sample (center), CH sample (right) of printed codes for different directions of polarization as a function of gray level g . Figure from [248] under a Creative Commons By 4.0 license.

Hence, we identified each speckle pattern by means of the mean and the variance (see Eq. (9.1)) obtained from the corresponding histograms. These two features are used to define the feature vector for classification purposes.

Figure (9.7) indicates all polarimetric signature codes (speckle patterns) corresponding with 19 samples shown as data points in the feature space (variance versus the mean). The distribution of data points shows the complexity of the classification problem.

It is important to note that each data point that appears in Fig. (9.7) represents a particular feature vector (see subsection 3.5). This feature vector corresponds to a particular polarization measurement of a particular printed QR material and

printed architecture (design), and these data points are used to be classified by the one-class support vector machine (OC-SVM) classifier.

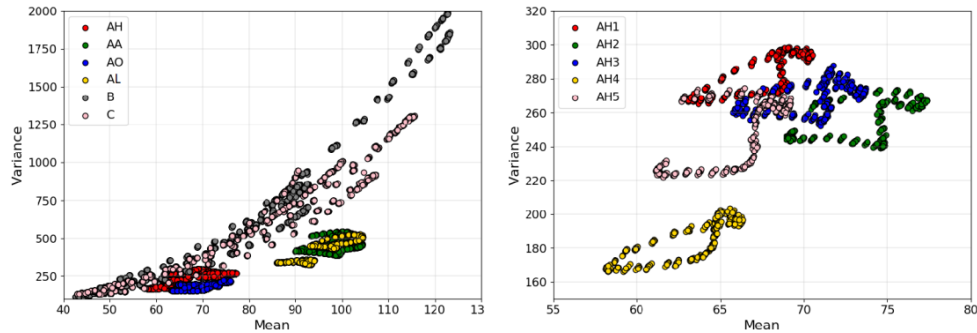


Fig. 9.7. The plot of the total dataset in feature coordinate (variance versus mean) corresponding with the experimental recorded speckle images is shown on the left side of the figure. Note that for the sake of clarity, the data corresponding to classes B and C are grouped. The right plot shows the distribution of data points in feature space corresponding with the samples belonging to class AH. Figure from [248] under a Creative Commons By 4.0 license.

9.4. Pattern classification

In subsection 9.1, we explained the process of providing 3D printed samples based on design variables such as the type of filling algorithm and filament. In subsection 9.2, the experimental process for obtaining unique speckle patterns has been described. In this subsection, we classify obtained speckle patterns into two main categories: the class of interest (or True class) and a class of no interest (or False class). Since the OC-SVM classifier is a type of binary classification, we used this machine learning algorithm to distinguish (classify) a group of optical codes as a class of interest from the other optical codes that belong to the class of no interest. The SVM machine learning algorithm with a brief mathematical description has been introduced in subsection 3.5.2.

One-class classification may be seen from two complementary perspectives: (a) from the anomaly detection and (b) from the target detection point of view. Anomaly detection is referred to the problem of detecting data and/or patterns that do not follow the expected behavior. We refer to them as the outlier data.

Target detection is applied to identify specific data of interest (target data). Classifying positive (target) cases in the absence of appropriately defined negative cases (outliers) has attracted more attention in the last few years [251-

253]. There is a diverse and rich field of one-class classification methodologies. The interested reader is referred to [254-256].

As explained in subsection 3.5.2, the SVM classifier aims to find the hyperplanes that separate the data from the origin with a maximal margin. One of the most important problems in pattern recognition is that the dataset may have a cardinality unbalance, defining a scenario where the number of data points of one of the classes is much lower than that of the other(s).

In our case, we are also dealing with an unbalanced problem due to the number of data points of interest being much lower than the total number of points in the dataset. Some strategies have been developed in general unbalanced classification scenarios to improve accuracy or gain insight into the specific aspects of the problem at hand [257, 258].

Here, we considered two different classification scenarios based on two different situations. In the first one, we considered the design variables such as the type of filling algorithm and the type of PLA-metal. All the physical samples made using the identical design variables are considered as part of the class of interest, as described in subsection 9.4.1. In this situation, we obtained different polarimetric signature codes depending on the design variable.

In the second scenario, just one physical sample of one particular combination of the material and the filling pattern is considered the class of interest, and the aim is to distinguish this from the other four (presumably) identical samples, as described in subsection 9.4.2. In this condition, we show that 3D printed samples might be considered as PUFs.

9.4.1. Classifying one group of identical 3D printed samples against the other different samples

In the first scenario, we intend to classify the 5 samples made of PLA-Aluminum with the Hilbert filling algorithm as validated samples. All the data points (speckle patterns or polarimetric signature codes) obtained from these 5 samples (AH1, AH2, AH3, AH4, and AH5) distributed in feature space (Fig. (9.7)) are grouped as the class of interest or True class. The OC-SVM classifier is designed to recognize these 5 samples as validated samples, whereas the machine should reject the other 14 samples. Note that the other 14 samples are made using different filling algorithms or/ and different materials (PLA- Brass and - Copper). The total data set for the class of interest as the combination of sample and polarization direction, based on the procedure detailed in subsection 9.2, is $360 \times 5 = 1800$ data points corresponding with 5 AH samples, in which 10 speckle patterns have been recorded from each one of the 36 different polarization directions (from 0 to 175°). Note that, Due to the instability of the

illuminating laser beam, for each orientation angle of Linear polarizer 2 (from 0 to 175°), we recorded 10 speckle patterns during a short time in order to enhance the recognition ability of the classifier.

To train the SVM classifier, we formed a matrix with a size of 900×2 corresponding with 900 data points obtained from the class of interest (5 AH samples) and two selected features (the mean and variance of the histogram distribution). The pre-processing dataset for machine learning implementation is explained in subsection 3.5. Note that the total dataset from the class of interest is 1800 data points, while we selected randomly 50% of them for testing the performance of the classifier. In other words, the total dataset coming from the class of interest is split randomly into a 50% for the training stage and a 50% for the testing stage.

We used the Scikit-learn OC-SVM implementation [259] accompanied by a Gaussian kernel function. During the training stage, the parameter γ introduced in Eq. (3.5-10) was optimized using a standard grid search (in logarithmic scale) in the feature space. In this case, γ corresponds to the width parameter associated with a Gaussian kernel function. This value gave the best classification accuracy rate on the training dataset and define a nonlinear decision border to isolate the data points coming from the class of interest from the other data points corresponding with the other 14 samples. This optimized decision border is shown in Fig. (9.8). However, we can observe in Fig. (9.8) some of the data points from the class of no interest are wrongly placed inside the decision border. This happens in most of the real classification problems.

The machine was trained only by data points of the class of interest. The accuracy A during training was defined as: $A = \frac{N_{tr} - N_{Errors}}{N_{tr}} \times 100$, where N_{tr} is the number of training data points and N_{Errors} is the number of points classified by OC-SVM as points of the class of no interest. This accuracy measure can also be formulated as follows: $A = \frac{TP}{TP + FN} \times 100$.

In this case, the number of data points of the class of interest that are correctly classified is identified with TP (True Positives), and the number of data points of the class of interest that are wrongly classified is identified with FN (False Negatives). Since during training the machine we only access data points of the class of interest, maximizing the accuracy rate defined in this way minimizes the number of False Negative cases.

After training the machine, we tested the performance of the classifier by predicting the unseen dataset. The test dataset that we used consisted of 50% of the randomly selected data points (900 data points) from the class of interest in addition to all data points that belong to the other 14 samples ($14 \times 360 = 5040$), in which was grouped as the class of no interest. In this regard, the total number of the test dataset is 5940, which shows an unbalanced number of training datasets compared with the test dataset. In this situation, some measures of accuracy may fail [260], in the sense that they may give high accuracy values, even for cases when 50% or more of the data points of the class with the lowest number of points are wrongly classified.

The geometric mean of accuracies (gma) [261] defined as: $\text{gma} = \sqrt{\text{TP}_r \times \text{TN}_r} \times 100$ ($\text{TP}_r = \frac{\text{TP}}{\text{TP} + \text{FN}}$; $\text{TN}_r = \frac{\text{TN}}{\text{TN} + \text{FP}}$) was considered to measure the classification quality in order to deal with this problem.

The number of samples of no interest classified as samples of interest is identified with FP and the number of samples of interest classified as samples of no interest is identified with FN. The obtained classification accuracy is $\text{gma} = 98.23\%$. In particular, $\text{TP} = 889$, $\text{FN} = 11$, $\text{TN} = 4923$ and $\text{FP} = 117$.

The result demonstrates that the classifier only mistakenly classifies 11 out of 900 data points corresponding to a class of interest sample as the class of no interest, which indicates a high identification capability for recognizing the class of interest.

Figure (9.8) shows the decision border given by OC-SVM. A zoomed-in version of it is also shown in order to better visualize the classification result.

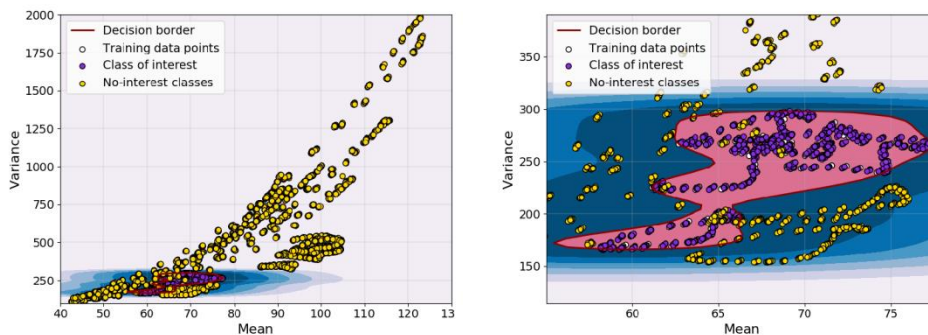


Fig. 9.8. The optimum decision border obtained during the training stage using the OC-SVM classifier for isolating the data points coming from the 5 validated AH samples. A zoomed-in version is also shown for visualization purposes. Figure from [248] under a Creative Commons By 4.0 license.

9.4.2. Classifying one sample against the other identical 3D printed samples

In the second scenario, we intend to classify one sample made of PLA-Aluminum with the Hilbert filling algorithm as a validated sample. In this case, we trained the machine in order to isolate the data points obtained from AH1 sample from the data points extracted from AH2, AH3, AH4, and AH5 samples. Note that all samples (AH1, AH2, AH3, AH4, and AH5) are made from the identical material (PLA- Aluminum) and filling algorithm (Hilbert). In this regard, data points corresponding with AH1 sample are classified as the class of interest, while the other data points corresponding with the 4 AH samples form the class of no interest.

So, the total number of datasets for the class of interest is 360 data points extracted from AH1 sample, but 50% of them (180 data points) were randomly selected as a training dataset, whereas the rest were used as a part of the test dataset. Moreover, the data points obtained from the AH2, AH3, AH4, and AH5 samples ($4 \times 360 = 1440$) form the other part of the test dataset. Generally speaking, 180 data points (speckle patterns or polarimetric signature codes) are used as a training dataset, and 1620 ($1440 + 180$) data points coming from AH1 (just 50% of the randomly selected dataset), AH2, AH3, AH4, and AH5 samples are used as a test dataset.

We retrained the machine with this new training dataset in a similar way explained in the previous subsection. Also, during the training stage, we found a new optimum γ parameter corresponding with a Gaussian kernel function using a standard grid search (in logarithmic scale) in the feature space. The performance of the OC-SVM classifier to find the optimum nonlinear decision border is shown in Fig. (9.9), in which the data points corresponding with the validated sample are isolated from the data points corresponding with false samples (AH2, AH3, AH4, and AH5).

In this case, the obtained classification accuracy is $\text{gma}=96.39\%$. In particular, $\text{TP}= 180$, $\text{FN}= 0$, $\text{TN}= 1338$ and $\text{FP}= 102$. This demonstrates that all data points of the class of interest are correctly classified inside the decision border, whereas the trained machine mostly rejects data points (polarimetric signature codes) extracted from invalid samples.

These results indicate that 3D printers print identical samples with different microstructures and mechanical properties, and therefore, they might be used as PUF materials, in which this physical structure is hard to predict [245, 246].

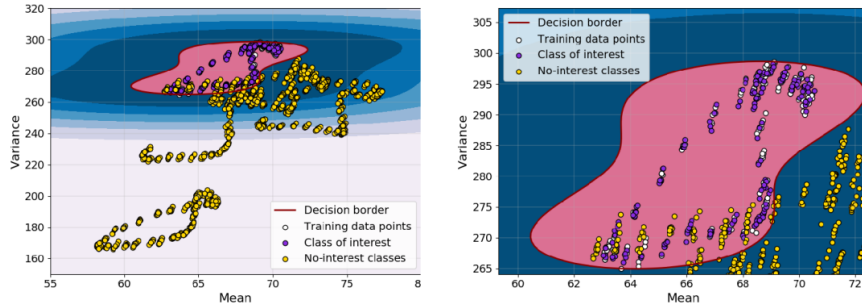


Fig. 9.9. The optimum decision border obtained during the training stage using the OC-SVM classifier for isolating the data points coming from a validated AH sample. Figure from [248] under a Creative Commons By 4.0 license.

In conclusion, we suggested an approach to synthesize and fabricate the nanoparticle encoded optical codes using a low-cost 3D printer. Our practical approach can substantially simplify the transition of optical techniques for security authentication. We set out this problem as a highly unbalanced, one-class pattern recognition in the sense that the system should be able to distinguish just one type of 3D printed structure.

To sum up, we considered two classification scenarios, in which the unique and synthesized optical codes using polarimetric signatures and 3D physical keys have been obtained. According to the accuracies obtained from two classification scenarios, our approach can identify the validated samples with a high rate of success using a relatively simple optical setup and low-cost technology.

10. Conclusion remarks

This section aims to summarize the algorithms and methods proposed in this thesis. In section 4:

1. We described an efficient approach to generating light beams with arbitrary intensity profiles and phase distributions.
2. A fast method has been introduced to characterize liquid crystal displays based on the Mach-Zehnder interferometer and fringe analysis in the Fourier domain.
3. We suggested using the KNN classifier to map DPH Arrizón's approach into any arbitrary modulation curve. This approach is around 80 times faster than conventional calculations, which require an extensive search of the minimum Euclidean distance.

In section 5:

4. A binary approach has been introduced to synthesize optical beams in order to encode character codes.
5. The distribution of binary values in radial annuli and azimuthal sectors forms a Circular Encoder, which can be encoded into holographic cells to be propagated in free space.
6. We demonstrated how characters of a list or a text could be encoded in this way in order to be used for autodetection applications, free-space optical communications, and optical encryption.

In section 6:

7. We described the experimental setup for generating highly focused beams with arbitrary complex amplitude and phase distributions and recording the corresponding Stokes images at the focal area without interaction with media.
8. We assessed the practical performance of the optical setup by comparing obtained experimental results with the numerically expected ones.
9. Since the detection of the longitudinal components of highly focused beams is a challenging task, we proposed a convenient method of estimating them using a phase retrieval algorithm and Gauss theorem.
10. The proposed approach also can be applied for decoding encrypted data into the longitudinal component of a highly focused beam.

In section 7:

11. We proposed an alternative method to estimate the aberrated wavefront at the focal plane of a vectorial diffraction system.
12. In contrast to the phase, the polarization state of optical fields is simply measurable; hence, we used polarimetric information in order to map the Zernike polynomials coefficients by means of trained neural networks.
13. Our approach aims to eliminate the necessity of phase retrieval for wavefront sensing applications, provided the beam used is known.
14. Our approach also can be applied for calibrating the complex optical system suffering from aberrations by synthesizing a properly polarized beam multiplied by a phase term that describes the Zernike expansion.

In section 8:

15. We presented an optical implementation of the visual encryption method using focused fields and tunable spiral polarization.
16. The numerical and experimental framework for encrypting 10-bit character codes based on Naor's and Shamir's secret sharing using the bitwise XOR operation has been proposed.
17. A proper binary approach was introduced to encode obscured cipher-character codes into holography cells, which formed a set of training datasets dependent on the properties of the optical system and design variables.
18. A multidimensional array (PMI), including polarimetric information, has been introduced to convolutional neural networks to recover obscured character codes into the longitudinal component of a highly focused beam without the necessity of applying phase retrieval algorithms.
19. Based on analyzing the system, the proposed algorithm is robust against noises and partially against occlusion attacks.
20. We justified that if an attacker is not able to access the complete group of channels of polarimetric mapping images, they will not be able to recover the expected character. Hence, the number of recipients involved might be increased up to twelve.

In section 9:

21. We proposed the synthesis, implementation, and classification of nanoparticle encoded optical codes.

22. We demonstrated the nanoparticle encoding and fabrication of PUFs using thermoplastic 3D printer filaments with metallic-like powder (aluminum, copper, or brass).
23. The classification of the codes has been carried out using polarimetric imaging based on the polarimetric signature.
24. Two classification scenarios have been considered: in the first one, one type of codes with the identical printed material and printing algorithm was discriminated against a large number of other codes. In the second one, one particular sample was compared against the rest identical samples.
25. In our experiments, not only the overall accuracy in both cases was excellent, but also the False Negative value, for instance, the number of polarimetric signatures of the code class of interest wrongly classified as a class of no interest, was very low, which confirms the capability of the proposed optically encoded samples with the polarimetric signature approach.

References

1. Encryption. (2022, June 10). In Wikipedia. <https://en.wikipedia.org/wiki/Encryption>
2. P. K. H. Fielding, J. L. Horner, and C. K. Makekai, "Optical fingerprint identification by binary joint transform correlation," *Opt. Eng.* 30, 1958–1961 (1991).
3. H.-Y. Li, Y. Qiao, and D. Psaltis, "Optical network for real-time face recognition," *Appl. Opt.* 32, 5026–5035 (1993).
4. B. Javidi, J. L. Horner, "Optical pattern recognition for validation and security verification," *Opt. Eng.* 33, 1752-1756 (1994).
5. J. Rodolfo, H. Rajbenbach, and J.-P. Huignard, "Performance of a photorefractive joint transform correlator for fingerprint identification," *Opt. Eng.* 34, 1166–1171 (1995).
6. T. Grycewicz and B. Javidi, "Experimental comparison of binary joint transform correlators used for fingerprint identification," *Opt. Eng.* 35, 2519-2525 (1996).
7. C. L. Wilson, C. I. Watson, and E. G. Paek, "Combined optical and neural network fingerprint matching," in *Optical Pattern Recognition VIII*, D. P. Casasent and T.-H. Chao, eds., Proc. SPIE 3073, 373–383 (1997).
8. P. Réfrégier and B. Javidi, "Optical image encryption based on input plane and Fourier plane random encoding," *Opt. Lett.* 20, 767–769 (1995).
9. P. Refregier and B. Javidi, "Optical image encryption using input plane and Fourier plane random encoding" Proc. SPIE 2565 62–8 (1995).
10. B. Javidi and E. Ahouzi, "Optical security system with Fourier plane encoding," *Appl. Opt.* 37, 6247-6255 (1998).
11. W. Chen, B. Javidi, and X. Chen, "Advances in optical security systems," *Adv. Opt. Photon.* 6, 120-155 (2014).
12. A. W. Lohmann, "Image rotation, Wigner rotation, and the fractional Fourier transform," *J. Opt. Soc. Am. A* 10, 2181-2186 (1993).
13. G. Unnikrishnan and Kehar Singh, "Double random fractional Fourier domain encoding for optical security," *Optical Engineering.* 39,11 (2000).
14. G. Unnikrishnan, J. Joseph, and K. Singh, "Optical encryption by double-random phase encoding in the fractional Fourier domain," *Opt. Lett.* 25, 887-889 (2000).
15. G. Situ and J. Zhang, "Double random-phase encoding in the Fresnel domain," *Opt. Lett.* 29, 1584-1586 (2004).
16. Y. Shi, G. Situ, and J. Zhang, "Multiple-image hiding in the Fresnel domain," *Opt. Lett.* 32, 1914-1916 (2007).
17. O. Matoba and B. Javidi, "Encrypted optical memory system using three-dimensional keys in the Fresnel domain," *Opt. Lett.* 24, 762-764 (1999).
18. H. Singh, A. K. Yadav, S. Vashisth, and K. Singh, "Fully phase image encryption using double random-structured phase masks in gyrator domain," *Appl. Opt.* 53, 6472-6481 (2014).
19. Z. Liu, L. Xu, C. Lin, and S. Liu, "Image encryption by encoding with a nonuniform optical beam in gyrator transform domains," *Appl. Opt.* 49, 5632–5637 (2010).
20. O. Matoba and B. Javidi, "Encrypted optical storage with wavelength-key and random phase codes," *Appl. Opt.* 38, 6785-6790 (1999).
21. G. Situ and J. Zhang, "Multiple-image encryption by wavelength multiplexing," *Opt. Lett.* 30, 1306–1308 (2005).
22. B. Javidi and T. Nomura, "Securing information by use of digital holography," *Opt. Lett.* 25, 28-30 (2000).

23. E. Tajahuerce and B. Javidi, "Encrypting three-dimensional information with digital holography," *Appl. Opt.* 39, 6595-6601 (2000).
24. A. Carnicer, M. Montes-Usategui, S. Arcos, and I. Juvells, "Vulnerability to chosen-ciphertext attacks of optical encryption schemes based on double random phase keys," *Opt. Lett.* 30, 1644-1646 (2005).
25. X. Peng, P. Zhang, H. Wei, and B. Yu, "Known-plaintext attack on optical encryption based on double random phase keys," *Opt. Lett.* 31, 1044-1046 (2006).
26. Y. Frauel, A. Castro, T. J. Naughton, and B. Javidi, "Resistance of the double random phase encryption against various attacks," *Opt. Express* 15, 10253-10265 (2007).
27. P. Kumar, A. Kumar, J. Joseph, and K. Singh, "Impulse attack free double-random-phase encryption scheme with randomized lens-phase functions," *Opt. Lett.* 34, 331-333 (2009).
28. T. J. Naughton, B. M. Hennelly, and T. Dowling, "Introducing secure modes of operation for optical encryption," *J. Opt. Soc. Am. A* 25, 2608-2617 (2008).
29. H. Tashima, M. Takeda, H. Suzuki, T. Obi, M. Yamaguchi, and N. Ohya, "Known plaintext attack on double random phase encoding using fingerprint as key and a method for avoiding the attack," *Opt. Express* 18, 13772-13781 (2010).
30. N. K. Nishchal, *Optical Cryptosystems*, IOP Publishing (2019).
31. O. Matoba, T. Nomura, E. Perez-Cabre, M. S. Millan, and B. Javidi, "Optical techniques for information security," *Proc. IEEE* 97, 1128-1148 (2009).
32. B. Javidi, A. Carnicer, M. Yamaguchi, T. Nomura, E. Pérez-Cabré, M. S. Millán, N. K. Nishchal, R. Torroba, J. F. Barrera, W. He, X. Peng, A. Stern, Y. Rivenson, A. Alfalou, C. Brosseau, C. Guo, J. T. Sheridan, G. Situ, M. Naruse, T. Matsumoto, I. Juvells, E. Tajahuerce, J. Lancis, W. Chen, X. Chen, P. W. H. Pinkse, A. P. Mosk, and A. Markman, "Roadmap on optical security," *J. Opt.* 18, 083001 (2016).
33. H. Lai, W. He, and X. Peng, "Optical Hash function based on two-beam interference," *Appl. Opt.* 52, 6213-6219 (2013).
34. Y. Y. Wang, Y. R. Wang, Y. Wang, H. Li, and W. Sun, "Optical image encryption based on binary Fourier transform computer-generated hologram and pixel scrambling technology," *Optics and Lasers in Engineering*, 45, 761-765(2007).
35. P. Palevicius and M. Ragulskis, "Image communication scheme based on dynamic visual cryptography and computer generated holography," *Optics Communications*, 335, 161-167 (2015).
36. N. Towghi, B. Javidi, and Z. Luo, "Fully phase encrypted image processor," *J. Opt. Soc. Am. A* 16, 1915-1927 (1999).
37. X. Tan, O. Matoba, T. Shimura, K. Kuroda, and B. Javidi, "Secure optical storage that uses fully phase encryption," *Appl. Opt.* 39, 6689-6694 (2000).
38. P. C. Mogensen and J. Glückstad, "phase-only optical encryption," *Opt. Lett.* 25, 566-568 (2000).
39. N. K. Nishchal, J. Joseph, K. Singh, "Optical phase encryption by phase contrast using electrically addressed spatial light modulator," *Optics Communications*, 217, 117-122 (2003).
40. R. W. Gerchberg and W. O. Saxton, "A practical algorithm for the determination of phase from image and diffraction plane pictures," *Optik* 35 237-50 (1972).
41. J.R. Fienup, "Reconstruction of an object from the modulus of its Fourier transform," *Opt Lett.* 3, 27-9 (1978).
42. Y. Shechtman, Y. C. Eldar, O. Cohen, H. N. Chapman, J. Miao and M. Segev, "Phase Retrieval with Application to Optical Imaging: A contemporary overview," in *IEEE Signal Processing Magazine*, 32, 87-109 (2015).

43. J. Glückstad, "Phase contrast image synthesis," *Optics Communications*, 130, 255-230 (1996).
44. F. Zernike, "How I discovered phase contrast," *Science*, 121, 345-349 (1995).
45. A. Alfalou and C. Brosseau, "Dual encryption scheme of images using polarized light," *Opt. Lett.* 35, 2185-2187 (2010).
46. S. K. Rajput and N. K. Nishchal, "Image encryption using polarized light encoding and amplitude and phase truncation in the Fresnel domain," *Appl. Opt.* 52, 4343-4352 (2013).
47. S. K. Rajput, D. Kumar, N. K. Nishchal, "Photon counting imaging and polarized light encoding for secure image verification and hologram watermarking," *J. Opt.* 16, 125406 (2014).
48. S. K. Rajput and N. K. Nishchal, "Asymmetric color cryptosystem using polarization selective diffractive optical element and structured phase mask," *Appl. Opt.* 51, 5377-5386 (2012).
49. P. C. Mogensen, J. Glückstad, "A phase-based optical encryption system with polarisation encoding," *Optics Communications*, 173, 77-183 (2000).
50. E. Carcolé, J. Campos, and S. Bosch, "Diffraction theory of Fresnel lenses encoded in low-resolution devices," *Applied optics*, 33, 162-174, (1994).
51. J. A. Davis, D. E. McNamara, D. M. Cottrell, and T. Sonehara, "Two-dimensional polarization encoding with a phase-only liquid-crystal spatial light modulator," *Applied Optics*, 39, 1549-1554, (2000).
52. R. L. Eriksen, P. C. Mogensen, and J. Glückstad, "Elliptical polarisation encoding in two dimensions using phase-only spatial light modulators," *Optics communications*, 187, 325-336 (2001).
53. X.-L. Wang, J. Ding, W.-J. Ni, C.-S. Guo, and H.-T. Wang, "Generation of arbitrary vector beams with a spatial light modulator and a common path interferometric arrangement," *Optics letters*, 32, 3549-3551 (2007).
54. J. A. Davis, D. E. McNamara, D. M. Cottrell, and T. Sonehara, "Two-dimensional polarization encoding with a phase-only liquid-crystal spatial light modulator," *Applied Optics*, 39, 1549-1554 (2000).
55. R. L. Eriksen, P. C. Mogensen, and J. Glückstad, "Elliptical polarisation encoding in two dimensions using phase-only spatial light modulators," *Optics communications*, 187, 325-336 (2001).
56. X. Tan, O. Matoba, Y. Okada-Shudo, M. Ide, T. Shimura, and K. Kuroda, "Secure optical memory system with polarization encryption," *Applied optics*, 40, 2310-2315 (2001).
57. O. Matoba and B. Javidi, "Secure holographic memory by double random polarization encryption," *Applied optics*, 43, 2915-2919 (2004).
58. J. F. Barrera, R. Henao, M. Tebaldi, R. Torroba, and N. Bolognini, "Multiplexing encrypted data by using polarized light," *Optics communications*, 260, 109-112 (2006).
59. D. Maluenda, A. Carnicer, R. Martínez-Herrero, I. Juvells, and B. Javidi, "Optical encryption using photon-counting polarimetric imaging," *Optics express*, 23, 655-666 (2015).
60. O. Graydon, "Optical encryption: Polarization keys," *Nature Photonics*, 9, 141-141 (2015).
61. F. Areeba, N. K. Nishchal, "Optical image security using Stokes polarimetry of spatially variant polarized beam," *Optics Communications*, 417, 30-36 (2018).
62. A. Carnicer, I. Juvells, B. Javidi, and R. Martínez-Herrero, "Optical encryption in the longitudinal domain of focused fields," *Optics express*, 24, 6793-6801 (2016).

63. A. Carnicer, I. Juvells, B. Javidi, and R. Martínez-Herrero, "Optical encryption in the axial domain using beams with arbitrary polarization," *Optics and Lasers in Engineering*, 89, 145-149 (2017).
64. X. Li, T. H. Lan, C. H. Tien, and M. Gu, "Three-dimensional orientation-unlimited polarization encryption by a single optically configured vectorial beam," *Nat. Commun.* 3998 (2012).
65. C. Lin, X. Shen, B. Hua, Z. Wang, "Three-dimensional polarization marked multiple-QR code encryption by optimizing a single vectorial beam," *Optics Communications*, 352, 25-32 (2015).
66. H. Y. Tu, C. J. Cheng, and M. L. Chen, "Optical image encryption based on polarization encoding by liquid crystal spatial light modulators," *J. Opt. A: Pure Appl. Opt.* 6, 524-528 (2004).
67. J. W. Han, C. S. Park, D. H. Ryu, and E. S. Kim, "Optical image encryption based on XOR operation," *Optical Engineering*, 38 (1999).
68. J. W. M. Chon, X. Gan, and M. Gu, "Splitting of the focal spot of a high numerical-aperture objective in free space," *Appl. Phys. Lett.* 81, 1576-1578 (2002).
69. M. Gu, *Advanced Optical Imaging Theory* (Springer, Heidelberg, 2000).
70. T. Grosjean and D. Courjon, "Polarization filtering induced by imaging systems: Effect on image structure," *Phys. Rev. E* 67, 046611 (2003).
71. L. Novotny and B. Hecht, *Principles of Nano-Optics* (Cambridge University Press, 2012).
72. E. Pérez-Cabré, M. Cho, and B. Javidi, "Information authentication using photon-counting double-random-phase encrypted images," *Opt. Lett.* 36, 22-24 (2011).
73. S. Yeom, B. Javidi, and E. Watson, "Photon counting passive 3D image sensing for automatic target recognition," *Opt. Express* 13, 9310-9330 (2005).
74. J. W. Goodman, *Statistical Optics* (John Wiley & Sons, 1985)
75. J. M. Meruga, W. M. Cross, P. S. May, Q. Luu, G. A. Crawford, and J. J. Kellar, "Security printing of covert quick response codes using upconverting nanoparticle inks," *Nanotechnology* 23, 395201 (2012).
76. A. Markman, B. Javidi, and M. Tehranipoor, "Photon-counting security tagging and verification using optically encoded QR codes," *IEEE Photon. J.* 6, 1-9 (2014).
77. A. Carnicer and B. Javidi, "Optical security and authentication using nanoscale and thin-film structures," *Adv. Opt. Photon.* 9, 218-256 (2017).
78. A. Markman, A. Carnicer, and B. Javidi, "Security authentication with a three-dimensional optical phase code using random forest classifier," *J. Opt. Soc. Am. A* 33, 1160-1165 (2016).
79. A. Carnicer, A. Hassanfiroozi, P. Latorre-Carmona, Y.-P. Huang, and B. Javidi, "Security authentication using phase-encoded nanoparticle structures and polarized light," *Opt. Lett.* 40, 135-138 (2015).
80. A. Carnicer, O. Arteaga, E. Pascual, A. Canillas, S. Vallmitjana, B. Javidi, and E. Bertran, "Optical security verification by synthesizing thin films with unique polarimetric signatures," *Opt. Lett.* 40, 5399-5402 (2015).
81. A. Carnicer, O. Arteaga, J. M. Suñé, and B. Javidi, "Authentication of gold nanoparticle encoded pharmaceutical tablets using polarimetric signatures," *Opt. Lett.* 41, 4507-4510 (2016).
82. V. -M. Freire, C. Corbella, E. Bertran, S. Portal-Marco, M. Rubio-Roy, and J.-L. Andújar, "Anisotropic Surface properties of micro/nanostructured a-C:H:F thin films with self-assembly applications," *J. Appl. Phys.* 111, 124323 (2012).

83. O. Arteaga, M. Baldrís, J. Antó, A. Canillas, E. Pascual, and E. Bertran, "Mueller matrix microscope with a dual continuous rotating compensator setup and digital demodulation," *Appl. Opt.* 53, 2236-2245 (2014).
84. T. Cover and P. Hart, "Nearest neighbor pattern classification," *IEEE Transactions on Information Theory.* 13, 21-27 (1967).
85. Z. H. Zhou, *Machine Learning* (Springer Nature Singapore Pte Ltd 2021).
86. S. Raschka, *Python Machine Learning* (Packt Publishing Ltd, 2015).
87. D. Sarkar, R. Bali, T. Sharma, *Practical Machine Learning with Python* (Springer, 2018).
88. L. Zhou, Y. Xiao, and W. Chen, "Machine-learning attacks on interference-based optical encryption: experimental demonstration," *Opt. Express* 27, 26143-26154 (2019).
89. C. Natalino, M. Schiano, A. Di Giglio, L. Wosinska, and M. Furdek, "Experimental Study of Machine-Learning-Based Detection and Identification of Physical-Layer Attacks in Optical Networks," *J. Lightwave Technol.* 37, 4173-4182 (2019).
90. Z. He, Y. Wang, and D. Huang, "Wavelength attack recognition based on machine learning optical spectrum analysis for the practical continuous-variable quantum key distribution system," *J. Opt. Soc. Am. B* 37, 1689-1697 (2020).
91. L. Zhou, X. Yin, and C. Wen, "Vulnerability to machine learning attacks of optical encryption based on diffractive imaging," *Optics and Lasers in Engineering* 125, 105858 (2020).
92. M. Liao, S. Zheng, S. Pan, D. Lu, W. He, G. Situ, and X. Peng, "Deep-learning-based ciphertext-only attack on optical double random phase encryption," *Opto-Electronic Advances*, 4, 200016-1 (2021).
93. Y. Rivenson, Y. Wu, and A. Ozcan, "Deep learning in holography and coherent imaging," *Light sci Appl.* 8, 85 (2019).
94. R. Horisaki, R. Takagi, and J. Tanida, "Deep-learning-generated holography," *Appl. Opt.* 57, 3859-3863 (2018).
95. T. Liu, K. Haan, Y. Rivenson, W. Zhensong, X. Zeng, Y. Zhang, and A. Ozcan, "Deep learning-based super-resolution in coherent imaging system," *Sci Rep.* 9, 3926 (2019).
96. C. Guerrero-Mendez, T. Saucedo-Anaya, I. Moreno, M. Araiza-Esquivel, C. Olvera-Olvera, and D. Lopez-Betancur, "Digital Holographic Interferometry without Phase Unwrapping by a Convolutional Neural Network for concentration Measurements in Liquid samples," *appl. Sci.* 10, 4974 (2020).
97. Y. Wu, Y. Rivenson, Y. Zhang, Z. Wei, H. Günaydin, X. Lin, and A. Ozcan, "Extended depth-of-field in holographic imaging using deep-learning-based autofocusing and phase recovery," *Optica* 5, 704-710 (2018).
98. S. W. Paine and J. R. Fienup, "Machine learning for improved image-based wavefront sensing," *Opt. Lett.* 43, 1235-1238 (2018).
99. Y. Nishizaki, M. Valdivia, R. Horisaki, K. Kitaguchi, M. Saito, J. Tanida, and E. Vera, "Deep learning wavefront sensing," *Opt. Express* 27, 240-251 (2019).
100. S. Feng, Q. Chen, G. Gu, T. Tao, L. Zhang, Y. Hu, W. Yin, C. Zuo, "Fringe pattern analysis using deep learning," *Adv. Photon.* 1, 025001 (2019).
101. H. Yu, D. Zheng, J. Fu, Y. Zhang, C. Zuo, and J. Han, "Deep learning-based fringe modulation-enhancing method for accurate fringe projection profilometry," *Opt. Express* 28, 21692-21703 (2020).
102. Y. Qin, S. Wan, Y. Wan, J. Weng, W. Liu, and Q. Gong, "Direct and accurate phase unwrapping with deep neural network," *Appl. Opt.* 59, 7258-7267 (2020).
103. Y. Rivenson, Y. Zhang, H. Günaydin, D. Teng, and A. Ozcan, "Non-Iterative Holographic Image Reconstruction and Phase Retrieval Using a Deep Convolutional Neural Network,"

- in Conference on Lasers and Electro-Optics, OSA Technical Digest (online) (Optica Publishing Group, 2018), paper STh1J.3.
- 104.Ç. Işıl, F. S. Oktem, and A. Koç, “Deep iterative reconstruction for phase retrieval,” *Appl. Opt.* 58, 5422-5431 (2019).
 - 105.A. Goy, K. Arthur, S. Li, and G. Barbastathis, “Low Photon Count Phase Retrieval Using Deep Learning,” *Phys Rev Lett.* 121, 243902 (2018).
 - 106.Y. Nishizaki, R. Horisaki, K. Kitaguchi, and J. Tanida, “Analysis of non-iterative phase retrieval based on machine learning,” *Opt Rev* 27, 136–141 (2020).
 - 107.Y. Rivenson, Y. Zhang, H. Günaydın, D. Teng, and A. Ozcan, “Phase recovery and holographic image reconstruction using deep learning in neural networks,” *Light Sci Appl* 7, 17141 (2018).
 - 108.J. White, S. Wang, W. Eschen, and J. Rothhardt, “Real-time phase-retrieval and wavefront sensing enabled by an artificial neural network,” *Opt. Express* 29, 9283-9293 (2021).
 - 109.A. Sinha, J. Lee, S. Li, and G. Barbastathis, “Lensless computational imaging through deep learning,” *Optica* 4, 1117-1125 (2017).
 - 110.A. Shamir, “How to share a secret,” *Commun ACM* 22, 612–13 (1979).
 - 111.G. R. Blakley, “Safeguarding cryptographic keys,” *Proc AFIPS* 48, 313–17 (1979).
 - 112.Y. G. Desmedt, Y. Frankel, “Threshold cryptosystems,” *Proc CRYPTO* 435:307–15 (1989).
 - 113.M. Naor, A. Shamir, “Visual cryptography,” *Advances in Cryptology EUROCRYPT'94. Lecture Notes in Computer Science* 950, 1–12 (1995).
 - 114.D. Lu, M. Liao, W. He, Q. Xing, G. Verma, X. Peng, “Experimental optical secret sharing via an iterative phase retrieval algorithm,” *Optics and Lasers in Engineering*, 126, 105904 (2020).
 - 115.X. Pan, F. Meng, Y. Wang, X. Yang, X. Peng, W. He, G. Dong, and H. Chen, “Multilevel image authentication using shared secret threshold and phase retrieval,” *J Mod Optics* 61, 1470-1478 (2014).
 - 116.X. Deng, W. Wen, X. Mi, X. Long, “Optical threshold secret sharing scheme based on basic vector operations and coherence superposition,” *Opt Commun* 341, 22–77 (2015).
 - 117.X. Deng, Z. Shi, W. Wen, “Threshold secret sharing scheme based on phase-shifting interferometry,” *Appl Opt* 55, 8855–8859 (2016).
 - 118.X. Li, Meng XF, Y. Wang, X. Yang, Y. Yin, X. Peng, W. He, G. Dong, and H. Chen, “Secret shared multiple-image encryption based on row scanning compressive ghost imaging and phase retrieval in the Fresnel domain,” *Opt Laser Eng* 96, 7–16 (2017).
 - 119.X. Li, X. Meng, Y. Yin, Y. Wang, X. Yang, X. Peng, X. He, G. Dong, H. Chen, “Multilevel image authentication using row scanning compressive ghost imaging and hyperplane secret sharing algorithm,” *Opt Laser Eng* 108, 28–35 (2018).
 - 120.T. Zhao and Y. Chi, “A novel secret sharing with two users based on joint transform correlator and compressive sensing,” *J Mod Optics* 65, 1072-1080 (2018).
 - 121.P. Palevicius, M. Ragulskis, “Image communication scheme based on dynamic visual cryptography and computer generated holography,” *Opt Commun* 33, 161-167 (2015).
 - 122.P. Kumar and N. K. Nishchal, “Enhanced exclusive-OR and quick response code-based image encryption through incoherent illumination,” *Appl. Opt.* 58, 1408-1412 (2019).
 - 123.E. Collett. *Field Guide to Polarization* (SPIE, 2005).
 - 124.B. E. A Saleh and M. C. Teich. *Fundamentals of photonics*. (2nd ed. Wiley-Interscience 2007).
 - 125.M. Leutenegger, R. Rao, R. A. Leitgeb, and T. Lasser, “Fast focus field calculations,” *Opt. Express* 14, 11277-11291 (2006).

126. P. Debye, "Das Verhalten von Lichtwellen in der N ahe eines Brennpunktes oder einer Brennlinie," *Ann. Phys.* 30, 755–776 (1909).
127. E. Wolf, "Electromagnetic diffraction in optical systems, I. An integral representation of the image field," *Proc. R. Soc. London Ser. A* 253, 349–357 (1959).
128. B. Richards, E. Wolf, "Electromagnetic diffraction in optical systems, II. Structure of the image field in an aplanatic system," *Proc. R. Soc. London Ser. A* 253, 358–379 (1959).
129. Y. H. Wu and P. Chavel, "Cell-oriented on-axis computer-generated holograms for use in the Fresnel diffraction mode," *Appl. Opt.* 23, 228-238 (1984).
130. Y. Sang-Yi, C. Kyo-II, R. Chung-Sang, C. Kwang-Hoon, L. Seung-Hyun, and K. Eun-Soo, "Encryption of cell-oriented computer generated hologram by using visual cryptography," *Technical Digest. CLEO/Pacific Rim '99. Pacific Rim Conference on Lasers and Electro-Optics.* 3, 817-818 (1999).
131. C. K. Hsueh and A. A. Sawchuk, "Computer-generated double-phase holograms," *Appl. Opt.* 17, 3874-3883 (1978).
132. J. M. Florence, R. D. Juday, "Full-complex spatial filtering with a phase mostly DMD," *Proc. SPIE* 1558, *Wave Propagation and Scattering in Varied Media II*, (11 November 1991). <https://doi.org/10.1117/12.49655>.
133. D. Mendlovic, G. Shabtay, U. Levi, Z. Zalevsky, and E. Marom, "Encoding technique for design of zero-order (on-axis) Fraunhofer computer-generated holograms," *Appl. Opt.* 36, 8427-8434 (1997).
134. V. Arriz n, "Improved double-phase computer-generated holograms implemented with phase-modulation devices," *Opt. Lett.* 27, 595-597 (2002).
135. V. Arriz n and D. S nchez-de-la-Llave, "Double-phase holograms implemented with phase-only spatial light modulators: performance evaluation and improvement," *Appl. Opt.* 41, 3436-3447 (2002).
136. V. Arriz n, "Complex modulation with a twisted-nematic liquid-crystal spatial light modulator: double-pixel approach," *Opt Lett.* 28, 1359-61 (2003).
137. V. Arriz n, "Optimum on-axis computer-generated hologram encoded into low-resolution phase-modulation devices," *Opt. Lett.* 28, 2521-2523 (2003).
138. V. Arriz n, L. A. Gonz lez, R. Ponce, and A. Serrano-Heredia, "Computer-generated holograms with optimum bandwidths obtained with twisted-nematic liquid-crystal displays," *Appl. Opt.* 44, 1625-1634 (2005).
139. K. Ahmadi, Beam implementation with a translucent twisted-nematic liquid crystal display, in: P. J. Rosen (Ed.), *Holography- Recent Advances and Applications*, IntechOpen, Rijeka, 2022, Ch. 25. DOI: 10.5772/intechopen.105671.
140. A. Gholamy, V. Kreinovich, O. Kosheleva, Why 70/30 or 80/20 relation between training and testing sets: A pedagogical explanation, *Departmental Technical Reports (CS)*. The University of Texas at El Paso (2018).
141. C. Cortes, V. Vapnic, "Support-vector network," *Machine Learning* 20, 273-297 (1995).
142. Y. LeCun, L. Bottou, Y. Bengio, and P. Haffner, "Gradient-based Learning Applied to Document Recognition," *Proceedings of the IEEE*, 86(11):2278–2324 (1998).
143. I. Goodfellow, Y. Bengio, and A. Courville, *Deep learning* (MIT Press, 2016).
144. M. L. Cruz, A. Castro, and V. Arriz n, "Phase shifting digital holography implemented with a twisted-nematic liquid-crystal display," *Appl. Opt.* 48, 6907-6912 (2009).
145. D. Maluenda, I. Juvells, R. Mart nez-Herrero, A. Carnicer, "A digital holography technique for generating beams with arbitrary polarization and shape," *Proceedings of SPIE - The International Society for Optical Engineering.* 8550. 10.1117/12.979926. (2012).

146. C. Shen, J. Tan, C. Wei and Z. Liu, "Coherent diffraction imaging by moving a lens," *Opt. Express* 24, 16520-16529 (2016).
147. Z. Y. Rong, Y.-J. Han, S.-Z. Wang, and C.-S. Guo, "Generation of arbitrary vector beams with cascaded liquid crystal spatial light modulators," *Opt. Express* 22, 1636–1644 (2014).
148. R. Martínez-Herrero, D. Maluenda, I. Juvells, and A. Carnicer, "Experimental implementation of tightly focused beams with unpolarized transversal component at any plane," *Opt. Express* 22, 32419-32428 (2014).
149. D. Maluenda, R. Martínez-Herrero, I. Juvells, and A. Carnicer, "Synthesis of highly focused fields with circular polarization at any transverse plane," *Opt. Express* 22, 6859-6867 (2014).
150. I. Moreno, J. Campos, C. Gorecki and M.J. Yzuel, "Effects of amplitude and phase mismatching errors in the generation of a Kinoform for pattern recognition," *Jpn. J. Appl. Phys.* 34, 6423-6432 (1995).
151. S. Lin, C. Li, C. Kuo and H. Yeh, "Fresnel Lenses in 90° Twisted-Nematic Liquid Crystals with Optical and Electrical Controllability," in *IEEE Photonics Technology Letters* 28, 1462-1464 (2016).
152. C. Lin, H. Huang and J. Wang, "Polarization-Independent Liquid-Crystal Fresnel Lenses Based on Surface-Mode Switching of 90° Twisted-Nematic Liquid Crystals," in *IEEE Photonics Technology Letters* 22, 137-139 (2010).
153. C. W. Wu, G. Thompson and S. L. Wright, "Multiple images viewable on twisted-nematic mode liquid-crystal displays," *IEEE Signal Processing Letters* 10, 225-227 (2003).
154. C. J. Cheng, M. L. Chen, and H. Y. Tu, "Polarization Encoding for Multi-channel Optical Encryption using Twisted Nematic Liquid Crystal Displays," in *Pacific Rim Conference on Lasers & Electro-Optics*, 981-982 (2005).
155. I. Moreno, N. Bennis, J. A. Davis, and C. Ferreira, "Twist angle determination in liquid crystal displays by location of local adiabatic points," *Opt. Communications* 158, 231-238 (1998).
156. J. A. Davis, I. Moreno, and P. Tsai, "Polarization eigenstates for twisted-nematic liquid-crystal displays," *Appl. Opt.* 37, 937-945 (1998).
157. R. Ponce, A. Serrano-Heredia, and V. M. Arrizón, "Simplified optimum phase-only configuration for a TNLCD," *Proc. SPIE* 5556, 206–213 (2004).
158. J. L. Pezzaniti and R. A. Chipman, "Phase-only modulation of a twisted nematic liquid-crystal TV by use of the eigenpolarization states," *Opt. Lett.* 18, 1567-1569 (1993).
159. T. Yu and Y. Lo, "A Highly Phase-Sensitive Heterodyne Polariscope for the Full-Field Measurement of Twisted- Nematic Liquid Crystal," *IEEE Photonics Technology Letters* 20, 1778-1780 (2008).
160. S. Wang, C. Lin and K. Yang, "A Simple Method to Measure Pretilt Angles of Inverse Twisted Nematic Liquid Crystal Cells," *Journal of Display Technology* 10, 1024-1029, (2014).
161. Y. Chiang, T. Chou, S. Chen and C. Chao, "Effects of Low Viscosity Liquid on the Electro-Optical Properties of Inverse Twisted Nematic Liquid Crystal Display," *IEEE Transactions on Electron Devices* 64, 1630-1634 (2017).
162. W. Hung, M. Tsai, C. Wang, I. Jiang, and W. Cheng, "Simple parameter determination for twisted nematic liquid-crystal display," *Appl. Opt.* 46, 3493-3497 (2007).
163. F. S. Y. Yeung and H. S. Kwok, "Truly bistable twisted nematic liquid crystal display," *Proceedings of the Sixth Chinese Optoelectronics Symposium (IEEE Cat. No.03EX701)* 225-227 (2003).

164. C. Hsieh, G. Y. Li, T. T. Wu, C. Y. Huang, C. J. Tien, K. Y. Lo, and C. H. Lin, "Twisted Nematic Dual-View Liquid Crystal Display Based on Patterned Electrodes," *Journal of Display Technology* 10, 464-469 (2014).
165. V. Durán, J. Lancis, E. Tajahuerce, and M. Fernández-Alonso, "Phase-only modulation with a twisted nematic liquid crystal display by means of equi-azimuth polarization states," *Opt. Express* 14, 5607-5616 (2006).
166. J. Kim, S. Lee, D. Jeon and S. Lee, "Physical Model of Pixels in Twisted Nematic Active-Matrix Liquid Crystal Displays," *IEEE Transactions on Electron Devices* 62, 3308-3313(2015).
167. V. Duran, J. Lancis, E. Tajahuerce and V. Climent, "Poincaré Sphere Method for Optimizing the Phase Modulation Response of a Twisted Nematic Liquid Crystal Display," *Journal of Display Technology* 3, 9-14 (2007).
168. E. Matín-Badosa, A. Carnier, I. Juvells and S. Vallmitjana, "Complex modulation characterization of liquid crystal devices by interferometric data correlation," *Meas. Sci. Technol.* 8, 764-772 (1997).
169. H. Wang, Z. Dong, F. Fan, Y. Feng & Lou, Y. Lou, and X. Jiang, "Characterization of Spatial Light Modulator Based on the Phase in Fourier Domain of the Hologram and Its Applications in Coherent Imaging," *Applied Sciences*. 8. 1146. 10.3390/app8071146. (2018).
170. M. Takeda, H. Ida, and S. Kobayashi, "Fourier-transform method of fringe-pattern analysis for computer-based topography and interferometry," *J. Opt. Soc. Am.* 72156-72160, (1982).
171. C. Deotte, "Accelerating k-nearest neighbors 600x using RAPIDS cuML" [Internet]. 2005. Available from: <https://medium.com/rapids-ai/accelerating-k-nearest-neighbors-600x-using-rapids-cuml-82725d56401e>.
172. Q. Zhan, and J. R. Leger, "Focus shaping using cylindrical vector beams," *Opt. Express* 10, 324-331 (2002).
173. R. Dorn, S. Quabis, and G. Leuchs, "Sharper focus for a radially polarized light beam" *Phys. Rev. Lett.* 91, 233901 (2003).
174. N. Davidson and N. Bokor, "High-numerical-aperture focusing of radially polarized doughnut beams with a parabolic mirror and a flat diffractive lens," *Opt. Lett.* 29, 1318-1320 (2004).
175. H. Wang, L. Shi, B. Lukyanchuk, C. Sheppard, and C. T. Chong, "Creation of a needle of longitudinally polarized light in vacuum using binary optics," *Nat. Photonics* 2, 501-505 (2008).
176. G. M. Lerman, and U. Levy, "Effect of radial polarization and apodization on spot size under tight focusing conditions," *Opt. Express* 16, 4567-4581 (2008).
177. X. Hao, C. Kuang, T. Wang, and X. Liu, "Phase encoding for sharper focus of the azimuthally polarized beam," *Opt. Lett.* 35, 3928-3930 (2010).
178. S. N. Khonina, and S. G. Volotovskiy, "Controlling the contribution of the electric field components to the focus of a high-aperture lens using binary phase structures," *J. Opt. Soc. Am. A* 27, 2188-2197 (2010).
179. F. Kenny, D. Lara, O. Rodríguez-Herrera, and C. Dainty, "Complete polarization and phase control for focus-shaping in high-na microscopy" *Opt. Express* 20, 14015-14029 (2012).
180. L. Yang, X. Xie, S. Wang, and J. Zhou, "Minimized spot of annular radially polarized focusing beam" *Opt. Lett.* 38, 1331-1333 (2013).
181. G. Brakenhoff, P. Blom, and P. Barends, "Confocal scanning light microscopy with high aperture immersion lenses" *J. Microsc.* 117, 219-232 (1979).

182. D. Biss, and T. Brown, "Polarization-vortex-driven second-harmonic generation" *Opt. Lett.* 28, 923–925 (2003).
183. D. Oron, E. Tal, and Y. Silberberg, "Depth-resolved multiphoton polarization microscopy by third-harmonic generation" *Opt. Lett.* 28, 2315–2317 (2003).
184. C. J. Sheppard, and A. Choudhury, "Annular pupils, radial polarization, and superresolution," *Appl. Opt.* 43, 4322–4327 (2004).
185. K. Serrels, E. Ramsay, R. Warburton, and D. Reid, "Nanoscale optical microscopy in the vectorial focusing regime," *Nat. Photonics* 2, 311–314 (2008).
186. Y. Gorodetski, A. Niv, V. Kleiner, and E. Hasman, "Observation of the spin-based plasmonic effect in nanoscale structures," *Phys. Rev. Lett.* 101, 043903 (2008).
187. O. Masihzadeh, P. Schlup, and R. A. Bartels, "Enhanced spatial resolution in third-harmonic microscopy through polarization switching" *Opt. Lett.* 34, 1240–1242 (2009).
188. L. Vuong, A. Adam, J. Brok, P. Planken, and H. Urbach, "Electromagnetic spin-orbit interactions via scattering of subwavelength apertures," *Phys. Rev. Lett.* 104, 083903 (2010).
189. Q. Zhan, "Properties of circularly polarized vortex beams," *Opt. Lett.* 31, 867–869 (2006).
190. Q. Zhan, "Cylindrical vector beams: From mathematical concepts to applications," *Adv. Opt. Photonics* 1, 1–57 (2009).
191. C. Maurer, A. Jesacher, S. Fürhapter, S. Bernet, and M. Ritsch-Marte, "Tailoring of arbitrary optical vector beams". *New J. Phys.* 9, 78 (2007).
192. H.-T. Wang, et al. "A new type of vector fields with hybrid states of polarization," *Opt. Express* 18, 10786–10795 (2010).
193. X.-L. Wang, J. Ding, W.-J. Ni, C.-S. Guo, and H.-T. Wang, "Generation of arbitrary vector beams with a spatial light modulator and a common path interferometric arrangement" *Opt. Lett.* 32, 3549–3551 (2007).
194. I. Moreno, C. Iemmi, J. Campos, and M. J. Yzuel, "Jones matrix treatment for optical fourier processors with structured polarization," *Opt. Express* 19, 4583–4594 (2011).
195. D. Maluenda, I. Juvells, R. Martínez-Herrero, and A. Carnicer, "Reconfigurable beams with arbitrary polarization and shape distributions at a given plane," *Opt. Express* 21, 5432–5439 (2013).
196. E. H. Waller, and G. von Freymann, "Independent spatial intensity, phase and polarization distributions," *Opt. Express* 21, 28167–28174 (2013).
197. W. Han, Y. Yang, W. Cheng, Q. Zhan, "Vectorial optical field generator for the creation of arbitrarily complex fields," *Opt. Express* 21, 20692–20706 (2013).
198. R. Martínez-Herrero, I. Juvells, and A. Carnicer, "On the physical realizability of highly focused electromagnetic field distributions," *Opt. Lett.* 38, 2065–2067 (2013).
199. C.-S. Guo, Z.-Y. Rong, and S.-Z. Wang, "Double-channel vector spatial light modulator for generation of arbitrary complex vector beams," *Opt. Lett.* 39, 386–389 (2014).
200. Z.-Y. Rong, Y.-J. Han, S.-Z. Wang, and C.-S. Guo, "Generation of arbitrary vector beams with cascaded liquid crystal spatial light modulators," *Opt. Express* 22, 1636–1644 (2014).
201. D. Maluenda, M. Aviñoá, K. Ahmadi, R. Martínez-Herrero, A. Carnicer, "Experimental estimation of the longitudinal component of a highly focused electromagnetic field, *Sci. Rep.* 11, 1-10 (2021).
202. H. H. Bauschke, P. L. Combettes, and D. R. Luke, "Phase retrieval, error reduction algorithm, and fienu variants: A view from convex optimization," *J. Opt. Soc. Am. A* 19, 1334–1345 (2002).
203. J. R. Fienup, "Phase retrieval algorithms: A comparison," *Appl. Opt.* 21, 2758–2769 (1982).

- 204.H.-E. Hwang, H. T. Chang, and W.-N. Lie, “Fast double-phase retrieval in fresnel domain using modified Gerchberg–Saxton algorithm for lensless optical security systems,” *Opt. Express* 17, 13700–13710.
- 205.J. A. Veerman, J. J. Rusch and P. H. Urbach, “Calculation of the rayleigh-sommerfeld diffraction integral by exact integration of the fast oscillating factor,” *JOSA A* 22, 636–646 (2005).
- 206.V. Nascov and P. C. Logofătu, “Fast computation algorithm for the Rayleigh–Sommerfeld diffraction formula using a type of scaled convolution,” *Appl. Opt.* 48, 4310–4319 (2009).
- 207.D. S. C. Biggs and M. Andrews, “Acceleration of iterative image restoration algorithms,” *Appl. Opt.* 36, 1766–1775 (1997).
- 208.J. Fienup and C. Wackerman, “Phase-retrieval stagnation problems and solutions,” *J. Opt. Soc. Am. A.* 3, 1897–1907 (1986).
- 209.M. Born and E. Wolf, *Principles of Optics: Electromagnetic Theory of Propagation, Interference and Diffraction of Light* (Cambridge University Press, 1999).
- 210.J. W. Goodman. *Introduction to Fourier Optics* (Roberts and Company Publishers, 2005).
- 211.L. Novotny, M. Beversluis, K. Youngworth, and T. Brown, “Longitudinal field modes probed by single molecules,” *Phys. Rev. Lett.* 86, 5251 (2001).
- 212.A. Bouhelier, M. R. Beversluis, and L. Novotny, “Near-field scattering of longitudinal fields,” *Appl. Phys. Lett.* 82, 4596–4598 (2003).
- 213.K. Kitamura, K. Sakai, and S. Noda, “Sub-wavelength focal spot with long depth of focus generated by radially polarized, narrow-width annular beam,” *Opt. Express.* 18, 4518–4525 (2010).
- 214.B. Jia, X. Gan, and M. Gu, “Direct observation of a pure focused evanescent field of a high numerical aperture objective lens by scanning near-field optical microscopy,” *Appl. Phys. Lett.* 86, 131110 (2005).
- 215.J. Wang, Q. Wang, and M. Zhang, “Development and prospect of near-field optical measurements and characterizations,” *Front. Optoelectron.* 5, 171–181 (2012).
- 216.S. N. Khonina, et al. “Experimental demonstration of the generation of the longitudinal e-field component on the optical axis with high-numerical-aperture binary axicons illuminated by linearly and circularly polarized beams,” *J. Opt.* 15, 085704 (2013).
- 217.S. Alferov, S. Khonina, and S. Karpeev, “Study of polarization properties of fiber-optics probes with use of a binary phase plate,” *JOSA A.* 31, 802–807 (2014).
- 218.V. V. Kotlyar, S. S. Stafeev, Y. Liu, L. O’Faolain, and A. A. Kovalev, “Analysis of the shape of a subwavelength focal spot for the linearly polarized light,” *Appl. Opt.* 52, 330–339 (2013).
- 219.W. Chen, and Q. Zhan, “Realization of an evanescent bessel beam via surface plasmon interference excited by a radially polarized beam,” *Opt. Lett.* 34, 722–724 (2009).
- 220.S. Khonina, S. Alferov, and S. Karpeev, “Strengthening the longitudinal component of the sharply focused electric field by means of higher-order laser beams,” *Opt. Lett.* 38, 3223–3226 (2013).
- 221.F. Rigaut, and N. Benoit, “Multiconjugate adaptive optics for astronomy,” *Annual Review of Astronomy and Astrophysics.* 56, 277-314 (2018).
- 222.L. N. Thibos, B. Arthur, and H. Xin, “A statistical model of the aberration structure of normal, well-corrected eyes,” *Ophthalmic and Physiological Optics.* 22.5, 427-433(2002).
- 223.R. Barakat, “Diffraction images of coherently illuminated objects in the presence of aberrations,” *Optica Acta: International Journal of Optics.* 16.2,205-223 (1969).
- 224.D. Claus, et al. “Ptychography applied to optical metrology,” *Speckle 2012: V International Conference on Speckle Metrology.* SPIE, 8413 (2012).

225. J. Liang, B. Grimm, S. Goelz, J. Bille, "Objective measurement of wave aberrations of the human eye with the use of a Hartmann-Shack wave-front sensor," *J. Opt. Soc. Am. A* 11, 1949-1957 (1994).
226. H. J. Matthews, D. K. Hamilton, and C. J. R. Sheppard, "Aberration Measurement by Confocal Interferometry," *J. Mod. Opt.* 36, 233-250 (1989).
227. H. Zhou, M. Gu, and C. J. R. Sheppard, "Investigation of Aberration Measurement in Confocal Microscopy," *J. Mod. Opt.* 42, 627-638 (1995).
228. Y. Yasuno, T. Yatagai, T. F. Wiesendanger, A. K. Ruprecht, and H. J. Tiziani, "Aberration measurement from confocal axial intensity response using neural network," *Opt. Express* 10, 1451-1457 (2002).
229. T. K. Barrett, D. G. Sandier, "Artificial neural network for the determination of Hubble Space Telescope aberration from stellar images," *Appl. Opt.* 32, 1720-1727 (1993).
230. H. Guo, et al. "Wavefront reconstruction with artificial neural networks," *Optics Express* 14.14, 6456-6462 (2006).
231. M. Cherukara, Y. Nashed, and R. Harder, "Real-time coherent diffraction inversion using deep generative networks," *Sci Rep.* 8, 16520 (2018).
232. Y. Zhang, M. Andreas Noack, P. Vagovic, K. Fezzaa, F. Garcia-Moreno, T. Ritschel, and P. Villanueva-Perez, "PhaseGAN: a deep-learning phase-retrieval approach for unpaired datasets," *Opt. Express* 29, 19593-19604 (2021).
233. Y. LeCun, Y. Bengio, and G. Hinton, "Deep learning" *Nature* 521, 436-444 (2015).
234. V. Ramírez-Sánchez, G. Piquero, and M. Santarsiero, "Generation and characterization of spirally polarized fields," *J. Opt. A: Pure Appl. Opt.* 11, 085708 (2009).
235. A. Carnicer and B. Javidi, "Optical security and authentication using nanoscale and thin-film structures," *Adv. Opt. Photonics.* 9, 218-256 (2017).
236. S. Abdollahramezani, O. Hemmatyar, H. Taghinejad, A. Krasnok, Y. Kiarashinejad, M. Zandehshahvar, A. Alù, and A. Adibi, "Tunable nanophotonics enabled by chalcogenide phase-change materials," *Nanophotonics.* 9, 1189-1241 (2020).
237. A. Sung-Hoon, et al. "Anisotropic material properties of fused deposition modeling ABS," *Rapid prototyping journal* (2002).
238. A. Mst Faujiya, et al. "Effects of part build orientations on fatigue behaviour of FDM-processed PLA material," *Progress in Additive Manufacturing* 1.1, 21-28 (2016).
239. R. Shougat, et al. "Effect of Building Orientation & Post Processing Material on Mechanical Properties of 3D Printed Parts," *Proceedings of the International Conference on Mechanical, Industrial and Energy Engineering, Khulna, Bangladesh* (2016).
240. Ö. Keles, C. W. Blevins, and K. J. Bowman, "Effect of build orientation on the mechanical reliability of 3D printed ABS," *Rapid Prototyping Journal.* 23.2, 320-328 (2017).
241. A. Pilipovi'c, P. Raos, and M. Sercer, "Experimental testing of quality of polymer parts produced by laminated object manufacturing – LOM," *Teh. Vjesn.* 18, 253-260 (2011).
242. A. Pilipovi'c, P. Raos, and M. Sercer, "Experimental analysis of properties of materials for rapid prototyping," *Int. J. Adv. Manuf. Tech.* 40, 105-115 (2009).
243. D. Dimitrov, K. Schreve, and N. D. Beer, "Advances in three dimensional printing – state of the art and future perspectives," *Rapid Prototyp. J.* 12, 136-147 (2006).
244. T. Galeta, M. Kljajin, and M. Karakasic, "Cost evaluation of shell and compact models in 3d printing," *Manuf. Eng.* 7, 27-29 (2008).
245. R. Pappu, B. Recht, J. Taylor, and N. Gershenfeld, "Physical one-way functions," *Science.* 5589, 2026-2030 (2002).

- 246.C. Herder, L. Ren, M. van Dijk, M. Yu, and S. Devadas, “Trapdoor computational fuzzy extractors and cryptographically–secure physical unclonable functions,” *IEEE T Depend. Secure.* 14, 65–82 (2017).
- 247.B. Akhoundi and A. Behraves, “Effect of filling pattern on the tensile and flexural mechanical properties of fdm 3d printed products,” *Experimental Mechanics.* 59, 883–897 (2019).
- 248.K. Ahmadi, P. Latorre-Carmona, B. Javidi, and A. Carnicer, “Polarimetric Identification of 3D-Printed Nano Particle Encoded Optical Codes,” *IEEE Photonics Journal*, 12, 1-10 (2020).
- 249.M. N. Polyanskiy. Refractive index database. [Online]. Available: <https://refractiveindex.info>
- 250.J. Dainty, “The statistics of speckle patterns,” in *Progress in Optics.* Elsevier. 14, 1–46 (1977).
- 251.V. Chandola, A. Banerjee, and V. Kumar, “Anomaly detection: a survey,” *ACM Comput. Surv.* 41, 15:1–15.58 (2009).
- 252.V. M. Patel, R. Chellappa, D. Chandra, and B. Barbelo, “Continuous user authentication on mobile devices: Recent progress and remaining challenges,” *IEEE Signal Process. Mag.* 33, 49–61 (2016).
- 253.S. Matteoli, M. Diani, and G. Corsini, “A tutorial overview of anomaly detection in hyperspectral image,” *IEEE Aero. El. Sys. Mag.* 25, 5–28 (2010).
- 254.S. S. Khan and M. G. Madden, “One-class classification: taxonomy of study and review of techniques,” *Knowl. Eng. Rev.* 29, 345–374 (2014).
- 255.D. Tax and R. Duin, “Support vector domain description,” *Pattern Recognit. Lett.* 20, 1191–1199 (1999).
- 256.B. Scholkopf, J. Platt, J. S. Taylor, A. Smola, and R. Williamson, “Estimating the support of a high-dimensional distribution,” *Neural Comput.* 13, 1443–1471 (2001).
- 257.N. V. Chawla, K. W. Bowyer, L. O. Hall, and W. P. Kegelmeyer, “Smote: synthetic minority over-sampling technique,” *Journal of artificial intelligence research.* 16, 321–357 (2002).
- 258.A. Iranmehr, H. Masnadi-Shirazi, and N. Vasconcelos, “Cost-sensitive support vector machines,” *Neurocomputing.* 343, 50–64 (2019).
- 259.F. Pedregosa, G. Varoquaux, A. Gramfort, V. Michel, B. Thirion, O. Grisel, M. Blondel, P. Prettenhofer, R. Weiss, V. Dubourg, J. Vanderplas, A. Passos, D. Cournapeau, M. Brucher, M. Perrot, and E. Duchesnay, “Scikit–learn: Machine learning in python,” *J. Mach. Learn. Res.* 12, 2825–2830 (2011).
- 260.R. Barandela, J. Sánchez, G. V., and R. E., “Strategies for learning in class imbalance problems,” *Pattern Recognit.* 36, 849–851 (2003).
- 261.M. Kubat and S. Matwin, “Addressing the curse of imbalanced data sets: One sided selection,” in *Proceedings of the Fourteenth International Conference on Machine Learning*, 179–186 (1997).